INVERSE DESIGN METHOD FOR SUPERSONIC TRANSPORT

(逆問題を用いた超音速機の設計法に関する研究)

BY

SHINKYU JEONG

DEPARTMENT OF
AERONAUTICS AND SPACE ENGINEERING OF
TOHOKU UNIVERSITY
SENDAI, JAPAN
JANUARY 1999

Inverse Design Method for Supersonic Transport

(逆問題を用いた超音速機の設計法に関する研究)

A THESIS
SUBMITTED TO THE GRADUATE OF ENGINEERING
OF TOHOKU UNIVERSITY

By

Shinkyu Jeong

IN PARTIAL FULFILLMENT OF THE REQUIREMENTS
FOR THE DEGREE OF
DOCTOR OF PHILOSOPHY

January 1999

Inverse Design Method for Supersonic Transport

(Abstract)

Shinkyu Jeong

Tohoku University, 1999

In this study, a robust and efficient design method for a wing of supersonic transport is developed. Takanashi's transonic inverse design method is extended to the supersonic flow region. The present inverse method is based on the iterative "residual-correction" concept. By applying Green's theorem, the governing partial differential equation (potential flow equation) is transformed into integral equations on a wing surface. In case of three-dimensional design problems, the present method is revised by using the supersonic linearized pressure coefficient equations near the wing root and tip where the irrotational flow assumption does not stand.

Genetic Algorithms (GAs) is next applied to optimize target pressure distribution for the inverse method. The key features of GAs are as following: 1) GAs use objective function information (fitness values) instead of derivatives or other auxiliary knowledge. 2) GAs search from a population of the points not from a single point. These features make GAs robust and attractive to practical aerodynamic design problems that often have to deal with multiple objectives.

The design goal of this study is the drag reduction under a specified lift. The shape of target pressure distribution that gives minimum drag is studied. For the induced drag reduction, chordwise loading patterns are examined.

Furthermore, a wing twist specification technique is introduced to the present supersonic inverse design method. It is known that three-dimensional aerodynamic

inverse problems have non-unique solutions. By using this property, one can select favorable wing geometry among the many solution geometries of the three-dimensional aerodynamic inverse problem. In the present study, a smooth trailing-edge line was sought as a favorable design for manufacturability.

Finally, to construct an efficient design system, the unstructured grid approach is implemented to the present inverse design method. The unstructured grid is generated using the advancing front method and Delaunay triangulation. The resulting design system was successfully applied to the inverse design of the wing-nacelle configuration. A great versatility and geometrical flexibility of the unstructured grid approach make our design system more efficient.

Acknowledgements

I would like to express my sincere appreciation to my advisors, Professor Kazuhiro Nakahashi and Associate Professor Shigeru Obayashi. Their advice, experience and encouragement have been invaluable. I wish to thank Professor Junji Tani for kind advice as a member of my thesis committee. And I would like to thank Professor Hisao Fukunaga for his concern and help during my study. I would like to thank Professor Keisuke Sawada. His sincere advice and suggestions made this work possible.

I would like to thank all the people in National Aerospace Laboratory who have provided continuous intellectual and financial support for this research. I express my thanks to Mr. Kimio Sakata for his encouragement. I owe Dr. Toshiyuki Iwamiya and Ms. Kisa Matsushima special thanks. During my stay at NAL, I worked with them. Their mathematical knowledge and experiences in the aerodynamic inverse problems are essential to develop the present supersonic inverse formulations. I also like to thank NAL SST design team for their sincere advice and for providing me many useful data.

I would like to acknowledge my brother and his wife's encouragement and support. Finally, I wish to sincerely thank my parents who have devoted their life to their sons.

CONTENTS

LIST OF TABLES

LIST OF FIGURES

CHAPTER Ⅰ

INTRODUCTION

Ⅰ-1. Development of Supersonic Transport (SST)

Since the advent of powered flight in 1903, commercial aviation has grown remarkably with the development of world economy and industry. This growth in air travel is projected to continue well into the 21st century with increasing demands for more efficient aircraft. As one of the answers for such a demand, next generation Supersonic Transports (SSTs) are considered.

The first generation SSTs are the TU-144 [1] and the Concorde [2]. Although both SSTs went into service in 1970s, they could not succeed in business very well. The TU-144 was developed by the Soviets and entered its service in 1975 as a mail and freight carrier within the Soviets Union. But it ceased the regular operation some time before 1985 because there were some problems with the engine and wing design.

Unlike the TU-144, the Concorde that started its commercial operation in 1976 still continues its service today as the only commercially operating SST. From the technological point of view, the Concorde was a great achievement. Especially, its high-speed performance was admirable. However, the Concorde also had some shortcomings. The community noise around the airport generated at the takeoff and landing and the sonic boom at the supersonic cruising caused the environment problems. Furthermore, the operating cost of the Concorde was rather high. It can be attributed to its poor low-speed performance (L/D=4.0). To compensate poor L/D, the Concorde had to use a powerful engine that consumed a more fuel, which increased the operating cost. Another weak point is that its operating range is too short (about 3500 nmi). To meet the demand of the markets, the non-stop range of over 5000 nmi is required. Because of these shortcomings, only 16 Concordes were manufactured before the project was stopped.

For the success of the next generation SST, it must be economically viable and environmentally acceptable. To develop such an airplane, the United States and the Europe already started research and development programs for next generation SSTs [3, 4, 5, 6, 7, 8, 9, 10] and their technologies for designing SSTs have advanced remarkably. To catch up with this worldwide progress, a supersonic research program [11, 12] has been initiated in National Aerospace Laboratory (NAL) of Japan. The main subjects of the program are to develop

1) CFD (Computational Fluid Dynamics)-based aerodynamic design technology

2) Light weight composite structure technology

3) High performance propulsion system

4) Advanced control system

Among these subjects, NAL had laid a special emphasis on the development of the sophisticated CFD design technique for the next generation SST. The technological achievements of the research program are applied to the design of scaled experimental airplanes. They will perform flight tests with these experimental airplanes. The CFD design technique developed in the research program will be verified by the flight tests.

School of Engineering of Tohoku University has made a cooperative agreement with NAL in an aerodynamic research based on CFD since 1995. Collaboration on the supersonic wing design has started in 1996. This doctoral research has been performed as a part of NAL and Tohoku University cooperative research program.

Ⅰ-2. CFD-Based Aerodynamic Design Technique

Although the theoretical methods were used for designing the Concorde, such as the slender body theory and the supersonic area rule, their applications were limited to make a rough estimate of the aerodynamic characteristics. The design of the Concorde was wholly based on the experimental data from several thousands hours of wind tunnel tests. Wind tunnel data are very helpful to the design of the airplane, however, its cost is too expensive.

On the other hand, the cost of numerical methods is much cheaper than that of wind tunnel test. There are several numerical design methods proposed for a wing at a supersonic speed. The most widely used design methods for supersonic aircraft are the linear theory for wing warp optimization [13] and the supersonic area rule for the fuselage indentation [14]. These methods are very effective to reduce the induced drag and the wave drag, respectively. However, these methods optimize each aircraft component separately. When each component of the aircraft is integrated into the complete configuration, the optimized effect of each component is degenerated due to the interference between the components of aircraft. In this case, the auxiliary steps to recover the optimized performance are required.

Recently, the design optimization methods [15, 16, 17, 18] that treat a complete configuration directly are extended to the supersonic aircraft design. The essence of these methods is that a numerical optimization method is coupled directly with an existing CFD analysis code. The numerical optimization method is used to minimize (maximize) a chosen aerodynamic quantity which is evaluated by a CFD analysis code. Most of these optimization methods require the evaluation of the gradient of the objective function with respect to the design variables. The configuration is systematically modified through the design variables in use. However, such a direct method will require many design variables in the precise description of complete aircraft configurations. Even with the modern supercomputer, it would take too many computational times.

An alternative approach, which requires much less computational expense, is inverse design methods. The aerodynamic inverse problem is defined to seek geometry that yields the prescribed pressure distribution at the design condition. The existing inverse design methods are categorized into two classes. The first is based on the partial differential equation of flows. These methods use the modified potential flow equation to solve a Dirichlet boundary value problem in which the velocity potential derived from a specified pressure distribution is imposed as a boundary condition. This method was developed by Carlson [19] and Tranen [20] for two-dimensional airfoil design and successfully extended to three-dimensional design problem by Henne [21] and Shankar [22]. However, the applications of these methods were limited to the minor modification of existing wings and airfoils. In other words, the geometry correction must be small enough to run these methods successfully. This means that the designer has to know approximate geometry of wing before the inverse design.

The second is based on the iterative “residual-correction” concept. This class of methods solves auxiliary equations to find geometry corrections corresponding to residuals at each iteration step defined as the difference between the pressure on the transient geometry and the pressure prescribed by the designer. Because of the iterative approach, a relatively large geometry correction can be achieved. One of the merits of this class of methods is that these methods can be applied to complicated configurations with thanks to the iterative “residual-correction” concept. Another advantage is that the required analysis can be “black-box,” and thus any type of analysis, even experiment, can be used.

This kind of methods [23, 24, 25] can be further classified by the auxiliary equations to find geometry corrections: wave-wall, Garabedian-McFadden (GM) and integral equations. Among these methods, Takanashi’s inverse design method [26] that uses the integral equations as the auxiliary equations has advantage over the other methods in applicability to three-dimensional design problems, since most of the other methods are formulated only for two-dimensional design problems. Furthermore, Takanashi’s method needs less geometry constraints than the other methods. These merits of Takanashi’s method are also attractive to supersonic design problems. Unfortunately, Takanashi’s method was formulated only for subsonic and transonic flows. The extension of Takanashi’s method implies that the method has to be derived mathematically again from the governing equations of supersonic flows.

Ⅰ-3. Optimization Method for Aerodynamic Design

The aerodynamic inverse problem is to find geometry corresponding to the prescribed pressure distribution. The most important point to obtain a wing of a high performance with an inverse method is to find an appropriate target pressure distribution. Therefore, numerical optimization is considered for the determination of target pressures.

The numerical optimization method is very important to improve the design efficiency. One of the most widely used optimization algorithms is the gradient-based method. While this method has been improved and extended considerably, there are some weak points for the application to real-world engineering problems. First, this method is local in scope. It will not find a global optimum, because this method can only find a local optimum in a neighborhood of the initial point. Second, this method requires a well-defined gradient in the domain of interest. However, the aerodynamic engineering problems are fraught with discontinuities and ripples in the objectives as well as the constraints. In this sense, the gradient-based method is not suitable for an aerodynamic design problem.

Recently, Genetic Algorithms (GAs) [27], one of the Evolutionary Algorithms, have been enjoying popularity in this field. GAs are search algorithms based on the mechanics of natural selection and natural genetics. GAs are different from other conventional optimization methods in the following four points:

1) GAs work with a coding of the parameters set, not the parameters themselves.

2) GAs search from a population of points, not a single point.

3) GAs use payoff (objective function) information, not derivatives or other auxiliary knowledge.

4) GAs use probabilistic transition rules, not deterministic rules.

These features make GAs robust and attractive to aerodynamic design problems where nonlinearity of fluid may result in discontinuities in the objectives, constraints and their derivatives.

GAs have been applied to aeronautical problems in several ways, including parametric and conceptual design of aircraft [28], topological design of nonplanar wings [29] and aerodynamic optimization using CFD [30]. Application of these aerodynamic optimization methods to realistic problems, however, is limited by the fact that they are the direct approach. The direct approach requires CFD evaluations of each members of the population at every generation in GAs. As a result, it requires a tremendous amount of computational time.

In recent years, GAs has been applied to inverse optimization methods [31, 32] for the aerodynamic design. In this case, since the objective of optimization is not a geometry itself but a pressure distribution, GAs are not required to perform CFD evaluations. By doing this way, computational cost can be saved greatly. This method was successfully applied to aerodynamic design of transonic wings for commercial aircraft [33]. This design approach will also be extended to the supersonic wing design.

Ⅰ-4. Unstructured Grid Approach

CFD becomes an indispensable tool for the aerodynamic design and analysis of aircraft. However, its application to a design problem is still limited to relatively simple aircraft components such as airfoils and wings. One of the real bottlenecks is the time-consuming procedure to generate an appropriate grid around a complex configuration. One of the options for resolving this problem is unstructured grid approaches [34,35, 36, 37, 38]. Although this unstructured grid method requires an additional cost in terms of computational time and memory for the flow algorithms, this approach, as a counter balance, has a great versatility and geometrical flexibility to the mesh generation process. Its workload required for grid generation around the complicated aircraft configurations is far less than that of the structured grid approach. It will be very effective to adopt the unstructured grid approach to CFD design system, especially, in case of the complicated configuration design

.

Ⅰ-5. Objectives and Outline of This Thesis

The objective of this study is the development of a robust and efficient design method for a wing of a supersonic transport. As a main objective of this works, Takanashi’s transonic inverse design method that solves the integral equations using the iterative “residual-correction” concept to find geometry corrections will be extended to a supersonic flow region. Optimization of the inverse design and application of the inverse design to complicated configurations will then be studied.

In Chapter 2, mathematical formulation for the supersonic inverse method will be described. Modification for improving the convergence to the target pressure distribution will be also suggested here. The validation of the present formulation will be given through design test cases.

In Chapter 3, with the supersonic inverse code developed in Chapter 2, the optimum design will be executed. Genetic Algorithm will be applied to optimize a target pressure distribution required for the inverse design. The shape of a target pressure distribution for the drag reduction will be considered. Furthermore, the twist-specification inverse design (TSID) will be introduced. The concept of TSID is based on the non-uniqueness of the three-dimensional aerodynamic inverse problem. A designer should be able to select a favorable geometry among many solution geometries of the inverse problem. Therefore, TSID specifies the twist distribution for manufacturability.

In Chapter 4, the inverse design method will be extended to the wing-fuselage and wing-nacelle configurations. The proposed inverse method has been implemented into NAL SST design process successfully. The design result of a wing-fuselage configuration of NAL's scaled supersonic experimental aircraft is presented by courtesy of NAL SST design team. CFD analysis about the wing-fuselage configuration was performed using the multiblock structured grid approach. This design reveals that the grid generation is a bottleneck of the inverse design around the complicated geometry. To resolve this problem, the unstructured grid approach will be adapted to the design of wing-nacelle configuration because of its flexibility to fit complex configuration and refinement capability. Although the nacelles produce a strong influence on the flow filed, the inverse method works satisfactory.

References

[1] M. D. Christine and D. O. Erik, “Elements of NASA’s High-Speed Research Program,” AIAA Paper 93-2942, 1993.

[2] J. Rech and C. S. Leyman, “A Case Study by Aerospatiale and British Aerospace on the Concorde,” AIAA Professional Study Series.

[3] P. Satre, “Supersonic Air Transport – True Problem and Misconception,” *Journal of Aircraft*, Vol. 7, No. 1, pp. 3-12, Jan. – Feb. 1970.

[4] L. K. Loftin, Jr., “Toward a Second-Generation Supersonic Transport,” *Journal of Aircraft*, Vol. 11, No. 1, pp. 3-9, January 1974.

[5] A. Ferri, “Possibilities and Goals for the Future SST,” *Journal of Aircraft*, Vol. 12, No. 12, pp. 919-929, December 1975.

[6] C. W. Clay and A. Sigalla, “Shape of the Future Long-Haul Airplane,” *Journal of Aircraft*, Vol. 13, No. 8, pp. 551-558, August 1976.

[7] E. Q. Bond, B. R. Wright, E. A. Carroll and R. A. Flume, “Impact for Cruise Speed on Productivity of Supersonic Transports,” *Journal of Aircraft*, Vol. 17, No. 3, pp. 143-151, March 1980.

[8] Boeing Commercial Airplanes, “High-Speed Civil Transport Study,” NASA CR-4233, 1989.

[9] Douglas Aircraft Company, “Study of High-Speed Civil Transports,” NASA CR-4236, 1990.

[10] R. V. Harris Jr., “ On the Threshold – The Outlook for Supersonic and Hypersonic Aircraft,” *Journal of Aircraft*, Vol. 29, No. 1, pp. 10-19, Jan. – Feb. 1992.

[11] K. Takasawa, “Research on High-Speed Transport Program and Present Status at NAL, Tokyo,” AIAA Paper 96-6690, 1996.

[12] K. Sakata, “Supersonic Research Program in NAL, Japan,” Proceedings of 1st International CFD Workshop for SST Design, pp. 1-4, Tokyo, Japan, NAL, March 1998.

[13] H. W. Carlson and D. S. Miller, “Numerical Method for the Design and Analysis of Wings at Supersonic Speeds,” NASA TN D-7713, 1974.

[14] H. Ashely and M. Landahl, *Aerodynamics of Wings and Bodies*, Addison-Wesley Publishing Company, Inc., Reading, 1965.

[15] R. M. Hicks, E. M. Murman, and G. N. Vanderplaats, “An Assessment of Airfoil Design by Numerical Optimization, NASA TM X-3092, 1974.

[16] R. M. Hicks and P. A. Henne, “Wing Design by Numerical Optimization,” *Journal of Aircraft*, Vol. 15, No. 7, pp. 407-412, July 1978.

[17] J. Reuther, S. Cliff, R. Hicks and C. P. van Dan, “Practical Design Optimization of Wing/Body Configurations Using Euler Equations,” AIAA Paper 92-2633, 1992.

[18] J. Reuther and A. Jameson, “Aerodynamic Shape Optimization of Wing and Wing-Body Configurations Using Control Theory,” AIAA 95-0123, 1995.

[19] L. A. Carlson, “Transonic Airfoil Design Using Cartesian Coordinates,” NASA CR-2578, 1976.

[20] T. L. Tranen, “A Rapid Computer Aided Transonic Airfoil Design Methods,” AIAA Paper 74-501, 1974.

[21] P. A. Henne, “Inverse Transonic Wing Design Method,” *Journal of Aircraft*, Vol. 18,

No. 2, pp. 121-127, February 1981.

[22] V. Shankar, "A Full Potential Inverse Method Based on a Density Linearization Scheme for Wing Design," AIAA Paper 81-1234, 1981.

[23] W. H. Davis, Jr., "Technique for Developing Design Tools from the Analysis Methods of Computational Aerodynamics," *AIAA Journal*, Vol. 18, No. 9, pp. 1080-1087, September 1980.

[24] J. B. Malone, J. Vadyak and L. N. Shankar, "A Technique for the Inverse Aerodynamic Design of Nacelles and Wing Configurations," AIAA Paper 85-4096, 1985.

[25] L. C. Santos and L. N. Sankar, "A Hybrid Inverse Optimization Method for the Aerodynamic Design of Lifting Surfaces," AIAA Paper 94-1895, 1994.

[26] S. Takanashi, "Iterative Three-Dimensional Transonic Wing Design Using Integral Equations," *Journal of Aircraft*, Vol. 22, No. 8, pp. 655-660, August 1985.

[27] D. E. Goldberg, *Genetic Algorithms in Search, Optimization & Machine Learning*, Addison-Wesley Publishing, Inc., Reading, January 1989.

[28] Y. Crispin, "Aircraft Conceptual Optimization Using Simulated Evolution," AIAA Paper 94-0092, 1989.

[29] P. Gage and I. Kroo, "A Role of Genetic Algorithms in a Preliminary Design Environment," AIAA Paper 93-3933, 1933.

[30] D. Quagliarella and A. D. Cioppa, "Genetic Algorithms Applied to the Aerodynamic Design of Transonic Airfoils," AIAA Paper 94-1896, 1994.

[31] S. Obayashi and S. Takanashi, "Genetic Optimization of Target Pressure

Distributions for Inverse Design Methods," *AIAA Journal*, Vol. 34, No. 5, pp. 881-886, May 1996.

[32] H. Kim and O. Rho, "Aerodynamic Design of Transonic Wing Using the Target Pressure Optimization Approach," AIAA Paper 98-0599, 1998.

[33] S. Takahashi, S. Obayashi and K. Nakahashi, "Inverse Optimization of Transonic Wing Shape for Mid-Size Regional Aircraft," AIAA Paper 98-0601, 1998.

[34] K. Nakahashi, "A Finite-Element Method on Prismatic Elements for Three-Dimensional Navier-Stokes Equations," Lecture Notes in Physics, No. 323, pp. 434-438, Springer, 1998.

[35] R. Löhner, and P. Parikh, "Three-Dimensional Grid Generation by Advancing Front Method," *International Journal of Numerical Methods Fluids*, Vol. 8, pp. 1135-1149, 1998.

[36] D. Sharov and K. Nakahashi, "A Boundary Recovery Algorithm for Delaunay Tetrahedral Meshing," 5th International Conference on Numerical Grid Generation in Computational Field Simulation, pp. 229-238, 1996.

[37] K. Nakahashi and D. Sharov, "Direct Surface Triangulation Using the Advancing Front Method," AIAA Paper 95-1686, 1995.

[38] V. Venkatakrishnan, "A Perspective on Unstructured Grid Flow Solvers," AIAA Paper 95-0667, 1995.

CHAPTER Ⅱ

INVERSE DESIGN METHOD FOR WINGS OF SUPERSOINC TRANSPORT

II - 1. Introduction

For the success of the next generation SST development, an efficient and robust aerodynamic wing design system is necessary. The existing supersonic wing design methods [1, 2, 3] so far have their own limitations. In case of transonic wing design, Takanashi's inverse methods [4] coupled with target pressure optimization codes [5, 6, 7, 8] were very successful. The merits of this method are as follows:

1) it requires less computational time, compared with direct design methods.
2) it accounts for nonlinear effects of thickness distribution to the optimized warp because warp and thickness are designed simultaneously.
3) it can be applied to complicated configurations [9].

In this chapter, extension of this method to the supersonic wing design will be considered. The mathematical formulation for supersonic flows [10] will be mainly discussed here and design tests will be given for validation of the formulation.

II-2. Formulation of Supersonic Inverse Method

In a supersonic flow, the potential equation can be expressed in the linearized form, as

$$(M_\infty^2 - 1)\bar{\phi}_{\bar{x}\bar{x}} - \bar{\phi}_{\bar{y}\bar{y}} - \bar{\phi}_{\bar{z}\bar{z}} = 0 \tag{2-1}$$

The pressure coefficient on a wing surface and the tangency condition are expressed in terms of the velocity potential $\bar{\phi}_x$ and $\bar{\phi}_z$, as

$$C_{p\pm}(\bar{x}, \bar{y}) = -2\bar{\phi}_{\bar{x}}(\bar{x}, \bar{y}, \pm 0) \tag{2-2}$$

$$\frac{\partial \bar{f}_{\pm}(\bar{x}, \bar{y})}{\partial \bar{x}} = \bar{\phi}_{\bar{z}}(\bar{x}, \bar{y}, \pm 0) \tag{2-3}$$

where the subscripts '±' denote the upper and lower surfaces of the wing. For brevity, the expression $\beta^2 = M_\infty^2 - 1$ is eliminated through a Prandtl-Glauert transformation and a new coordinate system with *x*, *y* and *z* is introduced as

$$x = \bar{x}, \ \ y = \beta \bar{y}, \ \ z = \beta \bar{z} \tag{2-4}$$

After the transformation, Eqs. (2-1), (2-2) and (2-3) are rewritten as

$$\phi_{xx} - \phi_{yy} - \phi_{zz} = 0 \tag{2-5}$$

$$C_{p\pm}(x, \frac{y}{\beta}) = -2\beta^2 \phi_x(x, y, \pm 0) \tag{2-6}$$

$$\frac{\partial f_{\pm}(x, y)}{\partial x} = \beta^3 \phi_z(x, y, \pm 0) \tag{2-7}$$

Suppose $\phi(x, y, z)$, the solution of the equation (2-5) which governs the potential flow due to the initial geometry $f(x, y)$, is already known by means of numerical analysis or experiment. Now let us introduce small perturbation due to the geometry displacement $\Delta f(x,y)$. Then, the governing equation of this perturbed flow is expressed as

$$(\phi_{xx} + \Delta\phi_{xx}) - (\phi_{yy} + \Delta\phi_{yy}) - (\phi_{zz} + \Delta\phi_{zz}) = 0 \qquad (2\text{-}8)$$

and the pressure coefficient and the tangency condition are written as

$$C_{p\pm}(x, \frac{y}{\beta}) + \Delta C_{p\pm}(x, \frac{y}{\beta}) = -2\beta^2[\phi_x(x, y, \pm 0) + \Delta\phi_x(x, y, \pm 0)] \qquad (2\text{-}9)$$

$$\frac{\partial f_\pm(x,y)}{\partial x} + \frac{\partial \Delta f_\pm(x,y)}{\partial x} = \beta^3[\phi_z(x, y, \pm 0) + \Delta\phi_z(x, y, \pm 0)] \qquad (2\text{-}10)$$

By subtracting Eqs. (2-5) - (2-7) from Eqs. (2-8) - (2-10), the perturbation equations for the geometry displacement $\Delta f(x,y)$ are obtained as follows.

$$\Delta\phi_{xx} - \Delta\phi_{yy} - \Delta\phi_{zz} = 0 \qquad (2\text{-}11)$$

$$\Delta C_{p\pm}(x, \frac{y}{\beta}) = -2\beta^2 \Delta\phi_x(x, y, \pm 0) \qquad (2\text{-}12)$$

$$\frac{\partial \Delta f_\pm(x,y)}{\partial x} = \beta^3 \Delta\phi_z(x, y, \pm 0) \qquad (2\text{-}13)$$

The purpose of the present inverse method is to find the geometry displacement $\Delta f(x,y)$ from the pressure difference $\Delta C_p(x,y)$. In order to find $\Delta f(x,y)$, it is required to solve the partial difference equation (2-11). By applying a Green's theorem to Eq. (2-11), $\Delta\phi(x,y)$ can be expressed in the integrodifferential form. The analytic expression of Green's theorem for Eq. (2-11), relating a volume integral over the region *V* to a surface integral over surface *S* enclosing *V*, is written in the form

$$\iiint_V [\varphi L(\Delta\phi) - \Delta\phi L(\varphi)] dV = -\iint_S [\varphi D_n(\Delta\phi) - \Delta\phi D_n \varphi] dS \qquad (2\text{-}14)$$

where

$$L(\Delta\phi) \equiv \Delta\phi_{xx} - \Delta\phi_{yy} - \Delta\phi_{zz} \tag{2-15}$$

and

$$D_n = n_1 \frac{\partial\Delta\phi}{\partial x} - n_2 \frac{\partial\Delta\phi}{\partial y} - n_3 \frac{\partial\Delta\phi}{\partial z} \tag{2-16}$$

In Eq. (2-16), n_1, n_2 and n_3 are direction cosines of inward normals to the surface *S* and they have following relations with co-normal cosines ν_1, ν_2 and ν_3 as

$$\nu_1 = -n_1, \nu_2 = n_2, \nu_3 = n_3 \tag{2-17}$$

The geometry connection between the normal and the co-normal is illustrated in Fig. 2-1.

Replacing the normal cosines in Eq. (2-14) with the co-normal cosines, Eq. (2-14) becomes

$$\iiint_V [\varphi L(\Delta\phi) - \Delta\phi L(\varphi)] dV = -\iint_S \left[\varphi \frac{\partial\Delta\phi}{\partial\nu} - \Delta\phi \frac{\partial\varphi}{\partial\nu} \right] dS \tag{2-18}$$

If φ is properly chosen so as to satisfy $L(\varphi) = 0$ throughout the region *V*, Eq. (2-18) is reduced to the following equation;

$$\iint_S \varphi \frac{\partial\Delta\phi}{\partial\nu} dS = \iint_S \Delta\phi \frac{\partial\varphi}{\partial\nu} dS \tag{2-19}$$

Now consider a point $P(x, y, z)$ and a surface τ, as sketched in Fig. 2-2. The purpose of application of Green's theorem is to determine the value of $\Delta\phi$ at an arbitrary point $P(x, y, z)$. From the physics of the supersonic flow, the area that influences on the value of $\Delta\phi$ at *P* is restricted to the region within the forecone with a vertex at *P* and within the envelope of the aftercone with vertices at the foremost disturbance area of τ. Referring to Fig. 2-2, this would mean the volume bounded by forecone Γ and the aftercone λ with a vertex at the apex of the surface τ. Since for the boundary value problems involved the surface τ remain in the *xy*-plane, the integral surface *S* consists of all three surfaces λ, Γ and τ.

To the surface Γ, it is impossible to determine $\Delta\phi$ and $\frac{\partial\Delta\phi}{\partial\nu}$ unless the particular solution φ and its derivatives with respect to co-normal vanish everywhere on Γ. Thus the proper choice of φ is

$$\varphi(x,y,z;\xi,\eta,\zeta)=\cosh^{-1}\frac{x-\xi}{\sqrt{(y-\eta)^2+(z-\zeta)^2}} \tag{2-20}$$

The value of φ becomes zero on the forecone Γ, since the equation of this cone is

$$(x-\xi)^2-(y-\eta)^2-(z-\zeta)^2=0 \tag{2-21}$$

Furthermore, since the co-normal is always directed along the forecone, $\frac{\partial\varphi}{\partial\nu}$ is the gradient of φ along Γ and thus it is also zero. As a result, the integration on the surface Γ vanishes.

To the surfaces λ and τ, Eq. (2-19) provides an equality for the distribuiton of $\Delta\phi$ and $\frac{\partial\Delta\phi}{\partial\nu}$, provided $\Delta\phi$ and φ satisfy Eq. (2-11) through the enclosed volume mentioned. However, although φ satisfies Eq. (2-11) everywhere in the enclosed volume opposite τ from *P* (under the *xy* plane in Fig. 2-2), along the line $(y-\eta)^2+(z-\zeta)^2=0$ (above the *xy* plane in Fig. 2-2) φ is infinite and does not satisfy the assumption made in establishing Green's theorem. If this line is excluded, however, by means of a cylinder κ of radious ρ with the axis lying along the line $(y-\eta)^2+(z-\zeta)^2=0$, then equation (2-19) may be applied to the region outside κ and yet within the space bounded by λ, Γ and τ. In fact Eq. (2-19) can then be written

$$\iint_{\tau_1+\kappa+\lambda}\left(\Delta\phi\frac{\partial\varphi}{\partial\nu}-\varphi\frac{\partial\Delta\phi}{\partial\nu}\right)dS=0 \qquad (2\text{-}22)$$

where τ_1 is the portion τ of bounding the region of integration. If $R=\sqrt{(y-\eta)^2+(z-\zeta)^2}$ and cylindrical coordinates ρ, θ and $(x-\xi)$ are used, an element of area on the cylinder κ is $dS=-\rho d\theta d(x-\xi)$, while

$$\frac{\partial\varphi}{\partial\phi}=\frac{\partial\varphi}{\partial R}=-\frac{(x-\xi)}{\rho\sqrt{(x-\xi)^2-\rho^2}} \qquad (2\text{-}23)$$

so that

$$\lim_{\rho\to 0}\iint_{\kappa}\left[\Delta\phi\frac{\partial\varphi}{\partial\nu}-\varphi\frac{\partial\Delta\phi}{\partial\nu}\right]$$

$$=\lim_{\rho\to 0}\iint_{\kappa}\frac{\rho\Delta\phi(x-\xi)d\theta d(x-\xi)}{\rho\sqrt{(x-\xi)^2\rho^2}}-\lim_{\rho\to 0}\iint_{\kappa}\frac{\partial\Delta\phi}{\partial\nu}\cosh^{-1}(\frac{x-\xi}{\rho})d\theta d(x-\xi)$$

$$=-\iint_{\kappa}\Delta\phi d\theta d\xi-\iint_{\kappa}\lim_{\rho\to 0}\frac{\partial\Delta\phi}{\partial\nu}\left(\ln\frac{x-\xi}{\rho}\right)\rho d\theta d(x-\xi)$$

$$=-2\pi\int_{x_\lambda}^{x}\Delta\phi(\varepsilon,y,z)d\varepsilon \qquad (2\text{-}24)$$

where x_λ is x on λ.

If this result is applied to Eq. (2-22), one can obtain

$$2\pi\int_{x_\lambda}^{x}\Delta\phi(\varepsilon,y,z)d\varepsilon=\iint_{\tau_1+\lambda}\left[\Delta\phi\frac{\partial\varphi}{\partial\nu}-\varphi\frac{\partial\Delta\phi}{\partial\nu}\right]dS \qquad (2\text{-}25)$$

and, after differentiating Eq. (2-25) with respect to *x*,

$$\Delta\phi(x,y,z)=\frac{1}{2\pi}\frac{\partial}{\partial x}\iint_{\tau_1+\lambda}\left[\Delta\phi\frac{\partial\varphi}{\partial\nu}-\varphi\frac{\partial\Delta\phi}{\partial\nu}\right]dS \qquad (2\text{-}26)$$

Now considering the region bounded by the surfaces τ, Γ and λ', the portion of λ on the opposite side of τ from the point *P*, φ is finite through the region and Eq. (2-22) becomes

$$0 = -\frac{1}{2\pi}\frac{\partial}{\partial x}\iint_{\tau_1+\lambda'}\left[\Delta\phi'\frac{\partial\varphi}{\partial\nu'} - \varphi\frac{\partial\Delta\phi'}{\partial\nu'}\right]dS \tag{2-27}$$

where $\Delta\phi'$ is the value of the potential function on the side of τ opposite *P* and ν' is in the opposite direction to ν on τ.

By adding Eq. (2-26) to Eq. (2-27),

$$\Delta\phi(x,y,z) = -\frac{1}{2}\frac{\partial}{\partial x}\iint_{\tau_1}\left[\frac{\partial\Delta\phi}{\partial\nu} + \frac{\partial\Delta\phi'}{\partial\nu'}\right]\varphi dS$$
$$+\frac{1}{2\pi}\frac{\partial}{\partial x}\iint_{\tau_1}(\Delta\phi - \Delta\phi')\frac{\partial\varphi}{\partial\nu}dS + \frac{1}{2\pi}\frac{\partial}{\partial x}\iint_{\lambda}\left[\Delta\phi\frac{\partial\varphi}{\partial\nu} - \varphi\frac{\partial\Delta\phi}{\partial\nu}\right]dS$$
$$+\frac{1}{2\pi}\frac{\partial}{\partial x}\iint_{\lambda'}\left[\Delta\phi'\frac{\partial\varphi}{\partial\nu'} - \varphi\frac{\partial\Delta\phi'}{\partial\nu'}\right]dS$$

(2-28)

The value of $\Delta\phi$ on λ and λ' is zero since $\Delta\phi$ is identified with the perturbation velocity potential in this study. Thus Eq. (2-28) becomes

$$\Delta\phi(x,y,z)$$
$$= -\frac{1}{2\pi}\frac{\partial}{\partial x}\iint_{\tau_1}\left[\frac{\partial\Delta\phi}{\partial\nu} - \frac{\partial\Delta\phi'}{\partial\nu'}\right]\varphi dS + \frac{1}{2\pi}\frac{\partial}{\partial}\iint_{\tau_1}(\Delta\phi - \Delta\phi')\frac{\partial\varphi}{\partial\nu}dS$$

(2-29)

From the thin-wing assumption, $\frac{\partial}{\partial\nu} = \frac{\partial}{\partial\xi}$ and thus Eq. (2-29) can be written as

$$\Delta\phi(x,y,z) =$$
$$-\frac{1}{2\pi}\frac{\partial}{\partial x}\iint_{\tau_1}[(\Delta\phi_{\zeta}(\xi,\eta,+0) - \Delta\phi_{\zeta}(\xi,\eta,-0))\times\varphi(x,y,z;\xi,\eta,0)]d\xi d\eta \qquad \rightarrow①$$

$$+\frac{1}{2\pi}\frac{\partial}{\partial x}\iint_{\tau_1}[(\Delta\phi(\xi,\eta,+0)-\Delta\phi(\xi,\eta,-0))\times\varphi_{\zeta}(x,y,z;\xi,\eta,0)]d\xi d\eta \qquad \to ②$$

(2-30)

For the first term on the right-hand side, ①, the partial derivative can be moved inside the integral as

$$① = -\frac{1}{2\pi}\iint_{\tau_1}\frac{1}{\sqrt{(x-\xi)^2-(y-\eta)^2-z^2}}\times\left[\Delta\phi_{\zeta}(\xi,\eta,+0)-\Delta\phi_{\zeta}(\xi,\eta,-0)\right]d\xi d\eta$$

(2-31)

The second term on the right-hand side, ②, can be rewritten as

$$② = \frac{1}{2\pi}\frac{\partial}{\partial x}\iint_{\tau_1}\frac{z(x-\xi)}{\left[(y-\eta)^2+z^2\right]\sqrt{(x-\xi)^2-(y-\eta)^2-z^2}}\left[\Delta\phi(\xi,\eta,+0)-\Delta\phi(\xi,\eta,-0)\right]d\xi d\eta$$

$$=\frac{1}{2\pi}\frac{\partial}{\partial x}\int d\eta\left\{\left[\frac{-z\sqrt{(x-\xi)^2-(y-\eta)^2-z^2}}{(y-\eta)^2+z^2}\left[\Delta\phi(\xi,\eta,+0)-\Delta\phi(\xi,\eta,-0)\right]\right]_{L.E.}^{x}\right.$$

$$\left.+\int\frac{z\sqrt{(x-\xi)^2-(y-\eta)^2-z^2}}{(y-\eta)^2+z^2}\left[\Delta\phi_{\xi}(\xi,\eta,+0)-\Delta\phi_{\xi}(\xi,\eta,-0)\right]d\xi\right\}$$

(2-32)

Assuming the subsonic leading edge,

$$\xi = L.E. \quad \to \quad \Delta\phi(L.E.,\eta,+) = \Delta\phi\ (L.E.,\eta,-0)$$

$$\xi = x\ (on\ the\ Mach\ cone) \quad \to \quad r_c = \sqrt{(x-\xi)^2-(y-\eta)^2-z^2} = 0$$

and thus,

$$② = \frac{1}{2\pi}\frac{\partial}{\partial x}\int d\eta\int_{L.E.}^{x}\frac{zr_c}{(y-\eta)^2+z^2}\left[\Delta\phi_{\xi}(\xi,\eta,+0)-\Delta\phi_{\xi}(\xi,\eta,-0)\right]d\xi \qquad (2\text{-}33)$$

On the Mach forecone, $r_c = 0$ so the partial derivative $\dfrac{\partial}{\partial x}$ can be moved into the integral as

$$②=\frac{1}{2\pi}\iint_{\tau_1}\frac{z(x-\xi)}{\left[(y-\eta)^2+z^2\right]r_c}\left[\Delta\phi_\xi(\xi,\eta,+0)-\Delta\phi_\xi(\xi,\eta,-0)\right]d\xi d\eta \qquad (2\text{-}34)$$

Therefore,

$$\begin{aligned}\Delta\phi(x,y,z)&=①+②\\&=-\frac{1}{2\pi}\iint_{\tau_1}\frac{1}{\sqrt{(x-\xi)^2-(y-\eta)^2-z^2}}\times\left[\Delta\phi_\zeta(\xi,\eta,+0)-\Delta\phi_\zeta(\xi,\eta,-0)\right]d\xi d\eta\\&\quad+\frac{1}{2\pi}\iint_{\tau_1}\frac{z(x-\xi)}{\left[(y-\eta)^2+z^2\right]r_c}\left[\Delta\phi_\xi(\xi,\eta,+0)-\Delta\phi(\xi,\eta,-0)\right]d\xi d\eta\end{aligned}$$

(2-35)

To utilize the pressure distributions as a boundary condition, Eq. (2-35) is differentiated with respect to x and then by adding the values of the resulting $\Delta\phi_x(x,y,z)$ at $z=+0$ and $z=-0$,

$$\begin{aligned}&\Delta\phi_x(x,y,+0)+\Delta\phi_x(x,y,-0)\\&=-\frac{1}{2\pi}\frac{\partial}{\partial x}\iint_{\tau_1}\frac{1}{r_{c(z=+0)}}\left[\Delta\phi_\zeta(\xi,\eta,+0)-\Delta\phi_\zeta(\xi,\eta,-0)\right]d\xi d\eta &&\rightarrow③\\&\quad-\frac{1}{2\pi}\frac{\partial}{\partial x}\iint_{\tau_1}\frac{1}{r_{c(z=-0)}}\left[\Delta\phi_\zeta(\xi,\eta,+0)-\Delta\phi_\zeta(\xi,\eta,-0)\right]d\xi d\eta &&\rightarrow④\\&\quad+\frac{1}{2\pi}\frac{\partial}{\partial x}\iint_{\tau_1}\frac{z(x-\xi)}{\left[(y-\eta)^2+z^2\right]r_{c(z=+0)}}\left[\Delta\phi_\xi(\xi,\eta,+0)-\Delta\phi(\xi,\eta,-0)\right]d\xi d\eta &&\rightarrow⑤\\&\quad+\frac{1}{2\pi}\frac{\partial}{\partial x}\iint_{\tau_1}\frac{z(x-\xi)}{\left[(y-\eta)^2+z^2\right]r_{c(z=-0)}}\left[\Delta\phi_\xi(\xi,\eta,+0)-\Delta\phi(\xi,\eta,-0)\right]d\xi d\eta &&\rightarrow⑥\end{aligned}$$

(2-36)

The first term on the right-hand side, ③, can be calculated as

$$③ = -\frac{1}{2\pi}\lim_{\varepsilon\to+0}\frac{\partial}{\partial x}\int_{L.E.}^{x-\varepsilon}d\xi\int_{Y_1}^{Y_2}\frac{\Delta\phi_\zeta(\xi,\eta,+0)-\Delta\phi_\zeta(\xi,\eta,-0)}{\sqrt{(x-\xi)^2-(y-\eta)^2}}d\eta$$

$$= -\frac{1}{2\pi}\lim_{\varepsilon\to+0}\int_{\mathrm{y}-\varepsilon}^{\mathrm{y}+\varepsilon}\frac{\Delta\phi_\zeta(\xi,\eta,+0)-\Delta\phi_\zeta(\xi,\eta,-0)}{\sqrt{\varepsilon^2-(y-\eta)^2}}d\eta$$

$$-\frac{1}{2\pi}\int_{L.E.}^{x-\varepsilon}d\xi\frac{\partial}{\partial x}\int_{Y_1}^{Y_2}d\eta\frac{\Delta\phi_\zeta(\xi,\eta,+0)-\Delta\phi_\zeta(\xi,\eta,-0)}{\sqrt{(x-\xi)^2-(y-\eta)^2}}$$

(where $Y_1 = y-|x-\xi|, Y_2 = y+|y-\xi|$)

$$= -\frac{1}{2\pi}\lim_{\varepsilon\to+0}\left[\left(-\sin^{-1}\frac{y-\eta}{\varepsilon}\right)\left(\Delta\phi_\zeta(\xi,\eta,+0)-\Delta\phi_\zeta(\xi,\eta,-0)\right)\right]_{y-\varepsilon}^{y+\varepsilon}$$

$$-\frac{1}{2\pi}\int_{L.E.}^{x-\varepsilon}d\xi\frac{\partial}{\partial x}\int_{Y_1}^{Y_2}d\eta\frac{\Delta\phi_\zeta(\xi,\eta,+0)-\Delta\phi_\zeta(\xi,\eta,-0)}{\sqrt{(x-\xi)^2-(y-\eta)^2}}$$

$$= -\frac{1}{2\pi}\left[\Delta\phi_\zeta(\xi,\eta,+0)-\Delta\phi_\zeta(\xi,\eta,-0)\right]$$

$$+\frac{1}{2\pi}\int_{L.E}^{x}d\xi\int_{Y_1}^{Y_2}d\eta\frac{x-\xi}{\sqrt{(x-\xi)^2-(y-\eta)^2}}\left[\Delta\phi_\zeta(\xi,\eta,+0)-\Delta\phi_\zeta(\xi,\eta,-0)\right]$$

(2-37)

The second term ④ on the right-hand side of Eq. (2-36) can be written as

$$④ = -\frac{1}{2\pi}\left[\Delta\phi_\zeta(\xi,\eta,+0)-\Delta\phi_\zeta(\xi,\eta,-0)\right]$$

$$+\frac{1}{2\pi}\int_{L.E}^{x}d\xi\int_{Y_1}^{Y_2}d\eta\frac{x-\xi}{\sqrt{(x-\xi)^2-(y-\eta)^2}}\left[\Delta\phi_\zeta(\xi,\eta,+0)-\Delta\phi_\zeta(\xi,\eta,-0)\right]$$

(2-38)

Since the term in the form of $z\times G(x,y)$ goes to zero as $z\to 0$, the third and the forth terms ⑤ and ⑥ on the right-hand side of Eq. (2-36) can be ignored.

Therefore, one obtains

$$\Delta u_s(x,y) = -\Delta w_s(x,y) + \frac{1}{\pi}\iint_{\tau_1} \frac{(x-\xi)\Delta w_s(\xi,\eta)}{\sqrt{(x-\xi)^2-(y-\eta)^2}^{\,3}} d\xi d\eta$$

(2-39)

$$\Delta u_s(x,y) = \Delta\phi_x(x,y,+0) + \Delta\phi_x(x,y,-0) \tag{2-40}$$

$$\Delta w_s(x,y) = \Delta\phi_z(x,y,+0) - \Delta\phi_z(x,y,-0) \tag{2-41}$$

Similarly, by differentiating both side of Eq. (2-35) with respect to z and by adding the value of the resulting $\Delta\phi_z(x,y,z)$ at $z=+0$ and $z=-0$, one obtains

$$\Delta\phi_z(x,y,+0) + \Delta\phi_z(x,y,-0)$$

$$= -\frac{1}{2\pi}\lim_{z\to+0}\frac{\partial}{\partial z}\iint_{\tau_1}\frac{1}{\sqrt{(x-\xi)^2-(y-\eta)^2-z^2}}\left[\Delta\phi_\zeta(\xi,\eta,+0)-\Delta\phi_\zeta(\xi,\eta,-0)\right]d\xi d\eta \quad \to ⑦$$

$$-\frac{1}{2\pi}\lim_{z\to-0}\frac{\partial}{\partial z}\iint_{\tau_1}\frac{1}{\sqrt{(x-\xi)^2-(y-\eta)^2-z^2}}\left[\Delta\phi_\zeta(\xi,\eta,+0)-\Delta\phi_\zeta(\xi,\eta,-0)\right]d\xi d\eta \quad \to ⑧$$

$$+\frac{1}{2\pi}\lim_{z\to+0}\frac{\partial}{\partial z}\iint_{\tau_1}\frac{z(x-\xi)}{\left[(y-\eta)^2+z^2\right]r_c}\left[\Delta\phi_\xi(\xi,\eta,+0)-\Delta\phi_\xi(\xi,\eta,-0)\right]d\xi d\eta \quad \to ⑨$$

$$+\frac{1}{2\pi}\lim_{z\to-0}\frac{\partial}{\partial z}\iint_{\tau_1}\frac{z(x-\xi)}{\left[(y-\eta)^2+z^2\right]r_c}\left[\Delta\phi_\xi(\xi,\eta,+0)-\Delta\phi_\xi(\xi,\eta,-0)\right]d\xi d\eta \quad \to ⑩$$

(2-42)

The first term ⑦ of the right-hand side in Eq. (2-42) can be written as

$$⑦ = -\frac{1}{2\pi}\lim_{z\to+0}\lim_{\varepsilon\to0}\frac{\partial}{\partial z}\int_{L.E.}^{x-\sqrt{z^2+\varepsilon^2}} d\xi \int_{Y_1}^{Y_2}\frac{\Delta w_s(\xi,\eta)}{\sqrt{(x-\xi)^2-(y-\eta)^2-z^2}}d\eta$$

$$\left(Y_1 = y-\sqrt{(x-\xi)^2-z^2},\ Y_2 = y+\sqrt{(x-\xi)^2-z^2}\right)$$

$$= \lim_{z\to+0}\lim_{\varepsilon\to0} -\frac{1}{2\pi}\left(\frac{-\frac{1}{2}\cdot 2z}{\sqrt{z^2+\varepsilon^2}}\right)\int_{y-\varepsilon}^{y+\varepsilon}\frac{\Delta w_s(\xi,\eta)}{\sqrt{(x-\xi)^2-(y-\eta)^2-z^2}}d\eta \qquad \to ⑪$$

$$-\lim_{z\to0}\frac{1}{2\pi}\int d\xi\frac{\partial}{\partial z}\int_{Y_1}^{Y_2}\left[\frac{\Delta w_s(\xi,\eta)}{\sqrt{(x-\xi)^2-(y-\eta)^2-z^2}}\right]d\eta \qquad \to ⑫$$

(2-43)

Furthermore,

$$⑪ = \lim_{z\to+0}\lim_{\varepsilon\to0} -\frac{1}{2\pi}\left(\frac{-\frac{1}{2}\cdot 2z}{\sqrt{z^2+\varepsilon^2}}\right)\int_{y-\varepsilon}^{y+\varepsilon}\frac{\Delta w_s(\xi,\eta)}{\sqrt{(x-\xi)^2-(y-\eta)^2-z^2}}d\eta$$

$$= -\frac{1}{2\pi}\left[-\sin^{-1}\frac{y-\eta}{\varepsilon}\right]_{y-\varepsilon}^{y+\varepsilon} = \pi \qquad (2\text{-}44)$$

and

$$⑫ = -\lim_{z\to0}\frac{1}{2\pi}\int d\xi\frac{\partial}{\partial z}\int_{Y_1}^{Y_2}\left[\frac{\Delta w_s(\xi,\eta)}{\sqrt{(x-\xi)^2-(y-\eta)^2-z^2}}\right]d\eta$$

$$= -\lim_{z\to0}\frac{1}{2\pi}\int d\xi\cdot\frac{\partial}{\partial z}\left[-\sin^{-1}\frac{y-\eta}{\sqrt{(x-\xi)^2-z^2}}\right]_{Y_1}^{Y_2}\Delta w_s(\xi,\eta)$$

$$= -\lim_{z\to0}\frac{1}{2\pi}\int d\xi\cdot\frac{\partial}{\partial z}\left(-\pi\Delta w_s(\xi,\eta)\right) = 0$$

(2-45)

thus

$$⑪ + ⑫ = \pi \qquad (2\text{-}46)$$

In the same manner, the second term ⑧ on the right-hand side in Eq. (2-42) becomes $-\pi$, and thus

$$⑦ + ⑧ = 0 \tag{2-47}$$

Since the third term ⑨ on the right-hand side of Eq. (2-42) can be modified as

$$⑨ = \frac{1}{2\pi}\lim_{z\to+0}\frac{\partial}{\partial z}\iint_{\tau_1}\frac{z(x-\xi)}{\left[(y-\eta)^2+z^2\right]r_c}\left[\Delta\phi_\xi(\xi,\eta,+0)-\Delta\phi_\xi(\xi,\eta,-0)\right]d\xi d\eta$$

$$\left(\text{where}\quad Y_{1,2}=y\mp\sqrt{(x-\xi)^2-z^2}\right)$$

$$=\lim_{z\to+0}\lim_{\varepsilon\to 0}\frac{1}{2\pi}\cdot\left(-\frac{\frac{1}{2}2z}{\sqrt{z^2+\varepsilon^2}}\right)\int_{y-\varepsilon}^{y+\varepsilon}\frac{z\sqrt{z^2+\varepsilon^2}\cdot\Delta u_a(\xi,\eta)}{\left[(y-\eta)^2+z^2\right]\sqrt{\varepsilon^2-(y-\eta)^2}}d\eta$$

$$+\lim_{z\to+0}\frac{1}{2\pi}\int d\xi\frac{\partial}{\partial z}\int_{Y_1}^{Y_2}\frac{z(x-\xi)\cdot\Delta u_a(\xi,\eta)}{\left[(y-\eta)^2+z^2\right]\sqrt{(x-\xi)^2-(y-\eta)^2-z^2}}d\eta$$

$$=\lim_{z\to+0}\frac{1}{2\pi}\left(-\frac{z}{\sqrt{z^2+\varepsilon^2}}\cdot z\frac{\sqrt{z^2+\varepsilon^2}}{(\varepsilon\theta)^2+z^2}\right)\int_{y-\varepsilon}^{y+\varepsilon}\frac{\Delta u_a(\xi,\eta)}{\sqrt{\varepsilon^2-(y-\eta)^2}}d\eta$$

$$+\lim_{z\to+0}\frac{1}{2\pi}\int d\xi\frac{\partial}{\partial z}\int_{Y_1}^{Y_2}\frac{z(x-\xi)\cdot\Delta u_a(\xi,\eta)}{\left[(y-\eta)^2+z^2\right]\sqrt{(x-\xi)^2-(y-\eta)^2-z^2}}d\eta$$

$$=-\frac{1}{2}\Delta u_a(\xi,\eta)+\frac{1}{2\pi}\int d\xi\int d\eta\frac{(x-\xi)\cdot\Delta u_a(\xi,\eta)}{(y-\eta)^2\sqrt{(x-\xi)^2-(y-\eta)^2}}$$

(2-48)

The third term ⑨ can be added to the fourth term ⑩ as

$$⑨ + ⑩ = -\Delta u_a(x,y)+\frac{1}{\pi}\int d\xi\int d\eta\frac{(x-\xi)\Delta u_a(\xi,\eta)}{(y-\eta)^2\sqrt{(x-\xi)^2-(y-\eta)^2}} \tag{2-49}$$

Therefore, one obtains

$$\Delta w_a(x,y) = -\Delta u_a(x,y) + \frac{1}{\pi}\iint_{\tau_1} \frac{(x-\xi)\Delta u(\xi,\eta)}{(y-\eta)^2\sqrt{(x-\xi)^2-(y-\eta)^2}}\, d\xi d\eta$$

(2-50)

$$\Delta u_a(x,y) = \Delta\phi_x(x,y,+0) - \Delta\phi_x(x,y,-0) \qquad (2\text{-}51)$$

$$\Delta w_a(x,y) = \Delta\phi_z(x,y,+0) + \Delta\phi_z(x,y,-0) \qquad (2\text{-}52)$$

By solving Eqs. (2-39) and (2-50) with the boundary conditions Δu_s and Δu_a, the geometry related terms Δw_s and Δw_a can be obtained. The original boundary condition, Eq. (2-12), is now transformed to Eqs. (2-40) and (2-51). The geometry correction, Eq. (2-13), is finally given by Eqs. (2-41) and (2-52) where Δw_s and Δw_a represent the derivatives of the thickness and camber corrections, respectively.

The integrated value of the thickness correction in itself, however, does not satisfy the closure condition at the trailing edge. In this study, Δw_s are modified so as to satisfy the closure condition at the trailing edge. Modification is performed by the following equation;

$$\Delta w_s^{\mathrm{mod}}(x,y) = \Delta w_s(x,y) - \frac{\int_{L.E.}^{T.E.} \Delta w_s(\xi,y)d\xi}{\overline{dx}} \times \frac{dx}{l} \qquad (2\text{-}53)$$

where l is a local chord length and $\overline{dx}$ is a chord length divided by number of panels at each spanwise location.

Then, the geometry correction can be computed by performing the numerical integration in the x direction.

$$\Delta z_{\pm}(x,y) = \frac{1}{2}\int_{L.E}^{x} \Delta w_a(\xi,y)d\xi \pm \frac{1}{2}\int_{L.E.}^{x} \Delta w_s^{\mathrm{mod}}(\xi,y)d\xi \qquad (2\text{-}54)$$

By the way, since the Eqs. (2-39) and (2-50) are based on the linearized potential equation, they become invalid where the vorticity is generated. Such regions are typically around the root and tip of the wing. At the wing root, the bilateral symmetry is usually assumed for the flow analysis, but $\frac{\partial p}{\partial y} \neq 0$ for prescribing a pressure distribution on a swept wing. This breaks the irrotational flow assumption at the wing root. At the wing tip, on the other hand, the flow is naturally rotational due to the wing tip vortex. Thus, Eqs. (2-39) and (2-50) are replaced with the lower order approximations in those regions.

$$\Delta u_s(x,y) = -\Delta w_s(x,y) \tag{2-55}$$

$$\Delta w_a(x,y) = -\Delta u_a(x,y) \tag{2-56}$$

These equations are referred as the supersonic linearized pressure coefficient equation [11].

II-3. Inverse Design Procedure

The inverse problem for an aerodynamic shape design is to find a geometry that yields a specified surface pressure distribution. The procedure of finding the corresponding geometry based on the iterative “residual-correction” concept is illustrated in Fig. 2-3. First, a target pressure distribution and an arbitrary initial geometry is selected. The flow analysis is performed for the initial wing geometry to obtain the pressure distribution. In the present design system, the flow analysis stage and the inverse design stage are separated from each other, thus any type of analysis code, even an experiment, can be used for the flow analysis. In this study, an Euler code is used. After the flow analysis, the difference between the computed and the target pressure distributions is calculated. Using this pressure difference as a boundary condition, the geometry correction is obtained through the solution of the integrodifferential linearized small perturbation (LSP) equation derived in the previous section. By Adding the geometry correction to the initial geometry, a new geometry is produced. This process will be iterated until ΔC_P becomes sufficiently small.

II-4. Validation of Supersonic Inverse Design Method

To validate the formulation of the present supersonic inverse method, design tests are performed. The present wing planform is taken from the extended NAL's 2nd baseline configuration of the scaled supersonic experimental airplane program [12]. To make isolated wing planform, the wing root is extended to the centerline of the body. As shown in Fig. 2-4, the leading-edge sweep angle is about 70° and the leading- and trailing-edge kinks are located at 43.9% and 40% spanwise sections, respectively.

For the inverse design, this wing planform should be divided into panels. In Takanashi's transonic wing design, the planform is divide into panels with a constant size. However, in case of supersonic wing design, the use of the constant panel size is inappropriate since the taper ratio of planform is very small. Thus, in this case, the chordwise length of panels becomes toward smaller the tip while the spanwise length of panels remains constant. In this study, there are 50 panels in the chordwise direction and 67 in the spanwise direction.

Using NACA1204 and NACA0003 airfoil sections, two wings are created. For these wings, the Euler analysis is performed. The Euler code used here utilizes a TVD upwind scheme for the spatial discretization of the convective terms and the LU-SGS method [13] for the time integration. The topology of the grid is the C-H type with a two-dimensional C type grid at each spanwise section. The computational grid is generated by an algebraic grid generator.

The pressure distribution on the wing based on NACA1204 airfoil is designated to the target pressure. The inverse design started from a wing with NACA0003 sections as the initial geometry. The design condition is a Mach number of 2.0 and an angle of attack of 2.0° . The design result is shown in Fig. 2-5. The chordwise pressure distributions and the corresponding airfoil geometries at the 20, 40, 70 and 90% spanwise sections of the target, initial and designed wings after 9 inverse cycles are plotted. Except at the 90% spanwise section, pressure distributions of the designed wing coincide with those of the target wing. Maybe the discrepancies near the tip are attributed to the invalidity of the irrotational assumption of the original small perturbation equation there.

In order to improve the overall convergence, Eqs. (2-37) and (2-48) are replaced with the supersonic linearized pressure coefficient equations (2-53) and (2-54) near the root and tip sections where the original linearized small perturbation equation does not stand. Figure 2-6 shows the area to be dealt with the integral equations and the supersonic linearized coefficient equations. The corresponding design results are shown in Fig. 2-7. The designed and target pressures coincide with each other even at the 90%

spanwise section. To check the convergence, residual pressure differences ($\overline{\Delta C_p}$) averaged at each spanwise section after 9 inverse design cycles are plotted in Fig. 2-8. As shown in the figure, the integral equation derived here gives the best convergence in the midspan from 30% to 70% spanwise sections. On the other hand, near the root and tip, it gives the worst convergence due to the irrelevant physics. The lower order correction based on the supersonic linearized pressure coefficient equation is shown to give the better convergence there. Thus, by switching the both equations, the overall convergence is greatly improved. These design results confirmed the validity of the present method.

II-5. Summary

A supersonic inverse design method was developed in this chapter. The integrodifferential form of the governing equation was derived. The inverse design was executed by integrating this equation numerically on the wing surface. The method was extended from Takanashi's transonic inverse method. Since the present method designs camber and thickness corrections at the same time, the nonlinear effect due to the thickness distribution to the camber surface is accounted for.

In case of three-dimensional problems, the present method was revised by using the supersonic linearized pressure coefficient equation near the wing root and tip where the irrotational flow assumption does not stand. This greatly improved the convergence of the inverse design. Design results confirmed the validity of the present method.

References

[1] H. W. Carlson and D. S. Miller, "Numerical Methods for the Design and Analysis of Wings at Supersonic Speed," NASA TN D-7713, 1974.

[2] K. B. Walkey and G. E. Smith, "Application of a Full Potential Method to Supersonic Aircraft Design and Analysis," *Journal of Aircraft*, Vol. 26, No. 1, pp. 6-12, January 1989.

[3] H. W. Carlson and W. D. Middleton, "A Numerical Methods for Design of Camber Surfaces of Supersonic Wings with Arbitrary Planforms," NASA TN-2341, 1964.

[4] S. Takanashi, "Iterative Three-Dimensional Transonic Wing Design Using Integral Equations," *Journal of Aircraft*, Vol. 22, No. 8, pp. 655-660, August 1985.

[5] R. F. van den Dam, "Constrained Spanload Optimization for Minimum Drag of Multi-Lifting Surface Configurations," Computational Methods for Aerodynamic Design (Inverse) and Optimization, AGARD Conference Proceedings No. 463, Reference 16, March 1990.

[6] J. A. van Egmond, "Numerical Optimization of Target Pressure Distributions for Subsonic and Transonic Airfoil Design," Computational Methods for Aerodynamic Design (Inverse) and Optimization, AGARD Conference Proceedings No. 463, Reference 17, March 1990.

[7] S. Obayashi and S. Takanashi, "Genetic Optimization of Target Pressure Distributions for Inverse Design Methods," AIAA *Journal*, Vol. 34, No. 5, pp. 881-886, May 1996.

[8] S. Obayashi, S. Jeong and Y. Matsuo, "New Blunt Trailing-Edge Airfoil Design by

Inverse Optimization Method," *Journal of Aircraft*, Vol. 34, No. 2, pp. 255-257, March-April 1997.

[9] S. Jeong, S. Obayashi, K. Nakahashi, T. Iwamiya and K. Matsushima, "Supersonic Inverse Design Method for Wing-Fuselage Design," M. Tanaka and G. S. Dulikravich (Eds.), *INVERSE PROBLEMS IN ENGINEERING MECHANICS*, Proceeding of International Symposium on Inverse Problem in Engineering Mechanics 1998, Nagano, Japan, Elsevier Science, Oxford, pp.381-389, 1998.

[10] S. Jeong, S. Obayashi, K. Nakahashi, K. Matsushima and T. Iwamiya, "Iterative Design Method for Supersonic Wings Using Integral Equations," *CFD Journal*, Vol. 7, No. 3, pp. 365-374, October 1998.

[11] N. Kamiya, H. Tamaki, N., Hirose and Y. Ishida, "On an Inverse Problem for a Supersonic Airfoils Based on Navier-Stokes Approximation," Proceedings of 14th the NAL Symposium on Aircraft Computational Aerodynamic, pp. 95-100, 1997. (in Japanese)

[12] Y. Shimbo, K. Yoshida, T. Iwamiya, R. Takaki and K. Matsushima, "Aerodynamic Design of Scaled Supersonic Experimental Airplane," Proceedings of 1st International CFD Workshop for SST Design, pp. 62-67, Tokyo, Japan, NAL, March 1998.

[13] S. Obayashi and G. P. Guruswamy, "Convergence Acceleration of a Navier-Stokes Solver for Efficient Static Aeroelastic Computations," AIAA *Journal*, Vol. 33, No. 6, pp. 1134-1141, June 1995.

[14] M. A. Heaslet, H. Lomax and A. L. Jones, "Volterra's Solutions of Wave Equations

as Applied to Three-Dimensional Supersonic Airfoil Problem," NACA Rep. 899, 1947. (Formerly NACA TN 1412)

[15] H. Lomax, M. A. Heaslet and B. F. Franklyn, "Integrals and Integral Equation in Linearized Wing Theory," NACA Rep. 1054, 1951.

[16] J. Hadamard, *Lectures on Cauchy's Problem in Linear Partial Differential Equations*, Yale University Press, 1928.

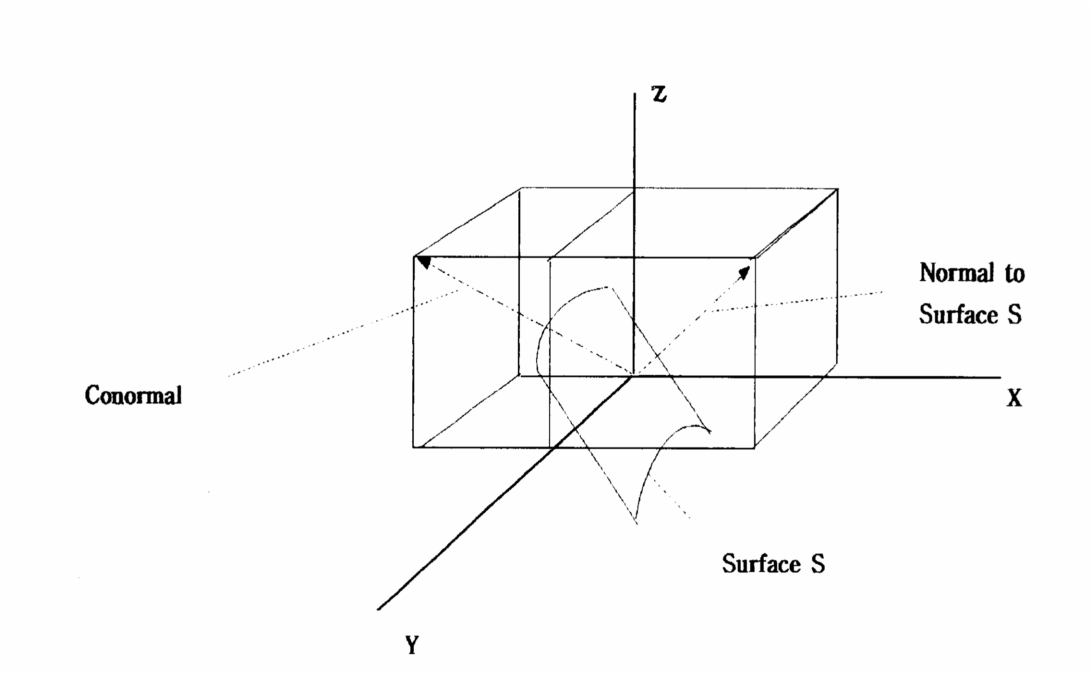

Figure 2-1. Geometry relation between normal and co-normal to surface *S*

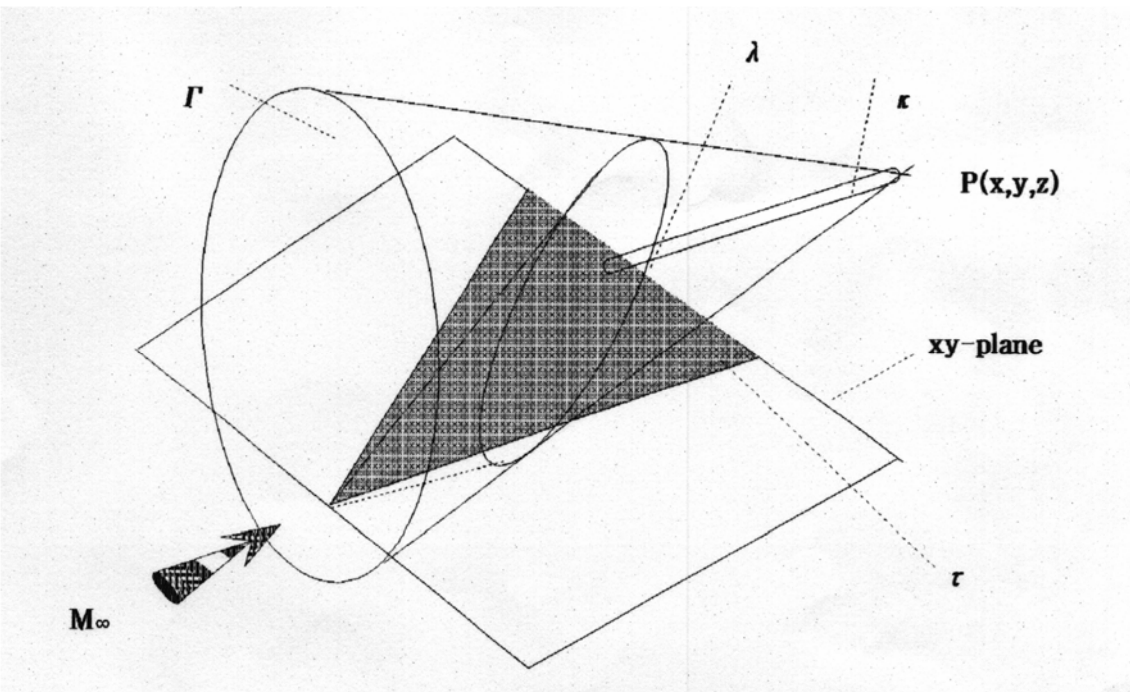

Figure 2-2. Mach forecone from point P(x,y) intersecting surface τ, triangular planform

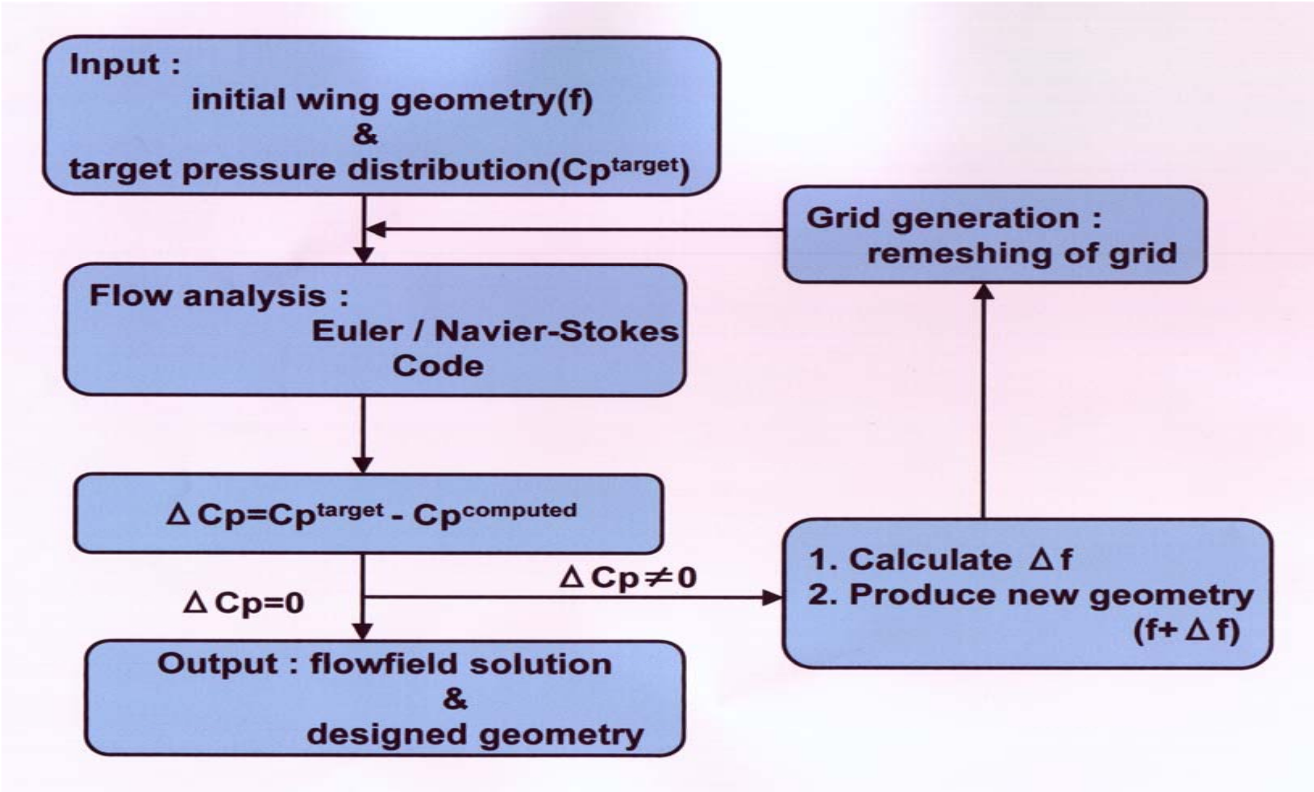

Figure 2-3. Procedure of the inverse design method based on the iterative “residual-correction” concept

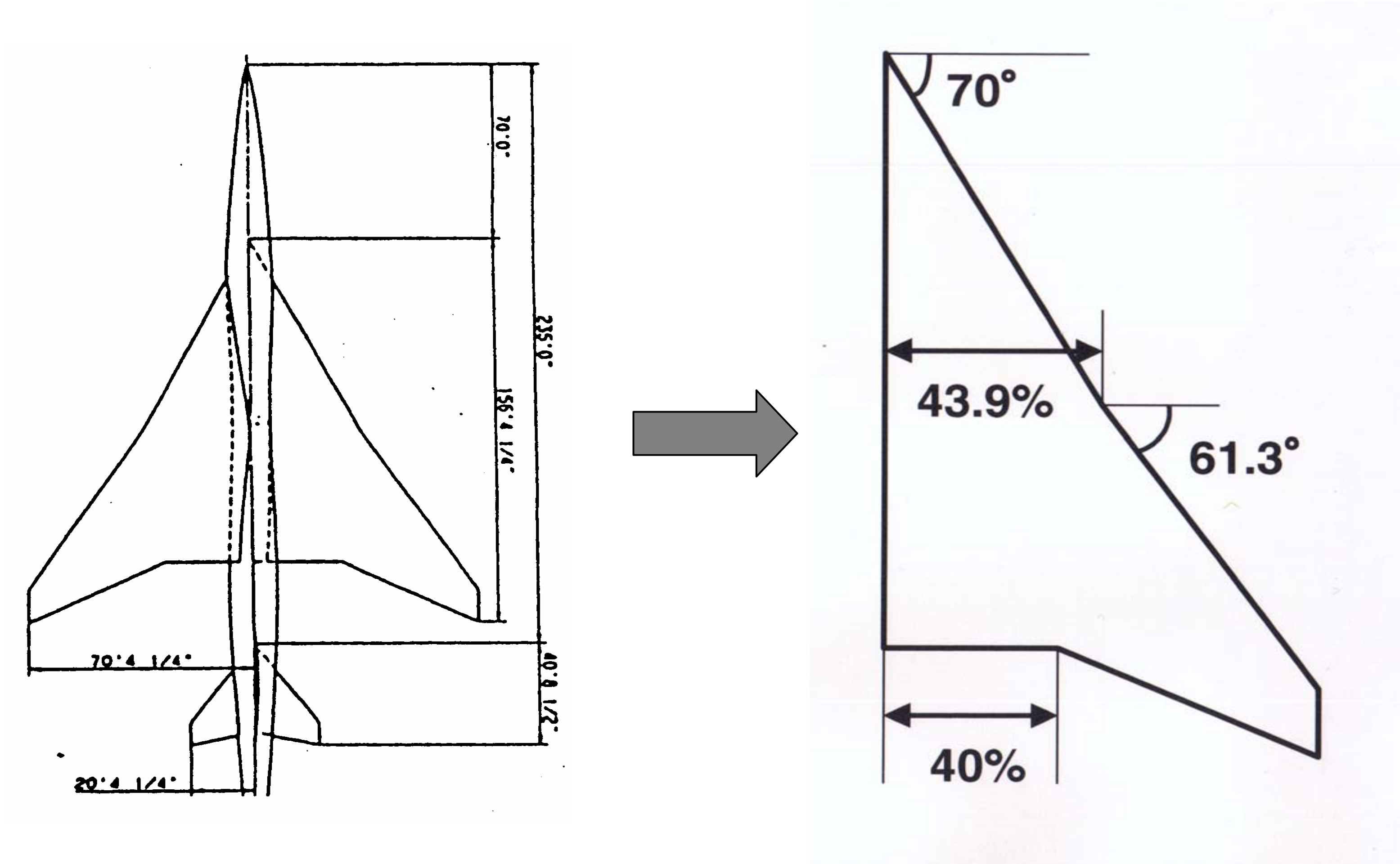

Figure 2-4. Wing planform

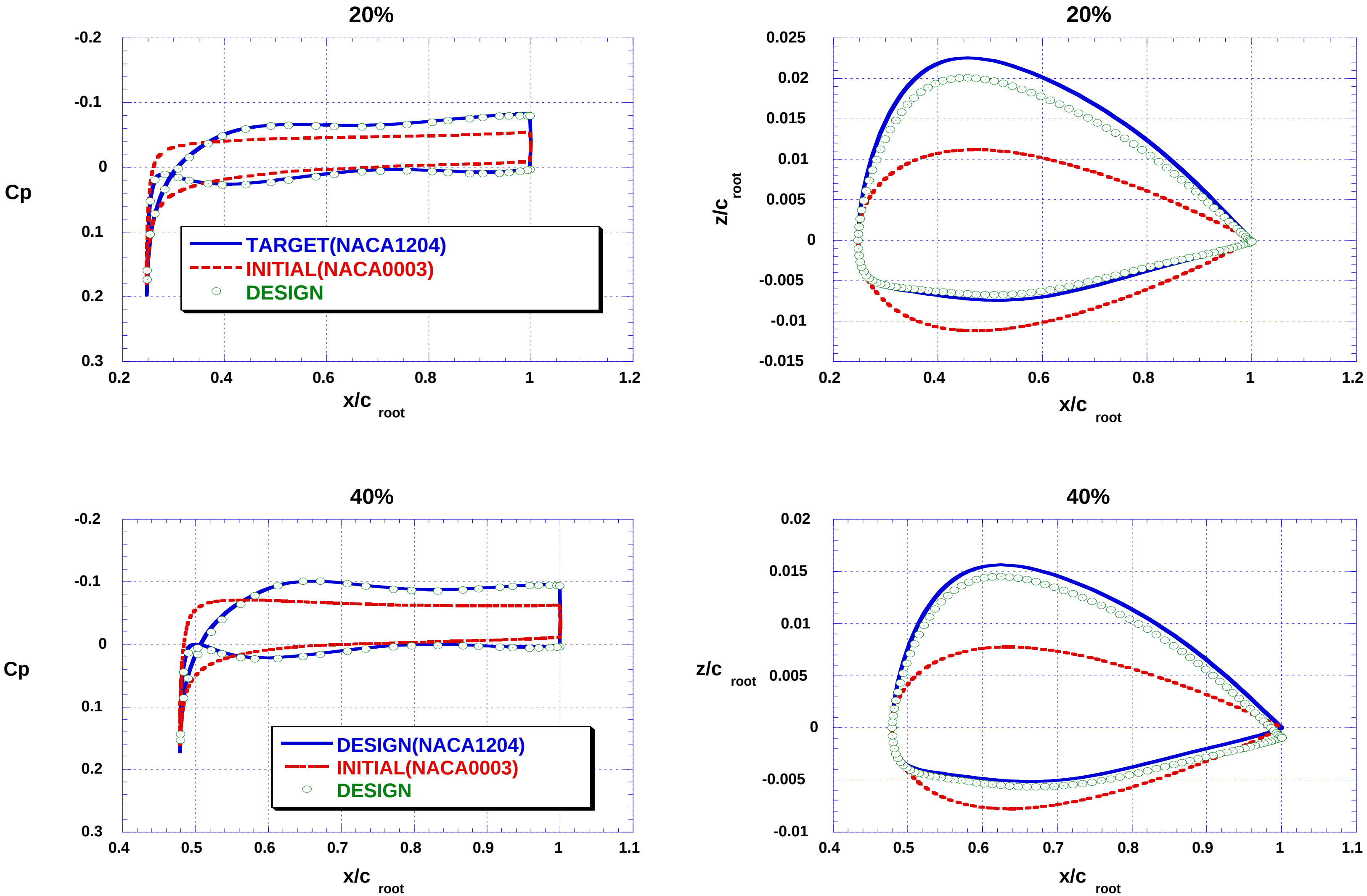

Figure 2-5. Comparison of pressure distributions and corresponding geometries among the target, initial and designed wings (1)

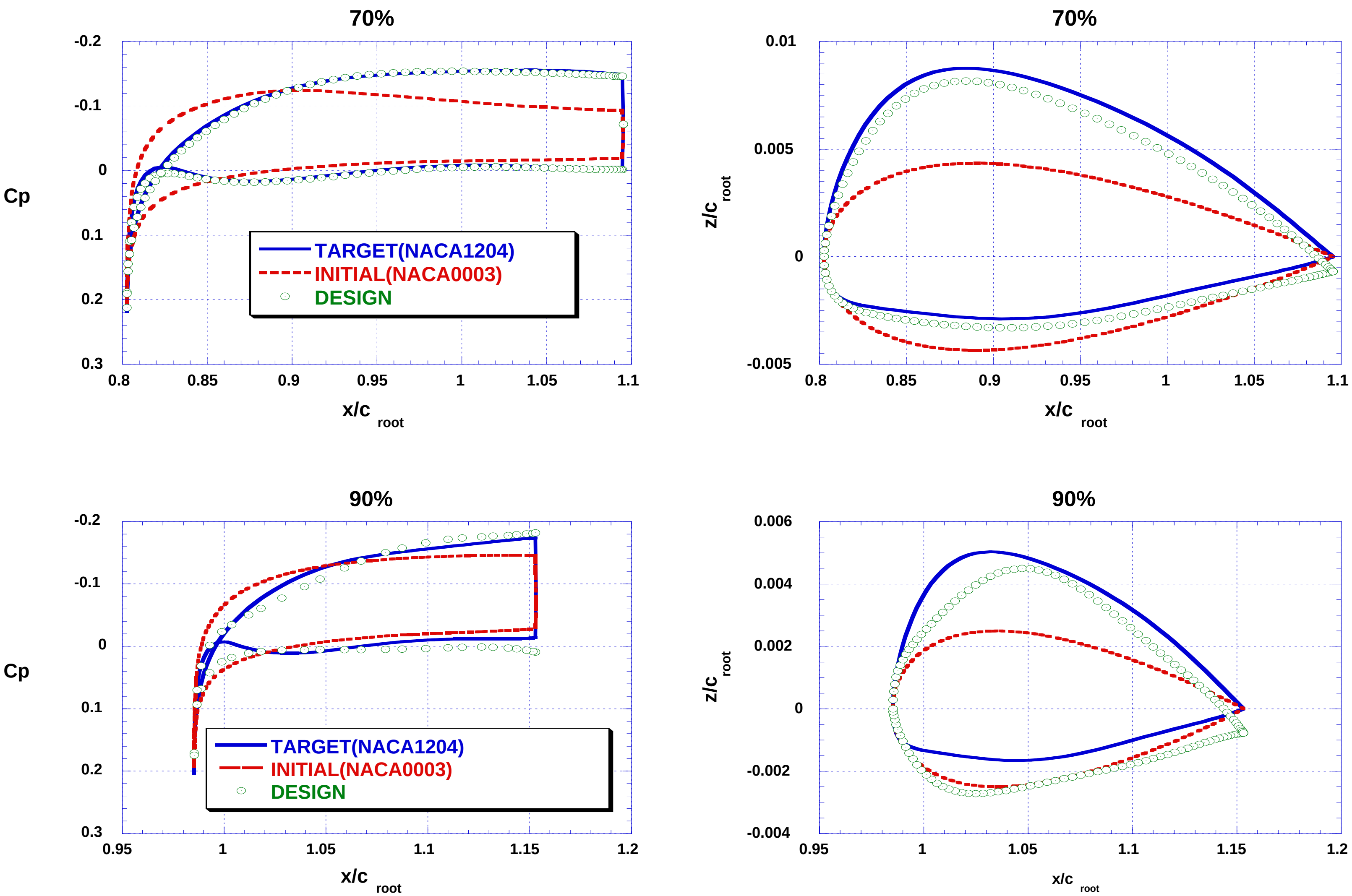

Figure 2-5. Comparison of pressure distributions and corresponding geometries among the target, initial and designed wings (2)

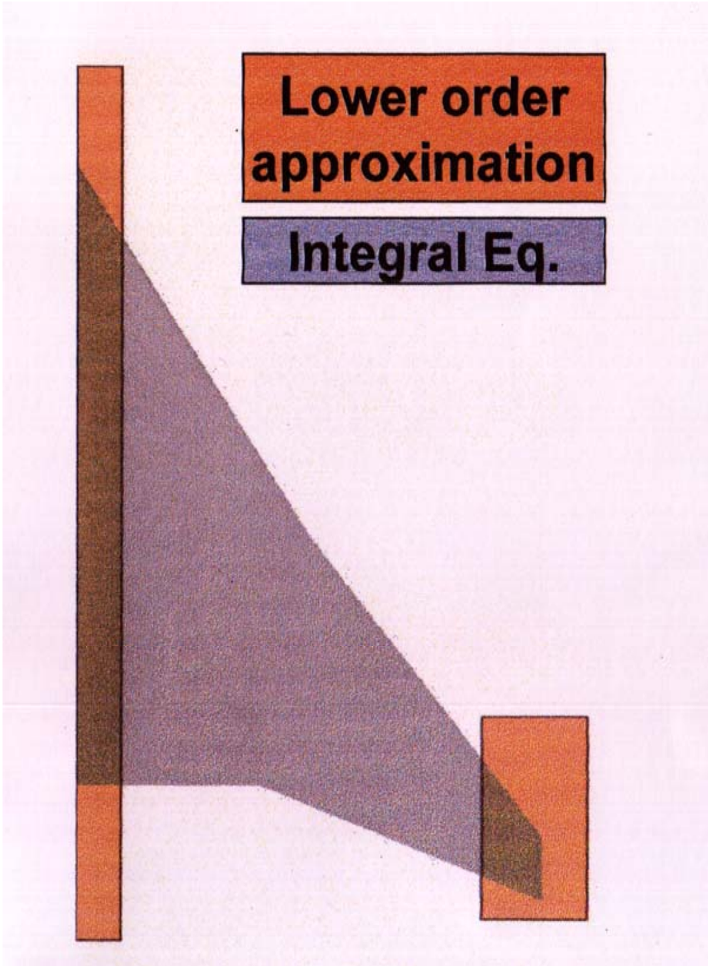

Figure 2-6. The area to be dealt with the integral equations and lower order approximations

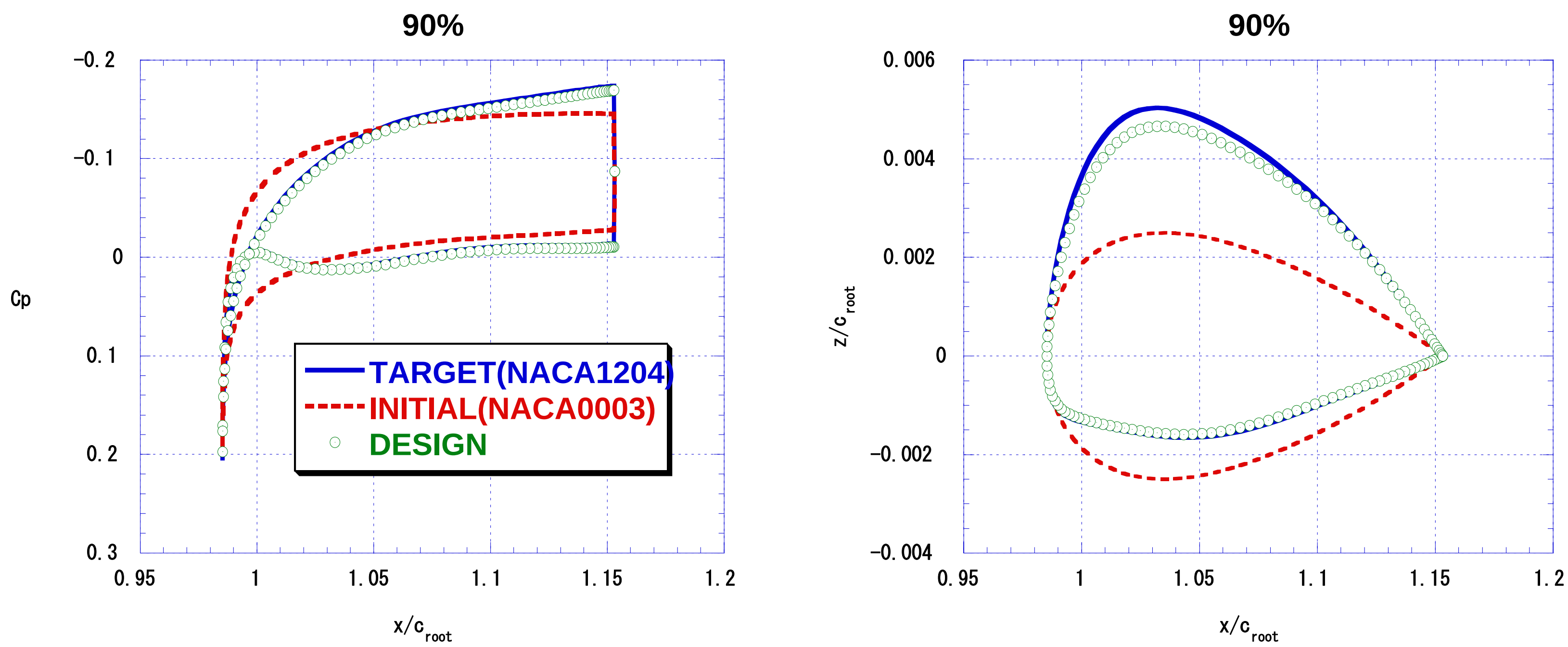

Figure 2-7. Comparison of pressure distributions and wing sections in modified inverse design

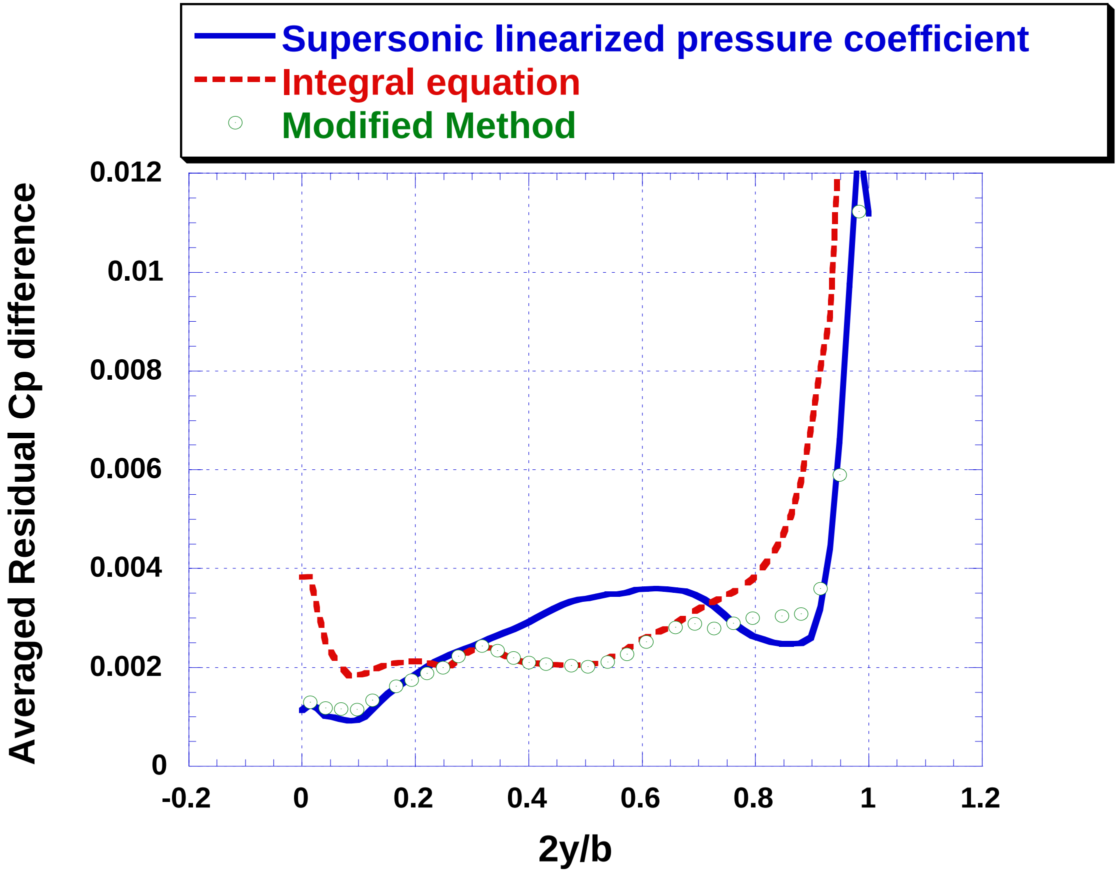

Figure 2-8. Comparison of the spanwise residuals of pressure difference

CHAPTER Ⅲ

INVERSE OPTIMIZATION OF SUPERSONIC WING DESIGN WITH TWIST SPECIFICATION

Ⅲ-1. Introduction

In case of inverse design optimization problems [1, 2], the objective of the optimization is not a geometry itself but a pressure distribution. To design a wing of a high performance, the designer must seek an optimal target pressure distribution first. Once the optimal target pressure distribution is specified, the corresponding geometry can be found through the inverse design. Thus, it is no exaggeration that the choice of a pressure distribution is the most important thing in the inverse design. In this chapter, the optimization method for the target pressure distribution will be discussed.

The most widely used optimization technique is a gradient-based method. However, since the aerodynamic design problems are strongly nonlinear and may have discontinuities in objectives as well as constraints, this method cannot meet the robustness demanded. On the other hand, Genetic Algorithms (GAs) [3, 4], one of Evolutionary Algorithms, uses only objective function information (fitness values) instead of derivatives or other auxiliary knowledge. In addition, GAs search from a population of the points not from a single point. These features make GAs robust and attractive to our aerodynamic design problems.

Furthermore, a wing twist specification technique is introduced to the supersonic inverse design method in this study by taking advantage of the non-uniqueness of three-dimensional aerodynamic inverse problems. The present non-uniqueness property means that there are more than one geometries that yield the prescribed surface pressure distribution. This non-uniqueness allows to implement an additional geometry constraint during the inverse design process, in particular, the wing twist specification.

Ⅲ-2. Design Goal & Target Pressure Distribution

One of the important design goals of SST is an improvement in the lift-to-drag ratio (L/D). To obtain higher L/D performance under the required lift, drag reduction is considered here. To achieve this goal with the inverse design method, target pressure distributions that give a low drag are studied. In general, the total drag consists of the lift dependant, friction, wave and pressure drag components. Thus, target pressure distributions for the low drag are investigated for each drag component separately here.

The first component considered is the lift-dependent drag. Theoretically, load distribution integrated in every direction must be elliptic for the minimum lift-dependent drag. However, in case of a wing with large sweptback angle, the elliptic integrated chordwise load distribution is nearly unattainable. Thus, in this investigation, the elliptic integrated load distribution is considered only in the spanwise direction. Instead of the elliptic integrated chordwise load distribution, two types of chordwise loading patterns are examined for a better target pressure distribution that produces the low lift-dependent drag. In this study, simple linear and parabolic shapes of chordwise load distribution will be tested.

The second component is the friction drag. The friction drag reaches about a half of the total drag in the fully turbulent flow. One of the strategies to reduce the friction drag is the utilization of Natural Laminar Flow (NLF) [5, 6, 7]. By preserving NLF on the wing surface as long as possible, the friction drag can be reduced. For a wing with a large sweptback angle as used for SSTs, the crossflow instability can be a trigger of the transition to turbulent as well as the Tollmien-Schliching instability. To minimize the crossflow instability, the pressure distribution should have a rapid drop at the leading edge followed by a flat distribution toward the trailing edge.

The shape of the target pressure distribution for the wave drag reduction is not considered here because it wholly depends on the shape of the wing planform. In our design, wave drag reduction will be achieved by using the planform that has a subsonic leading edge. Furthermore, flow separation can be easily avoided due to the supersonic trailing edge of the present planform.

Ⅲ-3. Genetic Algorithms for Multiple Objective (MO) Problems

The optimization problem to obtain the low drag target pressure distribution can defined as

Minimize:

1. Difference of local lift coefficients $C_L(y)$ to the elliptic spanwise load distribution at 10 spanwise locations from the root to the tip of the wing

$$diff = \sum_{root}^{tip} \left| C_L(y) - C_L^{elliptic}(y) \right| \tag{3-1}$$

2. Penalty function F ($F = f_1^{penalty} + f_2^{penalty}$) due to the constraints for natural laminar flow

$$f_1^{penalty} = k_1 \times \left[\min\left(\left.\frac{dC_{p,u}}{dx}\right|_{L.E.}, C_1 \right) - C_1 \right]^2 \tag{3-2}$$

$$f_2^{penalty} = k_2 \times \left[\max\left(\left.\frac{dC_{p,u}}{dx}\right|_{L.E.\to T.E.}, C_2 \right) - C_2 \right]^2 \tag{3-3}$$

(k_1 and k_2 are weighting constants and C_1 and C_2 are constants for tolerance limits, $C_1 = 0.02, C_2 = 0.0065$).

Subject to $C_L = 0.1$.

The defined problem here is a Multiple Objective (MO) problem [8, 9]. Unlike the single objective problem, the solution of the MO problem is not a single point, but a family of points known as Pareto-optimal solutions. Each point in this Pareto set is optimal in the sense that no improvement can be achieved in any objective without degradation in the others.

The definition of Pareto optimality is as follow:

Suppose $x^0, x^1, x^2 \in X$ (X is a feasible region of the problem.) and $f = \left(f_1, \cdots, f_p\right)$ is the set of objective functions to be minimized,

1. x^1 is said to be *dominated* by x^2, if $f(x^1)$ is partially less than $f(x^2)$, i.e., $f_i\left(x^1\right) \geq f_i\left(x^2\right)$, for $\forall i = 1, \cdots, p$, and $f_i\left(x^1\right) > f_i\left(x^2\right)$ for $\exists i = 1, \cdots, p$.

2. x^0 is *Pareto optimal*, if there doesn't exist any $x \in X$ such that x dominates x^0.

In Fig. 3-1, the Pareto-optimal solutions to a two-objective problem are illustrated.

Since a Pareto-optimal set represents rational solutions to the MO problem, the MO solvers are desired to find multiple Pareto solutions in parallel. To meet such a demand, the Pareto-ranking approach where selection/production is performed by referring not to the fitness values but to the dominance property is introduced to Multiple-Objective GAs [3, 9].

Additional aspect of such MO solvers is a capability to sample solutions uniformly from the Pareto-optimal set. To retain such a property, it is needed to maintain genetic diversity. Therefore, the fitness sharing method is also applied to MOGA [9, 10]. In the fitness sharing method, the fitness value of each individual is reduced if there exist other individuals in its neighborhood, and therefore an individual located in more crowed area leaves less offspring. Thus, the populations distributed more uniformly over the Pareto-optimal set can be obtained.

The pressure distribution is defined by B-spline parameterization [11, 12]. Seven points are used to control the upper and the lower surface of the pressure distribution respectively, as design variables of the present optimization problem. In the spanwise direction, 10 sections are considered.

The present MOGA runs for 100 generations with 100 individuals. Figures 3-2 and 3-3 show the optimized target pressure distribution at the 90% spanwise section and its integrated spanwise load distribution, respectively.

Ⅲ-4. Design Results

Once the target pressure distribution is optimized by GA, the corresponding geometry can be obtained through the inverse code. In this investigation, two target pressure distributions are considered. The difference between the two target pressure distributions is the chordwise loading pattern. One is linear and the other is a parabolic shape. Figure 3-4 shows the chordwise loading patterns used in this study. Both target pressure distributions have a rapid pressure drop at the leading edge followed by a flat distribution for NLF and their integrated spanwise load distributions are elliptic for the reduction of the lift-dependent drag as show in Figs. 3-2 and 3-3. In the both designs, the extended NAL's 2nd baseline configuration is used as the initial geometry. The design condition is M=2.0 and $\alpha=2^\circ$. The flow analysis code and the computational grid generator are the same as in the previous chapter.

Linear chordwise load distribution

Design results after 9 iteration cycles are shown in Fig. 3-5. The chordwise pressure distributions and the corresponding airfoil geometries at the 20, 40, 60 and 80% spanwise sections of the target, initial and designed wing are plotted. As shown in the figure, the pressure distribution of the designed wing converged to the optimized target pressure distribution very well at all spanwise sections. The integrated spanwise load distribution of the designed wing is plotted in Fig. 3-6. This also converged to the elliptic load distribution. Figure 3-7 shows pressure contours on the upper and the lower surface of the designed wing. The flat chordwise pressure distribution is realized on the upper surface. The isobar pattern is formed along the chordwise direction on the upper surface of the wing due to the elliptic loading.

The performance of the designed wing is compared with NAL's 2nd configuration of which the fundamental design tool was Carlson's method [13]. Figure 3-8 presents C_L vs. alpha and C_D vs. alpha. The lift curve of the designed wing is almost the same as that of NAL's second configuration while the corresponding drag polar is lower than that of NAL's 2nd configuration. Table 3-1 summaries the comparison of C_L, C_D and L/D at design the point. The lift-to-drag ratio of the designed wing is greatly improved.

Parabolic chordwise load distribution

Design results by using a parabolic chordwise load distribution are shown in Fig. 3-9. The chordwise pressure distributions and the corresponding airfoil geometries at the 20, 40, 60 and 80% spanwise sections of the target, initial and designed wing are plotted. The pressure distribution at each spanwise section converged to that of the target. As shown in Fig. 3-10, the integrated spanwise load distribution also appears elliptic. In Table 3-2, the C_L, C_D and L/D of the designed wing are compared with those of NAL's 2nd wing. Unlike the linear chordwise loading case, L/D decreases slightly. From these results, in this practical design problem, the linear chordwise load distribution is considered better for the lift-dependent drag reduction.

Ⅲ-5. Twist Specified Inverse Design (TSID)

In Fig. 3-11, the trailing-edge line of the designed wing is plotted. From the manufacturer's point of view, it will be very difficult to process such a wavy configuration precisely. More smooth and simple geometry is preferable. To eliminate a wavy design, the non-uniqueness of the three-dimensional aerodynamic inverse problem is utilized here.

The non-uniqueness means that there are more than one geometry solutions yielding the prescribed target pressure distribution as illustrated in Fig. 3-12. Then, a designer may be able to choose a favorable geometry among these solution geometries. The present inverse method cannot find a favorable geometry by itself. An additional geometry constraint is thus required. In this study, a wing twist specification is applied to the present inverse method as an additional geometry constraint.

The procedure of the twist specification inverse design (TSID) is shown in Fig. 3-13. In the present TSID:

1. The initial wing geometry must have the same wing twist expected to be designed.
2. The corrected camber line is rotated around the leading edge to maintain the specified wing twist.

TSID was performed with the same target pressure distribution used in the linear chordwise loading case. The design condition is M=2.0 and $\alpha = 2.0^\circ$. The trailing-edge line of the initial wing used in TSID is compared with that of the twist-free design results in Fig. 3-14. The trailing line of the twist specification design is much smoother than that of the twist-free design.

Figure 3-15 shows comparisons of pressure distributions and wing sections between the twist-specified design and the twist-free design. Although the pressure distributions coincide with each other, the corresponding wing sections are different. By using TSID design, the wing geometry that has the specified twist is obtained.

Ⅲ-6. Summary

In this chapter, the optimization method for target pressure distribution was investigated. GA used the Pareto-ranking approach and the fitness sharing method for the successful application to the Multiple Objective problems.

The shapes of target pressure distributions that give minimum drag have been studied. For the lift-dependent drag reduction, elliptic spanwise loading was specified. The chordwise loading patterns were also examined. As a result, in practical design problems, the linear chordwise loading pattern found a better for the lift-dependent drag reduction. For the friction reduction, the Natural Laminar Flow concept was applied.

In addition, the twist specification technique was introduced to the supersonic inverse design method by taking advantage of the non-uniqueness of the three-dimensional aerodynamic inverse problems. This made it possible for a designer to select a favorable geometry among the many solution geometries of the three-dimensional aerodynamic inverse problem. In other words, the twist of the initial wing can be maintained throughout the inverse design. Thus, a favorable wing can be designed by choosing such an initial wing with a smooth trailing edge line. The design result confirmed the usefulness of the TSID design over the twist-free design.

References

[1] S. Obayashi, S. Jeong and Y. Matsuo, "New Blunt Trailing-Edge Airfoil Design by Inverse Optimization Method," *Journal of Aircraft*, Vol. 34, No. 2, pp. 255-257, March-April 1997.

[2] H. Kim and O. Rho, "Aerodynamic Design of Transonic Wing Using the Target Pressure Optimization Approach," AIAA Paper, 98-0599-CP, 1998.

[3] D. E. Goldberg, *Genetic Algorithms in Search, Optimization & Machine Learning*, Addison-Wesley Publishing, Inc., Reading, January 1989.

[4] Z. Michalewicz, *Genetic Algorithms + Data Structure = Evolutionary Program*, Second extended edition, Springer-Verlag, Berlin, 1994.

[5] K. Yoshida, H. Ogoshi, Y. Ishida and M. Noguchi, "Numerical Study on Transition Prediction Method and Experimental Study on Effect of Supersonic Laminar Flow Control," NAL SP-31, 1996.

[6] B. E. Green, J. L. Whitesides, R. L. Campbell and R. E. Mineck, "Method for the Constrained Design of Natural Laminar Flow Airfoil," *Journal of Aircraft*, Vol. 34, No. 6, pp. 706-712, November-December 1997.

[7] Y. Shimbo, K. Yoshida, T. Iwamiya, R. Takaki and K. Matsushima, "Aerodynamic Design of the Scaled Supersonic Experimental Airplane," Proceedings of International CFD Workshop for SST Design, pp. 62-67, Tokyo, Japan, NAL, March, 1998.

[8] H. Tamaki, H. Kita and S. Kobayashi, "Multi-Objective Optimization by Genetic Algorithms: A Review," Proceedings of 1996 IEEE International Conference on

Evolutionary Computation, pp. 517-522, 1996.

[9] C. M. Fonseca and P. J. Fleming, “Genetic Algorithms for Multiobjective Optimization: Formulation, Discussion and Generalization,” Proceedings of 5th ICGA, pp. 416-423, 1993.

[10] S. Obayashi, S. Takahashi and Y. Takeguchi, "Niching and Elitist Models for MOGAs," Parallel Problem Solving from Nature - PPSN V, Lecture Notes in Computer Science, Springer, Berlin, pp. 260-269, September 1998.

[11] D. F. Rogers and J. A. Adams, *Mathematical Elements for Computer Graphics*, Second Edition, Mcgraw-Hill, Inc, New York,1990.

[12] V. B. Anand, *Computational Graphics and Geometry Modeling for Engineers*, First Edition, Jonn Wiley & Sons, Inc, New York, 1993

[13] H. W. Carlson and D. S. Miller, “Numerical Methods for the Design and Analysis of Wings at Supersonic Speed,” NASA TN D-7713, 1974.

[14] D. Küchemann, *The Aerodynamic Design of Aircraft*, Pergamon Press, Oxford, 1978.

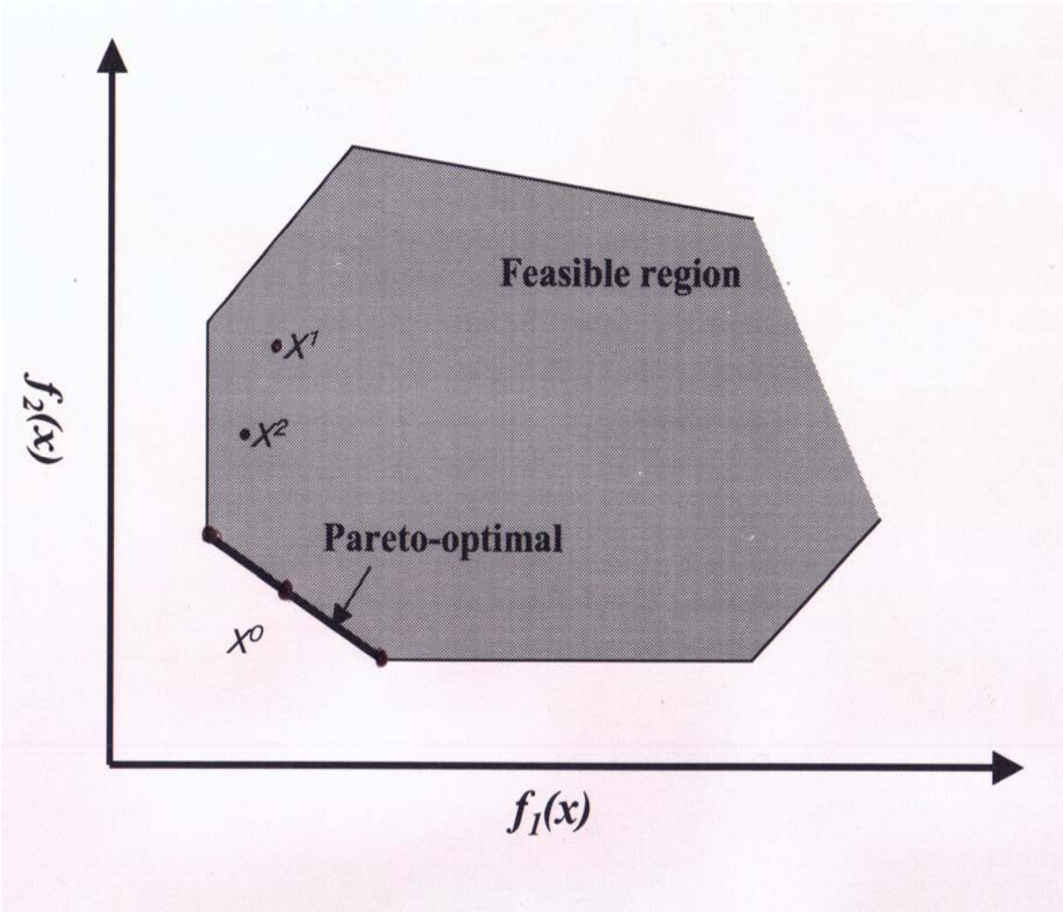

Figure 3-1. Feasible region of function space and the Pareto-optimal solutions

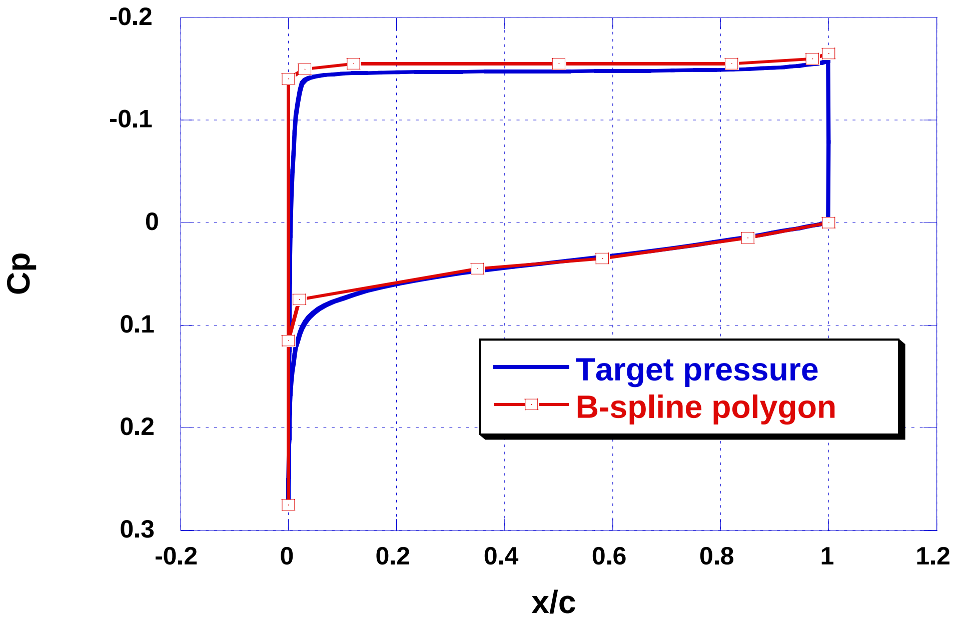

Figure 3-2. Representation of chordwise target pressure distribution at 90% spanwise section

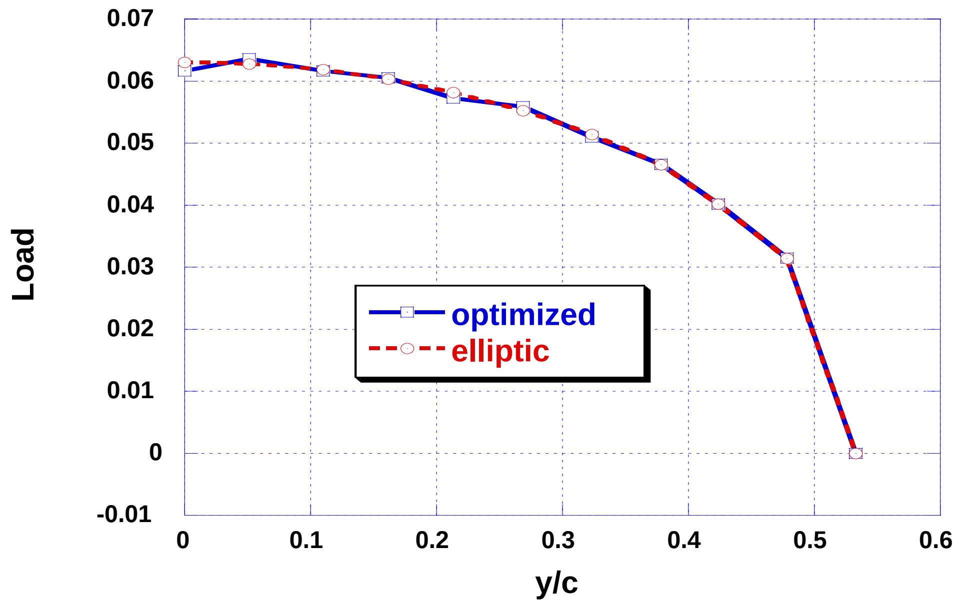

Figure 3-3. Spanwise load distribution of the target pressure distribution

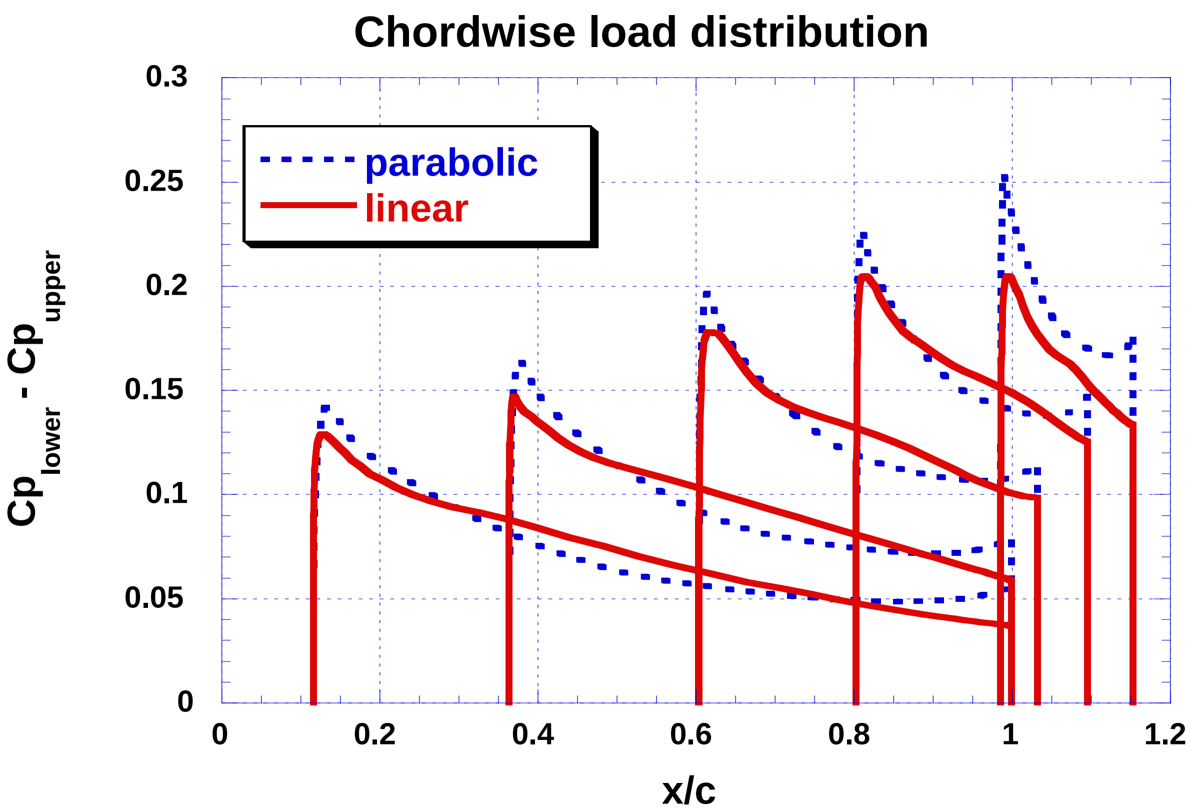

Figure 3-4. Chordwise loading patterns of target pressure distributions

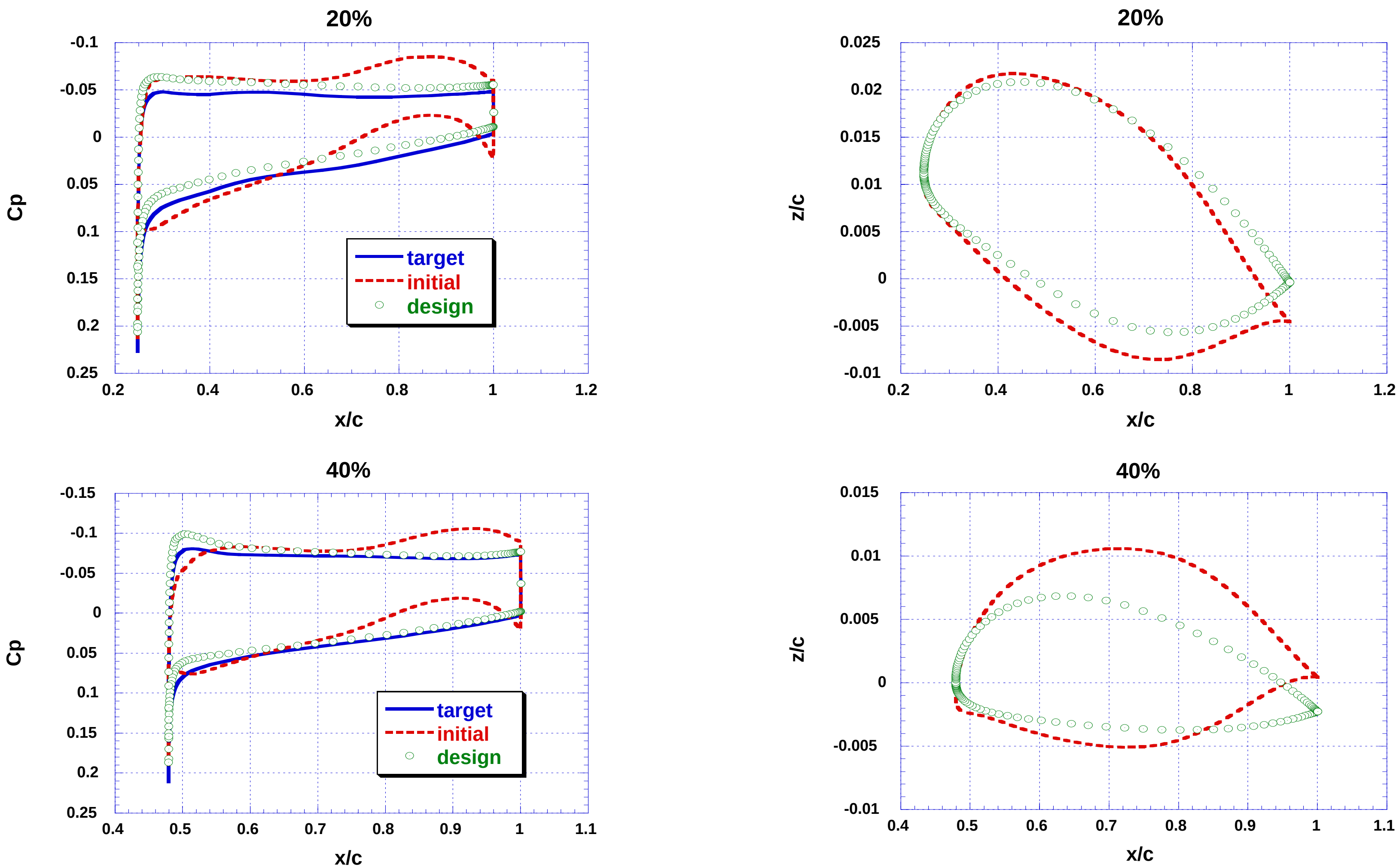

Figure 3-5. Comparison of pressure distributions and corresponding geometries among the target, initial and designed wings (1)

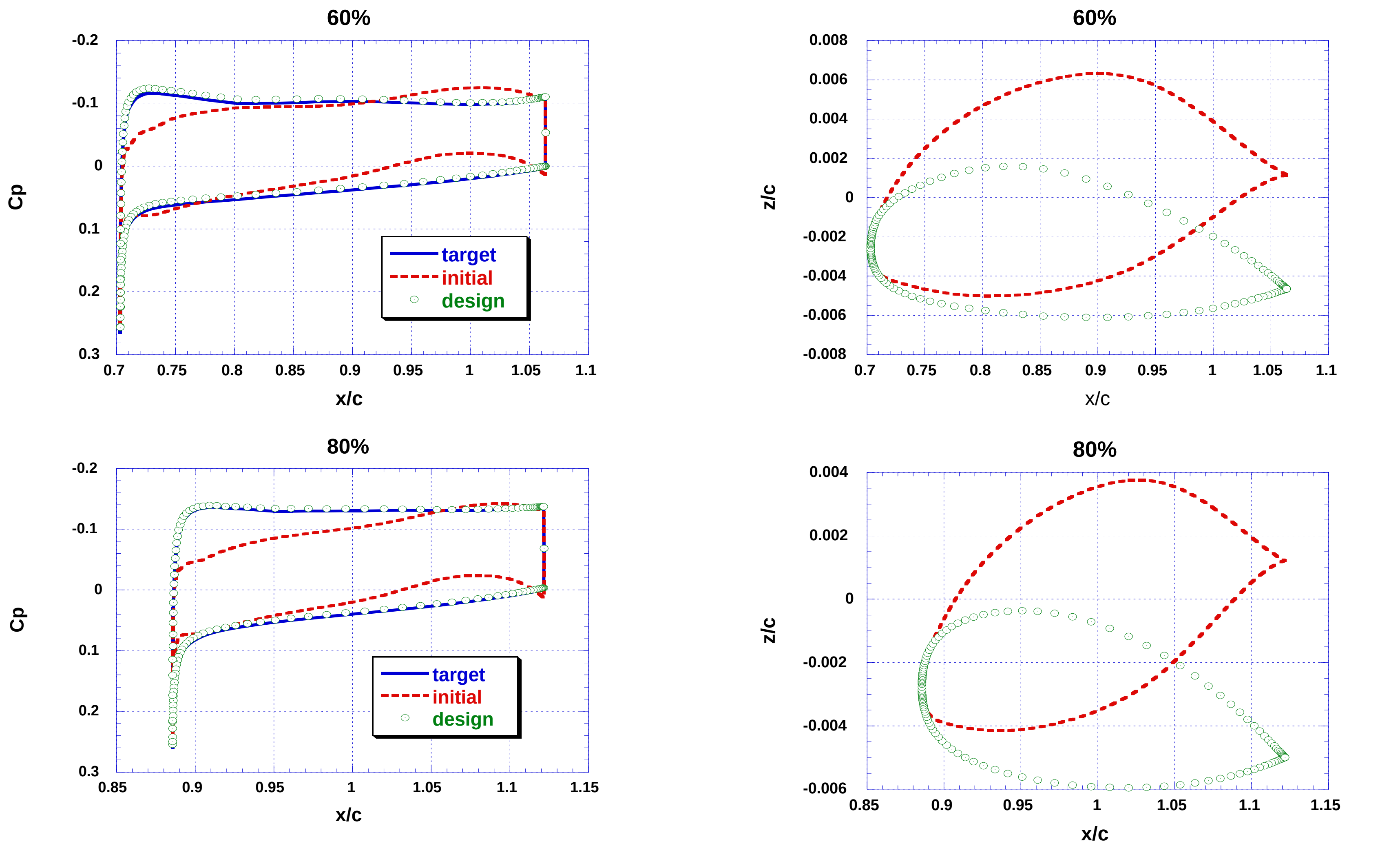

Figure 3-5. Comparison of pressure distributions and corresponding wing geometries among the target, initial and designed wings (2)

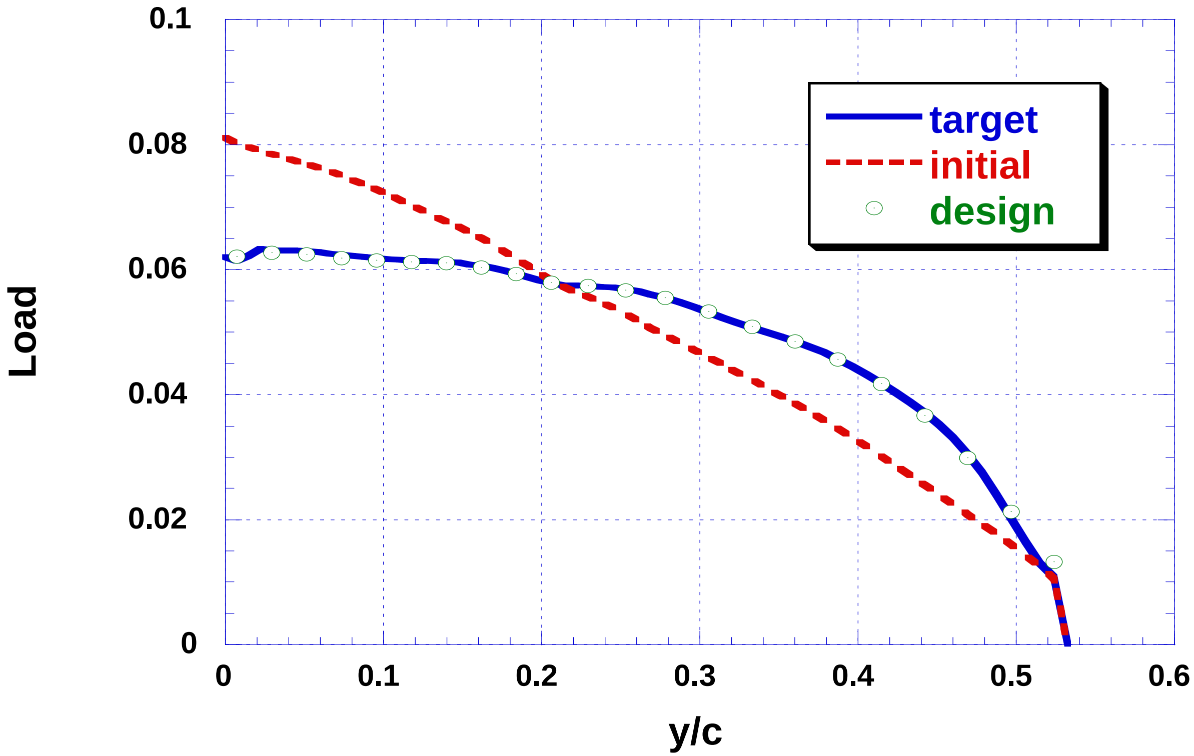

Figure 3-6. Comparison of integrated spanwise load distributions among the target, initial and designed wings

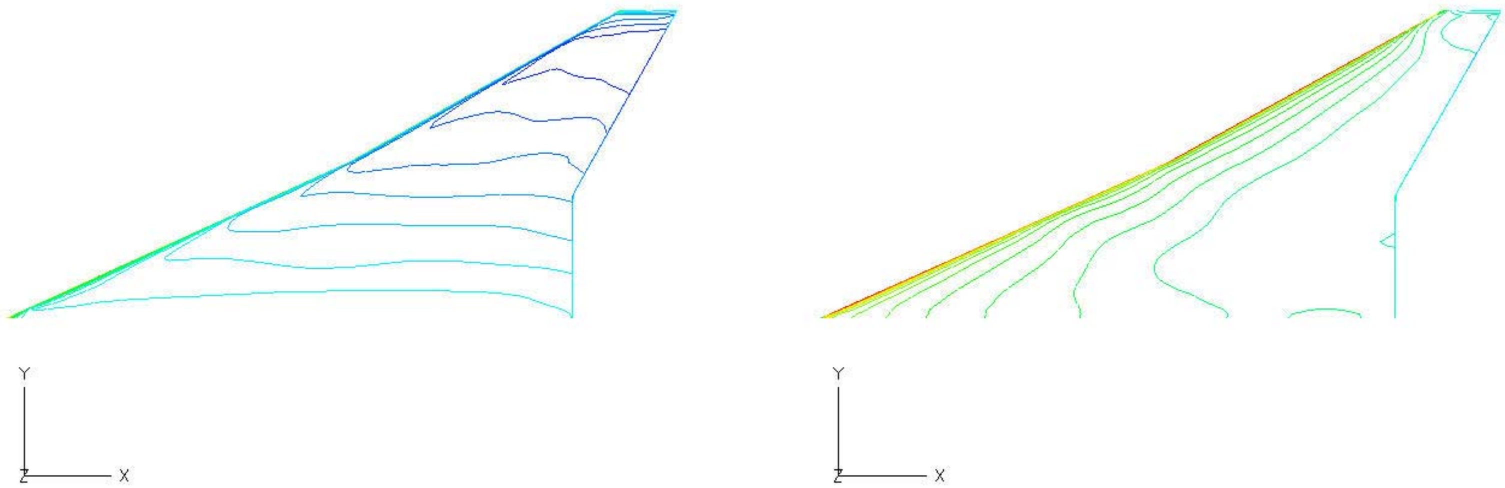

Upper Surface **Lower Surface**

Figure 3-7. Pressure contours of the designed wing

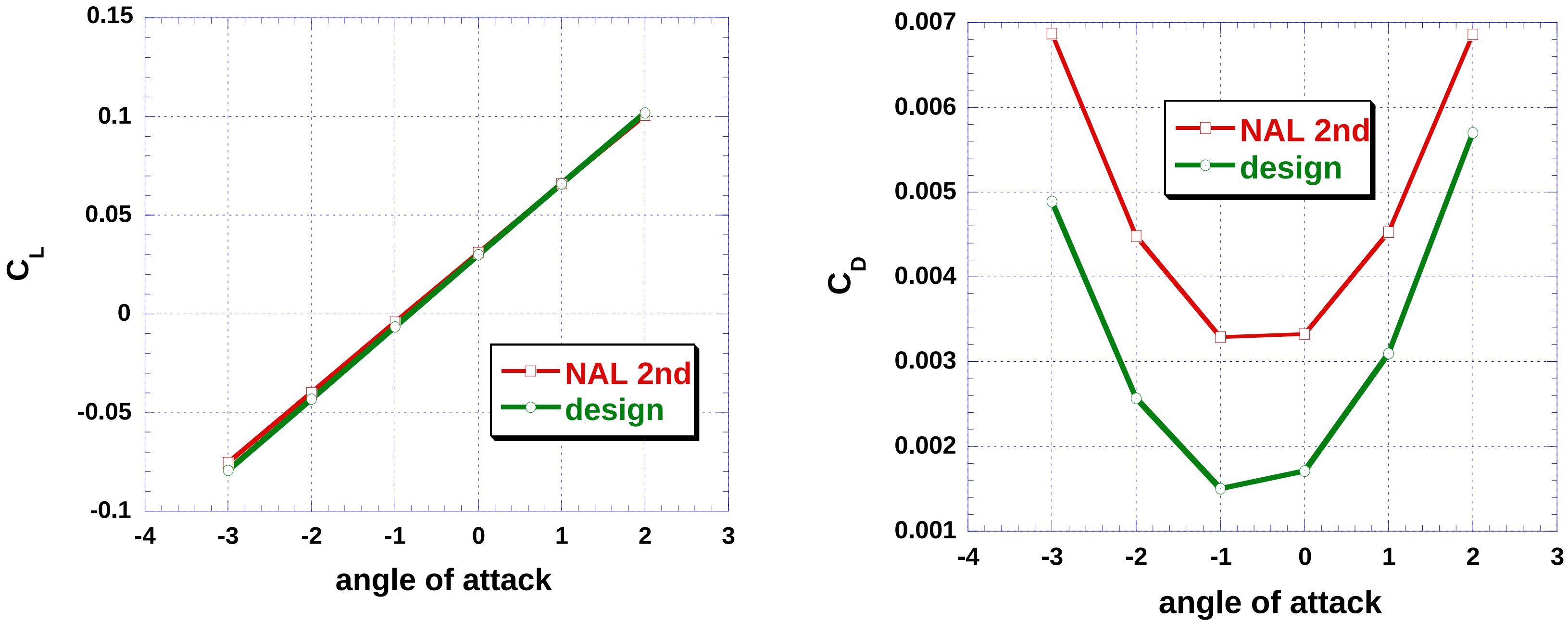

Figure 3-8. Comparison of performance coefficients between NAL’s 2nd and designed wings

	NAL's 2nd wing	Designed wing
C_L	0.10062	0.10198
C_D	0.00686	0.00570
L/D	14.66764	17.8912

Table 3-1. Performance comparison between NAL's 2nd configuration and the designed wing

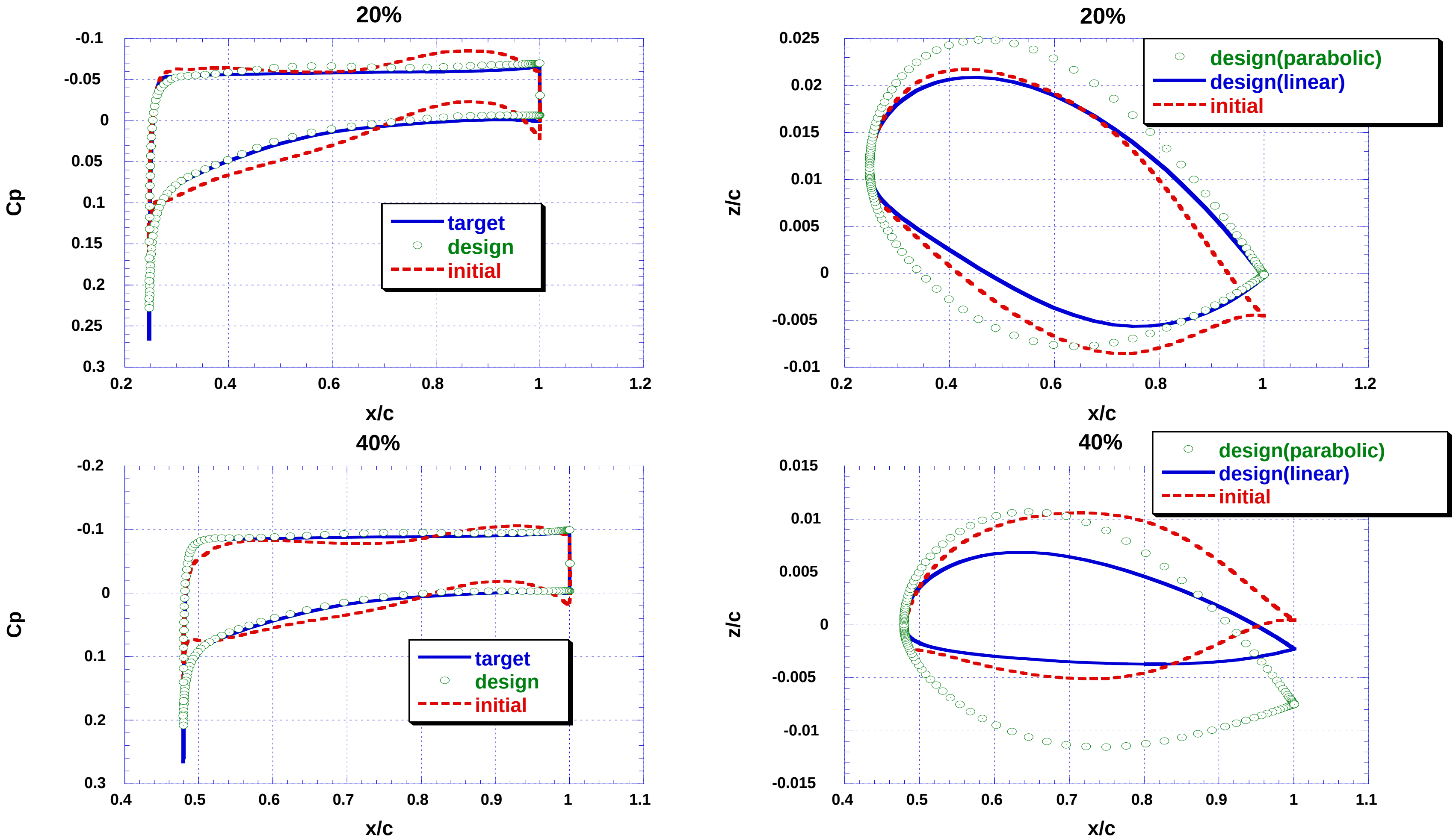

Figure 3-9. Comparison of pressure distributions and corresponding geometries among the target, initial and designed wings (1)

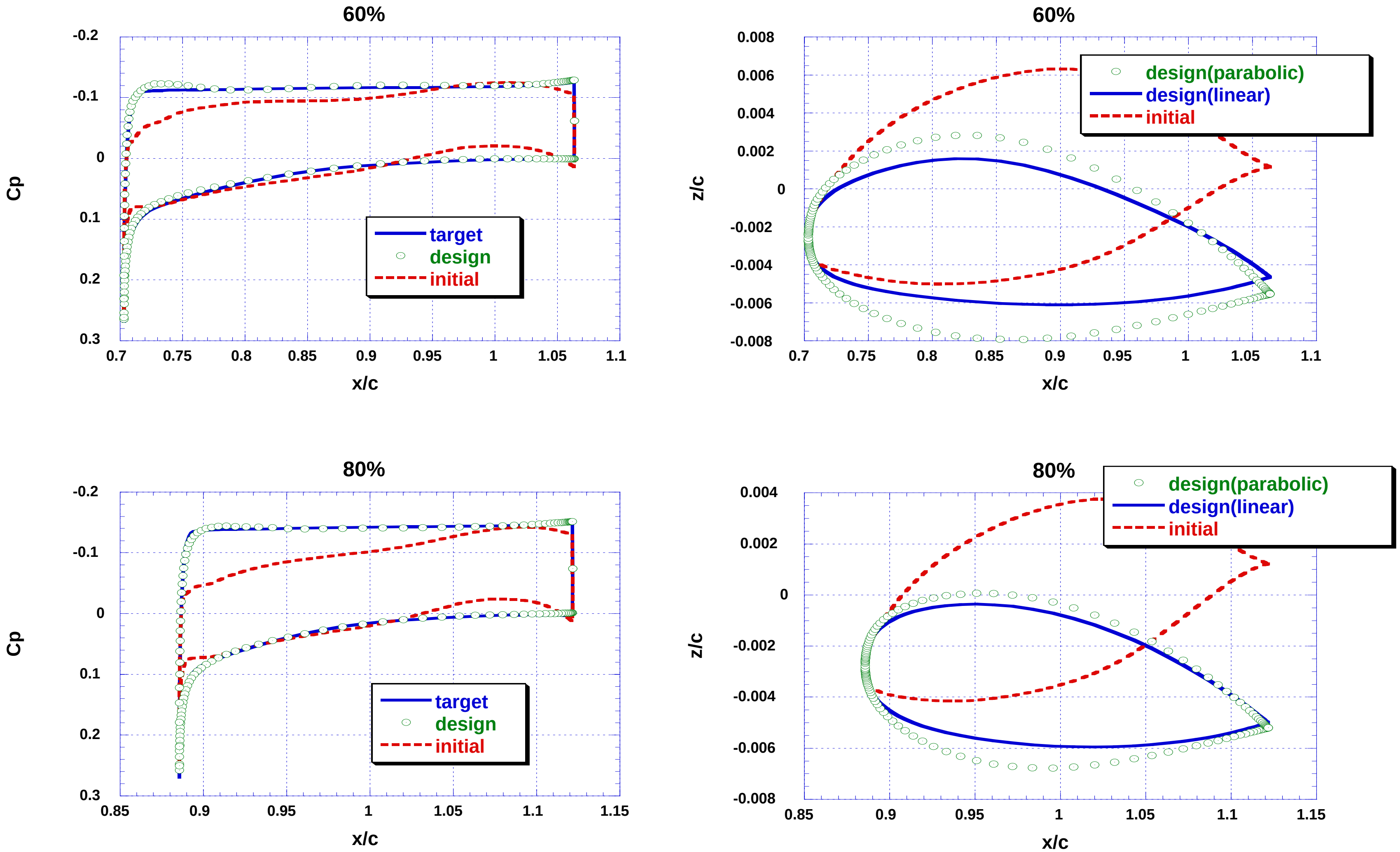

Figure 3-9. Comparison of pressure distributions and corresponding geometries among the target, initial and designed wings (2)

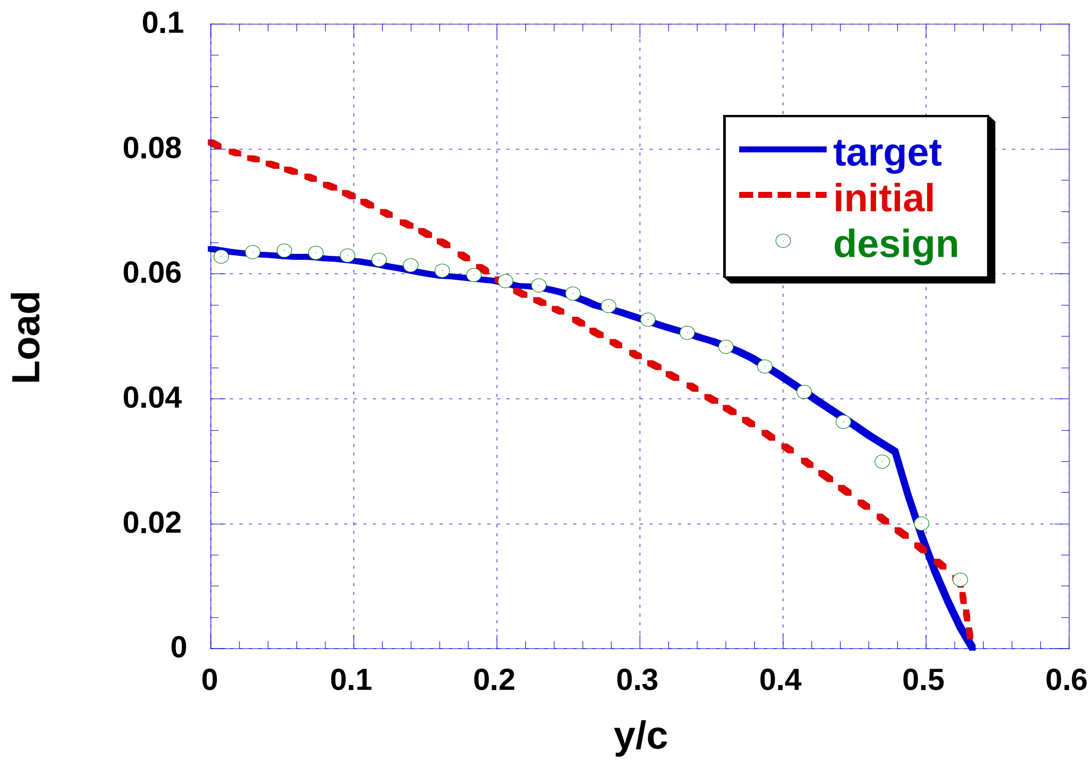

Figure 3-10. Comparison of integrated spanwise load distributions among the target, initial and designed wings

	NAL's 2^{nd} wing	Designed wing
C_L	0.10062	0.10205
C_D	0.00686	0.00705
L/D	14.66764	14.84700

Table 3-2. Performance comparison between NAL's 2nd configuration and the designed wing

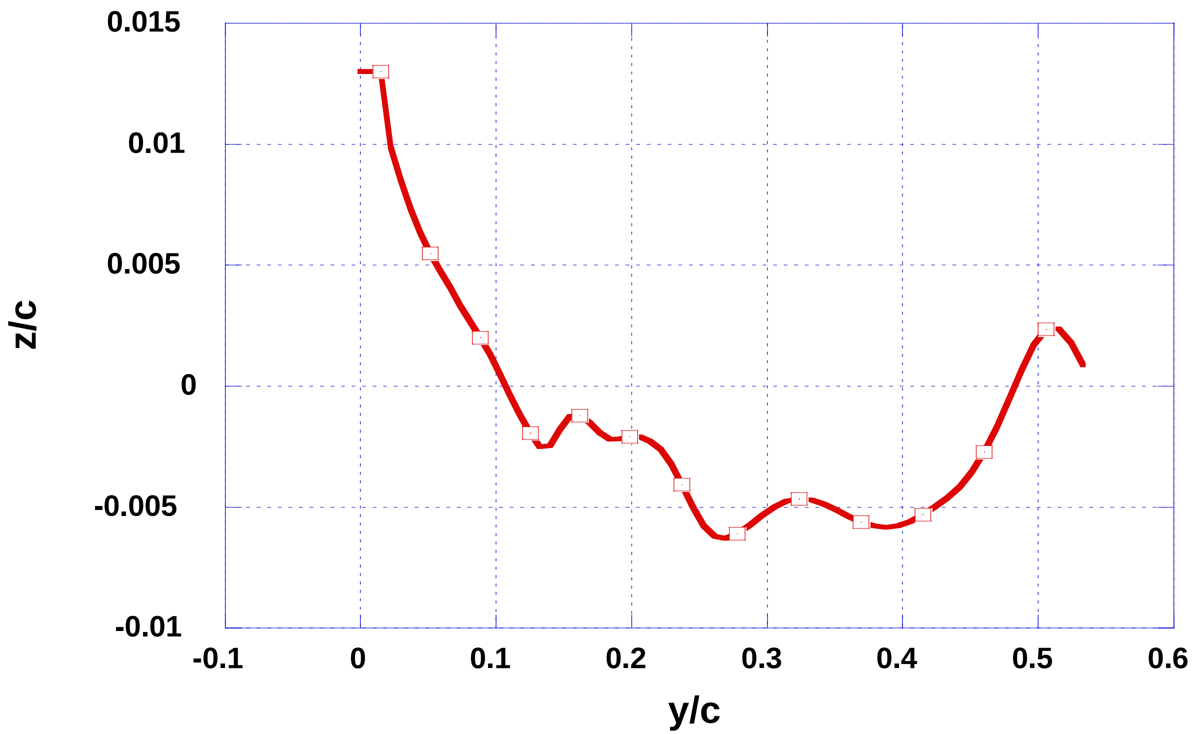

Figure 3-11. Trailing-edge line of the designed wing by the inverse method

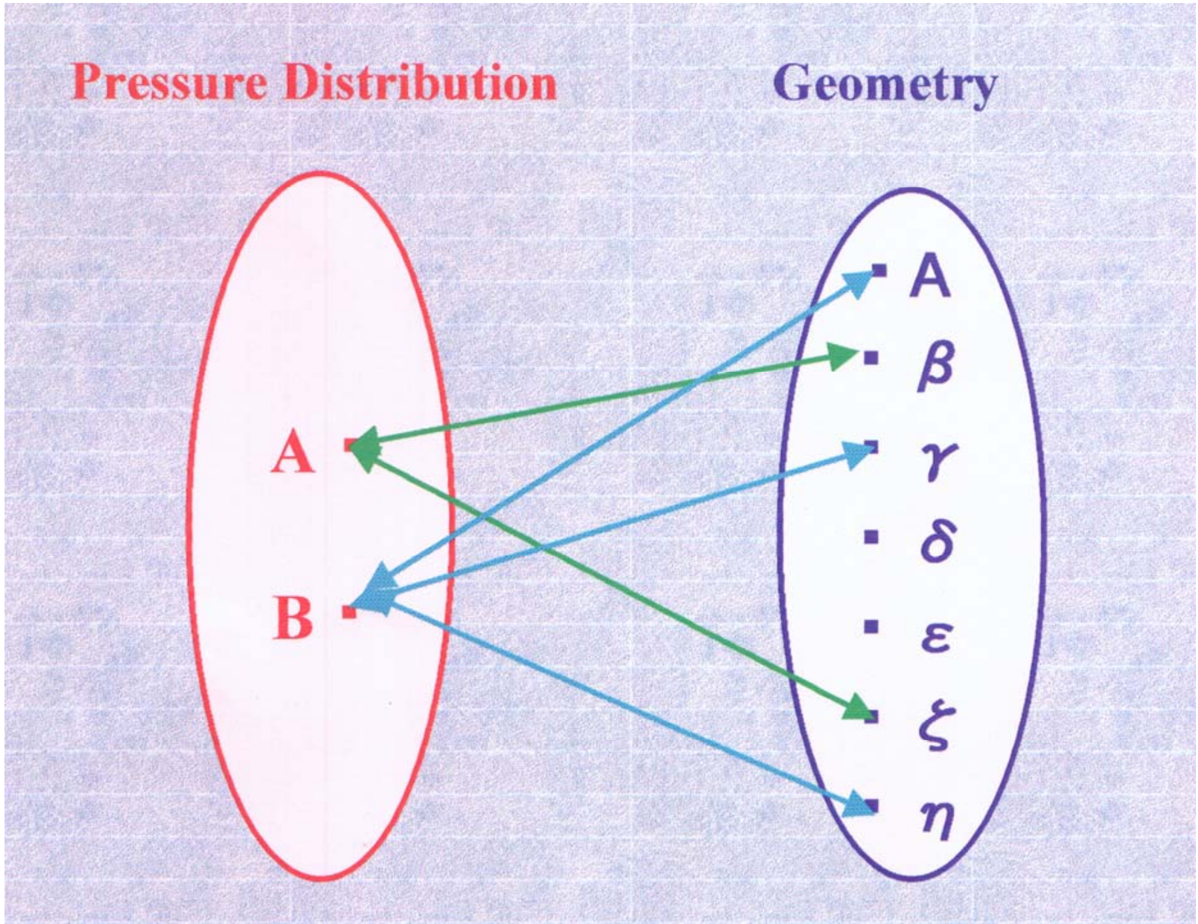

Figure 3-12. Non-uniqueness of the three-dimensional inverse problem

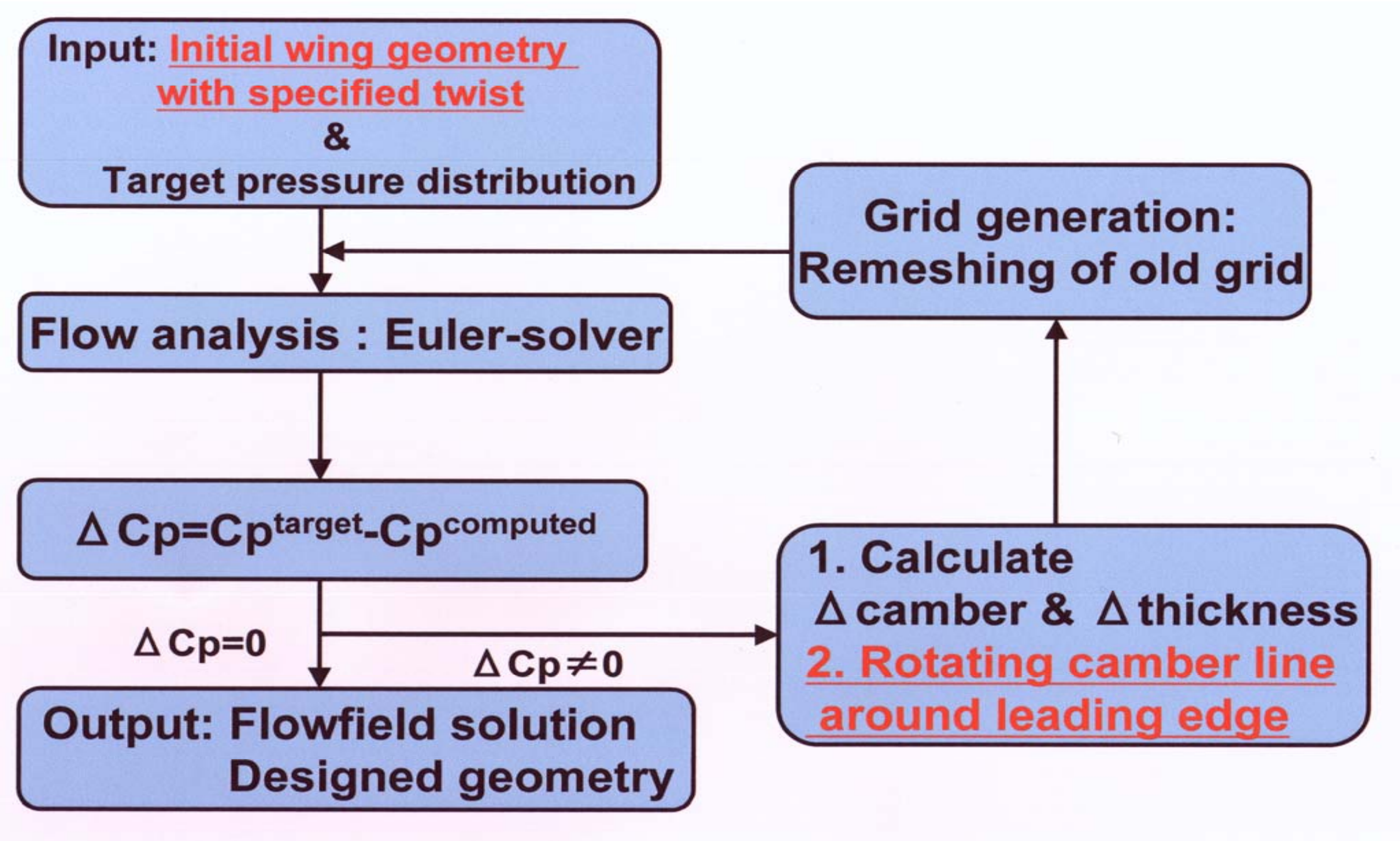

Figure 3-13. Procedure of the proposed twist-specified inverse design

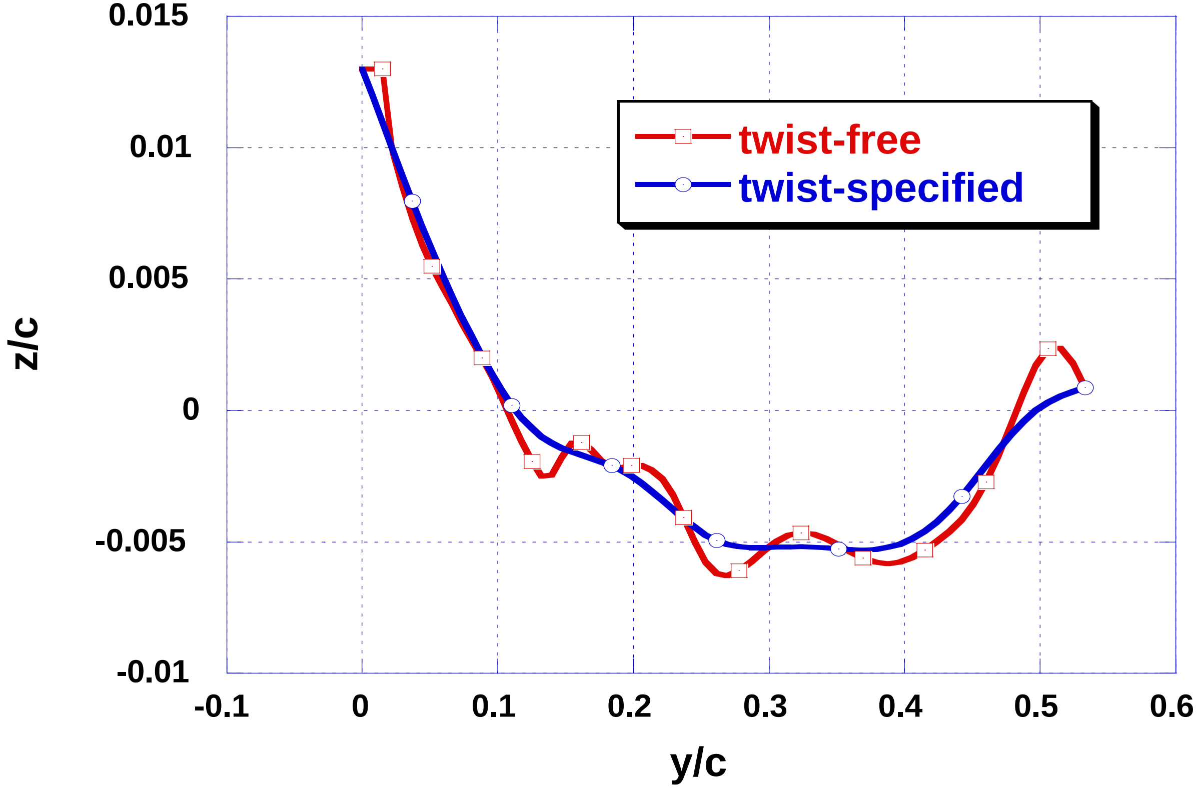

Figure 3-14. Comparison of trailing-edge lines between twist-free and twist-specified design methods

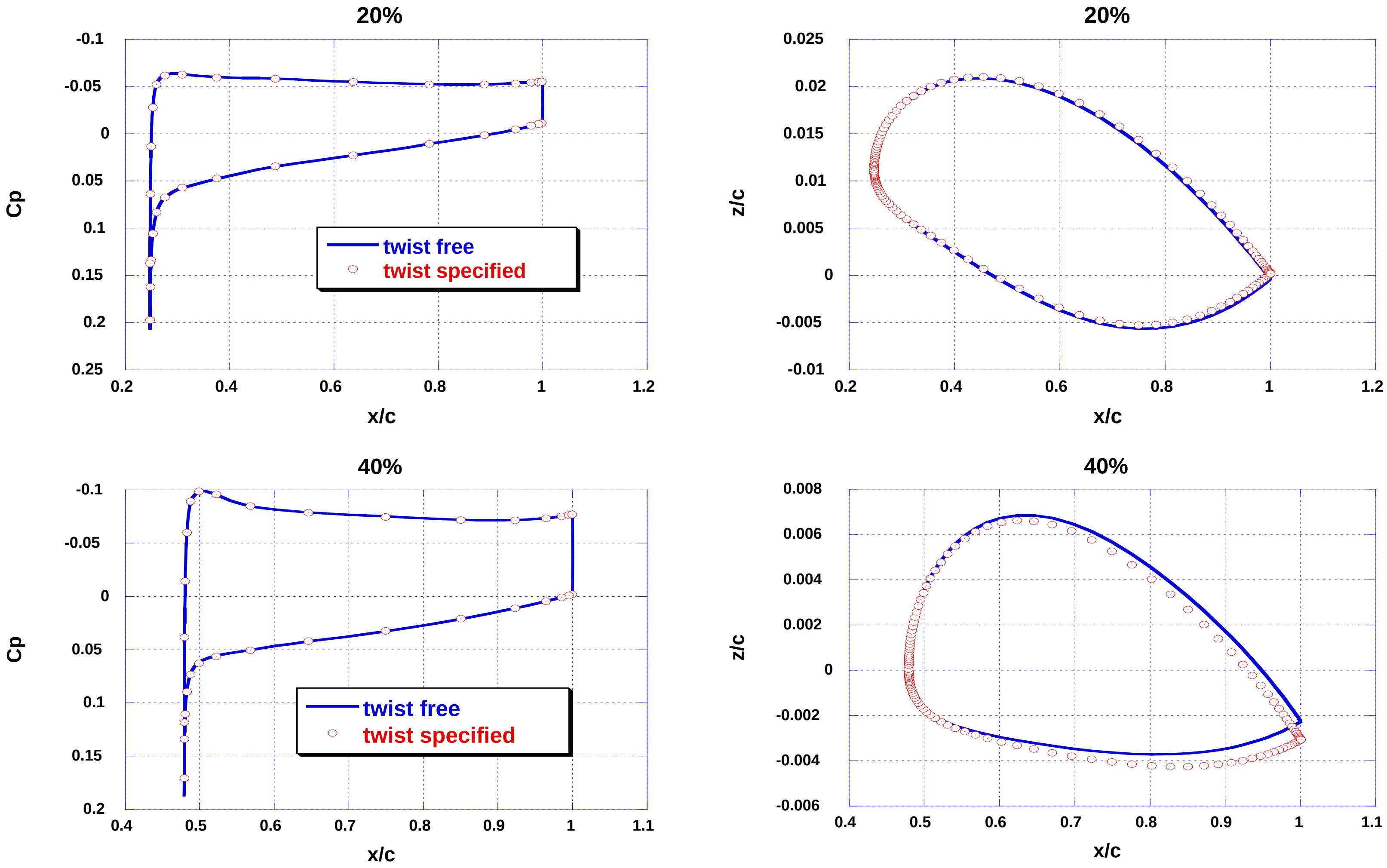

Figure 3-15. Comparison of pressure distributions and corresponding geometries between twist-free and twist-specified inverse design methods (1)

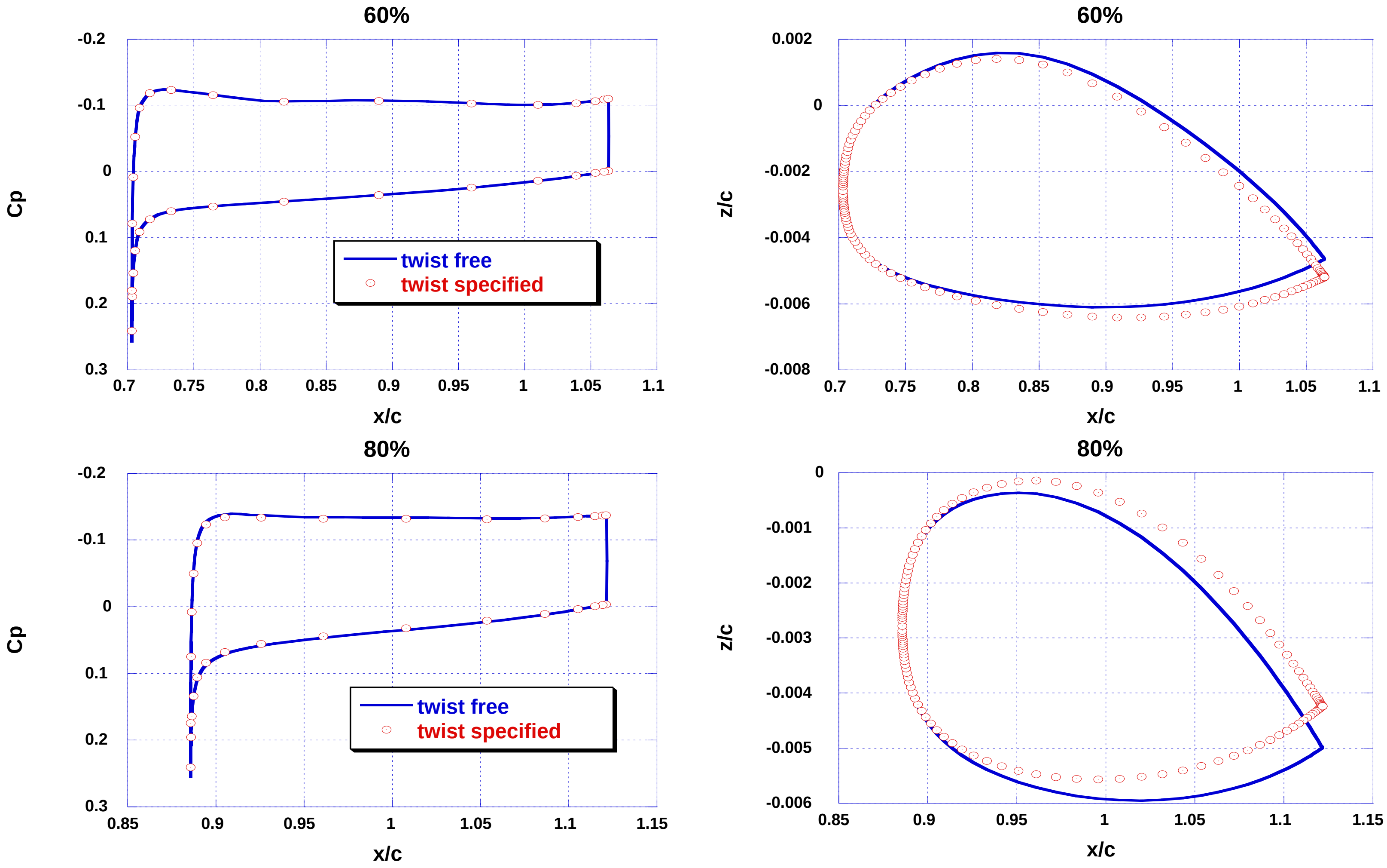

Figure 3-15. Comparison of pressure distributions and corresponding geometries between twist-free and twist-specified inverse design methods (2)

CHAPTER Ⅳ

APPLICATION OF INVERSE DESIGN METHOD TO COMPLICATED CONFIGURATIONS

Ⅳ-1. Introduction

This chapter discusses an extension of the proposed inverse design method to complicated aircraft configurations, such as wing-fuselage and wing-nacelle configurations. In the traditional design methods for wings at supersonic speed [1, 2], not only a nonlinear effect of wing thickness distribution but also interference with components of aircraft, such as fuselage and nacelles, degenerate the warp performance optimized by the linear theory. To design a SST configuration more accurately, a wing design method that also accounts for the interference with other aircraft components is indispensable. The present inverse design method based on the iterative "residual-correction" concept can be extended to design a wing under the consideration of interference with other components.

In this chapter, the present inverse design method will be applied to the wing-fuselage and the wing-nacelle configurations. The present inverse method has been implemented into NAL SST design system. The design result of the wing-fuselage configuration [3] was presented here by courtesy of the NAL SST design team. They utilized the inverse design method to find a wing for a natural laminar flow (NFL) in their design process. The outline of NAL's scaled supersonic experimental aircraft design process [4] is reviewed in Appendix.

Another indispensable tool required for dealing with the complicated configurations is an efficient grid generator. For complicated configurations, the grid generation is very time consuming. In order to resolve this problem, the unstructured grid approach is utilized to the inverse design of a wing-nacelle configuration, since the unstructured grid approach has a great versatility and geometrical flexibility.

Ⅳ-2. Inverse Design of Wing-Fuselage Configuration

In this section, the inverse design of a wing-fuselage configuration is presented by courtesy of NAL. The outline of the NAL SST design process is reviewed in Appendix. The initial wing was taken from the NAL's 2nd baseline configuration that had a NACA66003 thickness distribution. The specified target pressure distribution has a rapid pressure drop near the leading edge followed by a flat pressure distribution toward the trailing edge to realize NLF. The design condition is a Mach number of 2.0 and an angle of attack of 2.0°. The design considers the geometry correction on the wing surface only, while the flow analysis is performed about the wing-fuselage configuration to obtain the pressure distribution on the wing surface under the influence of the fuselage. The flow analysis was executed by using NAL's Navier-Stokes code [5]. In NAL's code, the AUSMDV scheme [6] is applied for the discretization of the convective terms. For the time integration, the explicit Euler method is adopted. The Baldwin-Lomax turbulence model is used.

The main feature of NAL's code is the utilization of multiple blocks [7]. Figure 4-1 shows the body surface and the outer grid surfaces used in this calculation. Computational space is divided into fourteen blocks; six blocks on the body surface, four blocks on the wing surfaces and four blocks in the wing wake domain.

In this inverse design, two geometry constraints [8] are implemented. First, the twisting axis of the wing is requested to go through 70% chord of every spanwise section. To satisfy this constraint, the designed wing sections are translated in the z direction so as to 70% chord of every section lie on the straight line. The other constraint is that $0.03 \le t/c_{\max} \le 0.037$. The geometry correction is performed for the designed wing at each iteration steps so as to satisfy this thickness constraints.

The comparisons of pressure distributions and corresponding geometries among the target, initial and designed wings after 10 inverse cycles are plotted in Fig. 4-2. The pressure distribution of the designed wing is close to that of the target.

The integrated spanwise loads are plotted in Fig. 4-3. The loads of the designed wing also coincide with those of the target that is elliptic for the minimum induced drag. These results confirmed the validity of applying the present inverse design method that is based on the iterative "residual-correction" concept to a wing geometry under the influence of the fuselage.

Ⅳ-3. Flow Filed Analysis of Wing-Nacelle Configuration

One of the difficulties in the inverse design of a complicated configuration is generation of a computational grid around geometry. The grid generation around a complex configuration is a very time-consuming procedure. According to NAL SST design team, it took three days to generate a multiblock computational grid used in the wing-fuselage design. To construct an efficient design system, a more rapid and robust grid generation tool is required.

In order to resolve this problem, an unstructured grid approach [9] is adopted to a wing-nacelle configuration design here. The surface grid of a three-dimensional configuration is generated by the direct surface meshing method [10]. The method applied the advancing front approach directly to the geometry surface in the physical space. Since it does not rely on a mapping, the mesh size can be automatically controlled by adapting to the local surface curvature. Without mapping, surface definition for meshing can be more flexible. Figure 4-4 shows the surface grid around the wing-nacelle configuration. The nacelles have a circular cross section and a kink at 50% location.

There is an additional problem on accurately representing the true geometry, especially, at the leading edge near the outer wing where its local curvature is very large. In this study, the structured grid is adopted for the surface grid near the leading edge. By drawing a diagonal in each rectangular structured grid, triangles for the unstructured grid can be generated. Figure 4-5 shows the airfoils sections at 80% spanwise sections represented by the original unstructured grid and the present hybrid grid. As shown in figure, the present grid represents the real geometry more accurately.

The tetrahedral volume grid is generated by applying the Delaunay approach [11]. Figure 4-6 shows the volume grid around the wing-nacelle configuration. Even in a very narrow region inside of the nacelle, the tetrahedral mesh is automatically generated.

Overall workload required for the generation of the grid is less than one day.

The flow analysis is performed by an Euler code. The governing equations are given in the non-dimensional integral form as follows:

$$\frac{\partial}{\partial t}\int_{\Omega} Q\, dV + \int_{\partial\Omega} F(Q)\cdot n\, dS = 0 \qquad (4\text{-}1)$$

where $Q = \left[\rho, \rho u, \rho v, \rho \mathrm{w}, e\right]^T$ is the vector of the conservative variables; ρ is the density; u, v, w are the velocity components in the *x, y, z* directions, respectively; and *e* is the total energy. The vector $F(Q)$ is the inviscid flux vector; and n is the outward normal to $\partial\Omega$, which is the boundary of the control volume Ω. This system is completed by the perfect gas equation of state. The equations are solved by a finite-volume cell-vertex scheme and the LU-SGS method [12, 13] for the spatial discretization and time integration, respectively.

To validate the unstructured grid and the Euler solver used here, the flow field around the isolated wing designed in Chapter 3 is computed again. The pressure distributions obtained from the structured and unstructured grid approaches are plotted in Fig. 4-7. They appear identical and the resolution of the unstructured grid approach is found comparable to that of the structured grid approach.

Ⅳ-4. Inverse Design of Wing-Nacelle Configuration

With this unstructured approach, the inverse design of the wing-nacelle configuration was performed. To verify the inverse method, initial geometry was created by attaching nacelles described in the previous section to the initial wing described in

Chapter 3. The target pressure distribution was generated from the wing designed in Chapter 3 by attaching the same nacelles. The design condition is a Mach number of 2.0 and an angle of attack of 2.0°.

In this case, due to strong shock waves generated from the front part of the nacelles on the lower surface of the wing, the flow field in this region becomes very complicated. Thus, in this region, the integral Eqs. (2-37) and (2-48) are replaced by the lower approximation Eqs. (2-53) and (2-54) as done for near the root and tip of the wing. Figure 4-8 illustrates the areas to be dealt with these equations.

The inverse design results after 5 iteration steps are shown in Fig. 4-9. The chordwise pressure distributions and the corresponding airfoil geometries at the 20, 40, 60 and 80% spanwise sections of the target, initial and designed wings are plotted. The pressure distribution of the designed configuration converges to that of the target very well. Minor discrepancy in the geometries may attribute to the non-uniqueness of the three-dimensional inverse problem. TSID was not executed here yet. With a proper treatment of shock waves generated from the nacelles, the present inverse method is confirmed to be applicable to the wing-nacelle configuration design.

Ⅳ-5. Summary

The present inverse design method was applied to complicated aircraft configurations. In this chapter, design results of wing-fuselage and wing-nacelle configurations were presented. In the design performed by the NAL SST design team, the inverse design method was used to find the wing design under the influence of the fuselage. Design results confirmed the validity of applying the present inverse design method to the complicated configurations.

One of the difficulties in applying the inverse design to complicated aircraft configurations is the generation of computational grids. The grid generation around a complex configuration is a very time-consuming procedure. In order to resolve this problem, the unstructured grid approach was considered because of a great versatility and geometrical flexibility. The wing-nacelle configuration design was then performed. The workload required for the grid generation at each inverse design cycle was reduced from three days to less than one day. The inverse design coupled with the unstructured grid approach was confirmed to be practical.

References

[1] H. W. Carlson and W. D. Middleton, "A Numerical Method for Design of Camber Surfaces of Supersonic Wings with Arbitrary Planforms," NASA TN-2341, 1964.

[2] H. W. Carlson and D. S. Miller, "Numerical Method for the Design and Analysis of Wings at Supersonic Speeds," NASA TN D-7713, 1974.

[3] K. Matsushima, T. Iwamiya, S. Jeong and S. Obayashi, "Aerodynamic Wing Design for NAL's SST Using Iterative Inverse Approach," Proceedings of 1st International CFD Workshop for SST Design, pp. 73-78, Tokyo, Japan, NAL, March 1998.

[4] Y. Shimbo, K. Yoshida, T. Iwamiya, R. Takaki and K. Matsushima, "Aerodynamic Design of Scaled Supersonic Experimental Airplane," Proceedings of 1st International CFD Workshop for SST Design, pp. 62-67, Tokyo, Japan, NAL, March 1998.

[5] R. Takaki, T. Iwamiya and A. Aoki, "CFD Analysis Applied to the Supersonic Research Airplane," Proceedings of 1st International CFD Workshop for SST Design, pp. 68-72, Tokyo, Japan, NAL, March 1998.

[6] Y. Wada and M. S. Liou, "A Flux Splitting Scheme with High-Resolution and Robustness for Discontinuities," AIAA Paper 94-0083, 1994.

[7] S. Takanashi, "Large-Scale Numerical Aerodynamic Simulations for Complete Aircraft Configurations," Proceedings of ICAS 90, Stockholm, 1990.

[8] K. Matsushima, T. Iwamiya, S. Jeong and S. Obayashi, "Inverse Wing Design for the Experimental Airplane of NAL's SST Research," Proceedings of 76th JSME Fall Annual Meeting, Vol. 2, pp. 9-10, October 1998.

[9] V. Venkatakrishnan, “ A Perspective on Unstructured Grid Flow Solvers,” AIAA Paper 95-0667, 1995.

[10] K. Nakahashi and D. Sharov, “Direct Surface Triangulation Using the Advancing Front Method,” AIAA Paper 95-1686, 1995.

[11] D. Sharov and K. Nakahashi, “A Boundary Recovery Algorithm for Delaunay Tetrahedral Meshing,” 5th International Conference on Numerical Grid Generation in Computational Field Simulation, pp. 229-238, 1996.

[12] Obayashi, S. and Guruswamy, G. P., “Convergence Acceleration of a Navier-Stokes Solver for Efficient Static Aeroelastic Computations,” AIAA *Journal*, Vol. 33, No. 6, pp. 1134-1141, June 1995.

[13] D. Sharov and K. Nakahashi, “Reordering of 3-D Hybrid Unstructured Grid for Vectorized LU-SGS Navier-Stokes Computations,” AIAA Paper 97-2102, 1997.

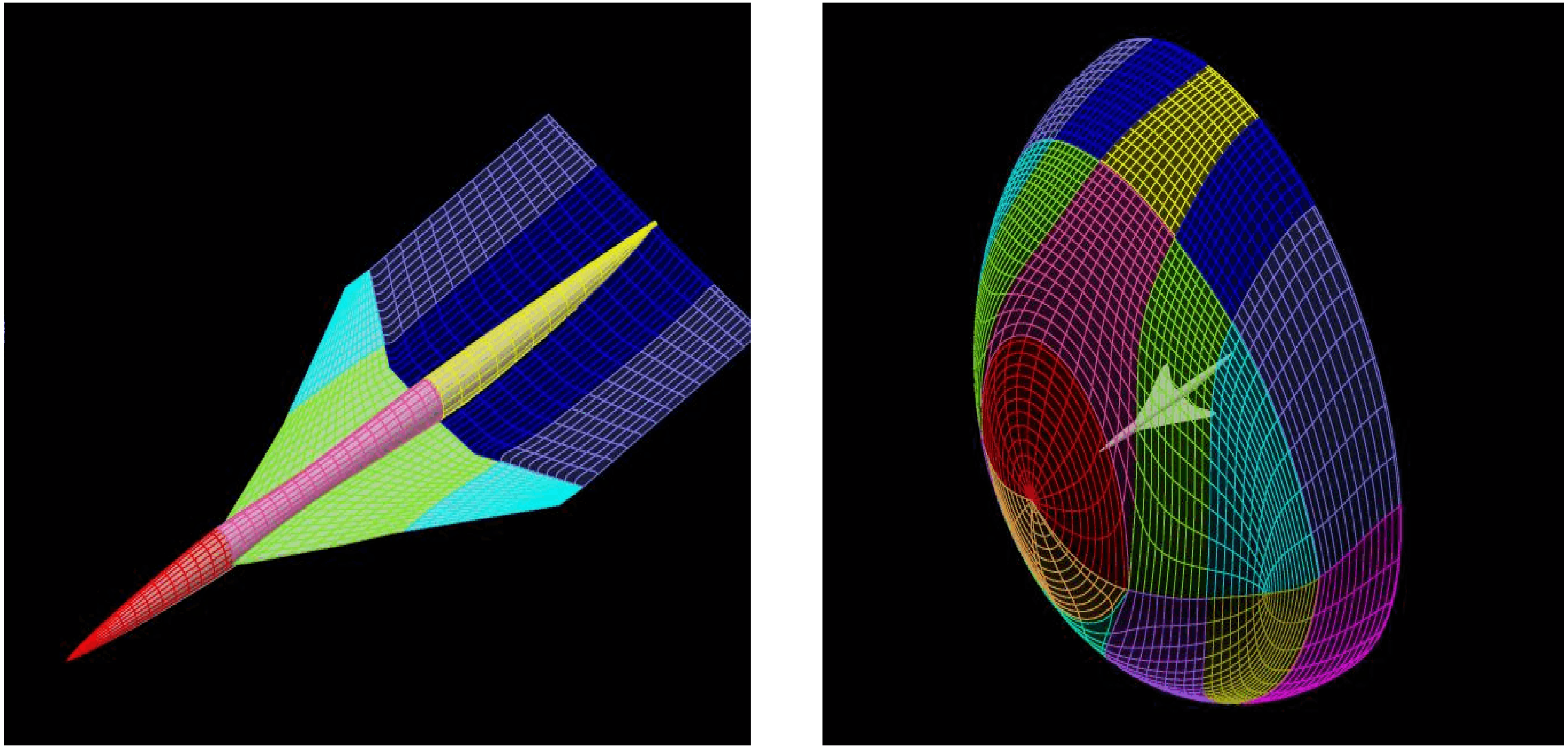

Figure 4-1. Computational grid

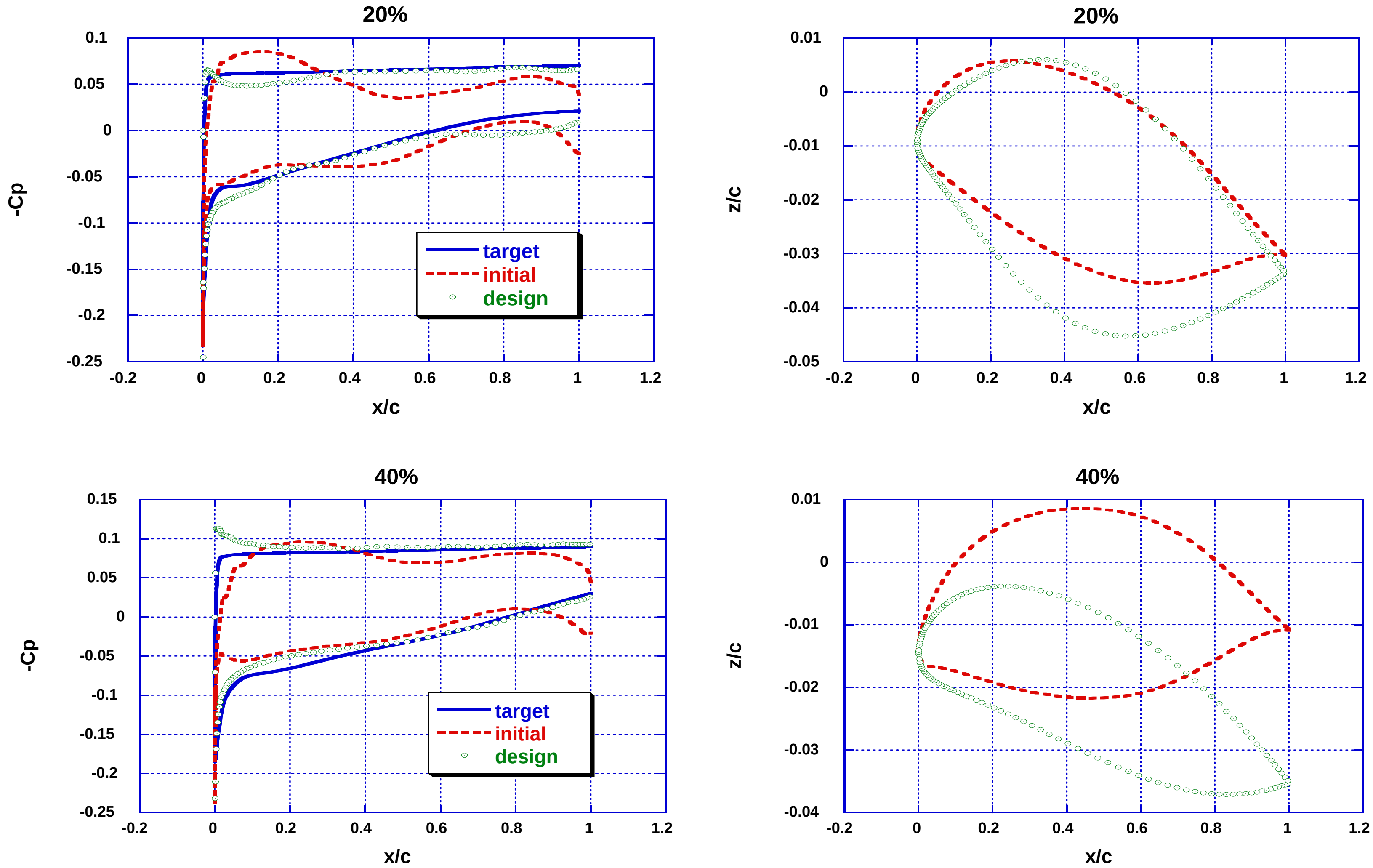

Figure 4-2. Comparison of pressure distributions and corresponding geometries among the target, initial and designed wings (1)

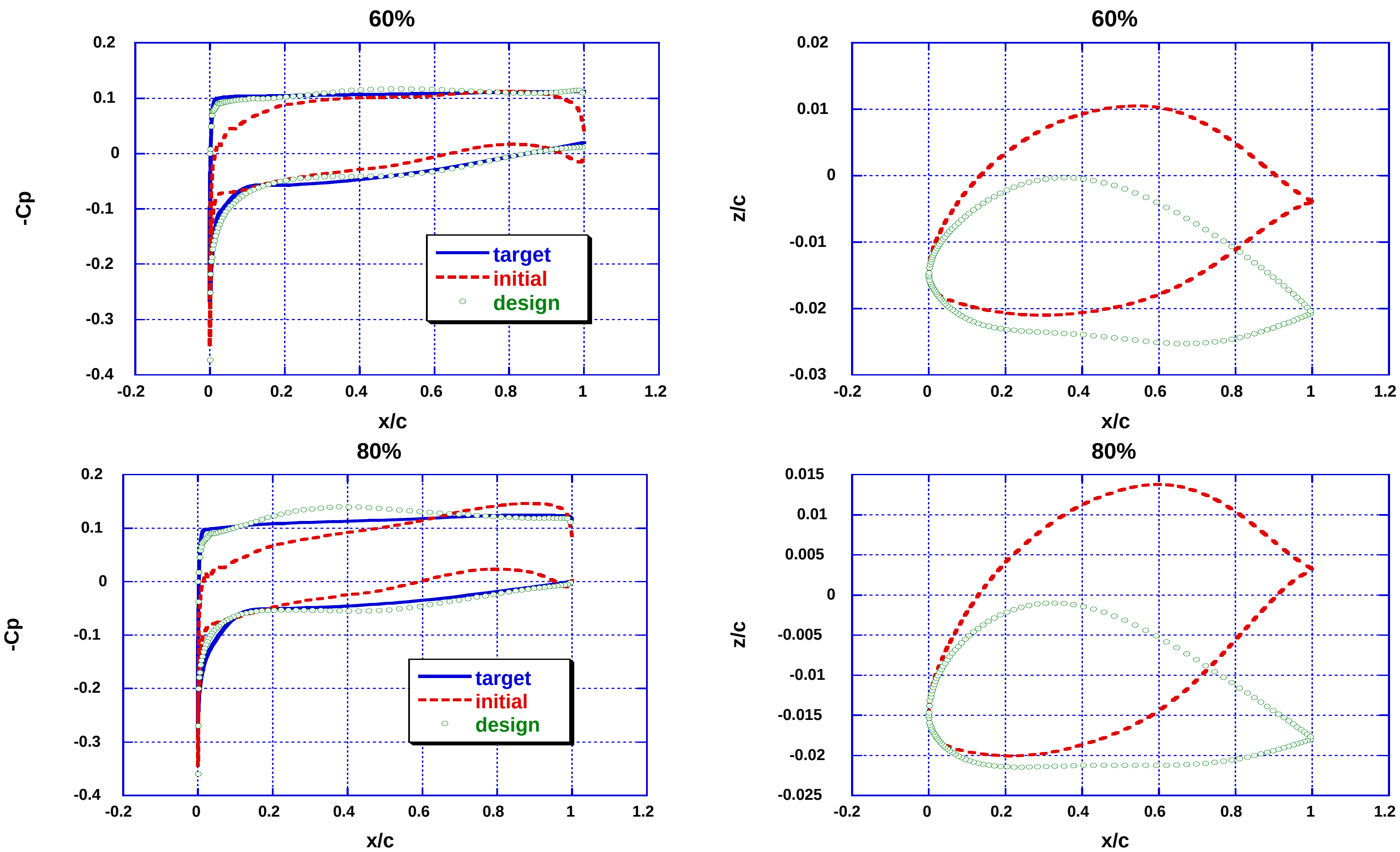

Figure 4-2. Comparison of pressure distributions and corresponding geometries among the target, initial, designed wings (2)

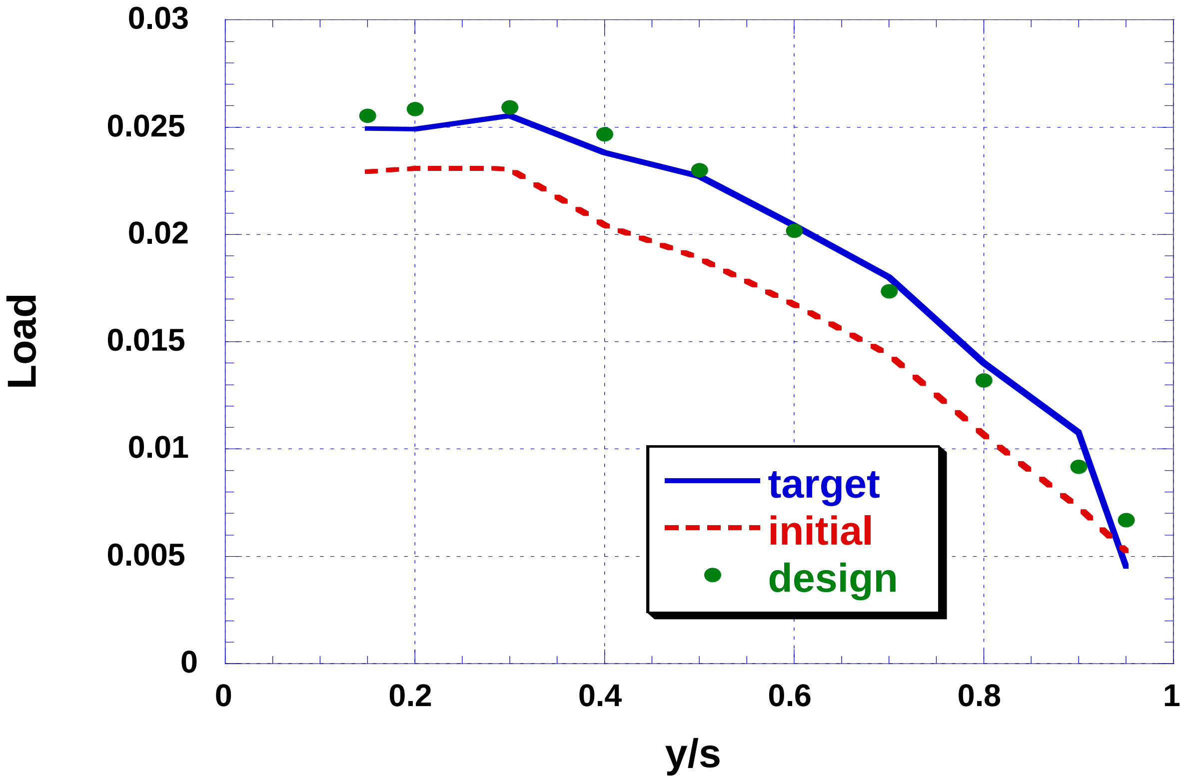

Figure 4-3. Comparison of integrated spanwise load distributions among the target, initial and designed wings

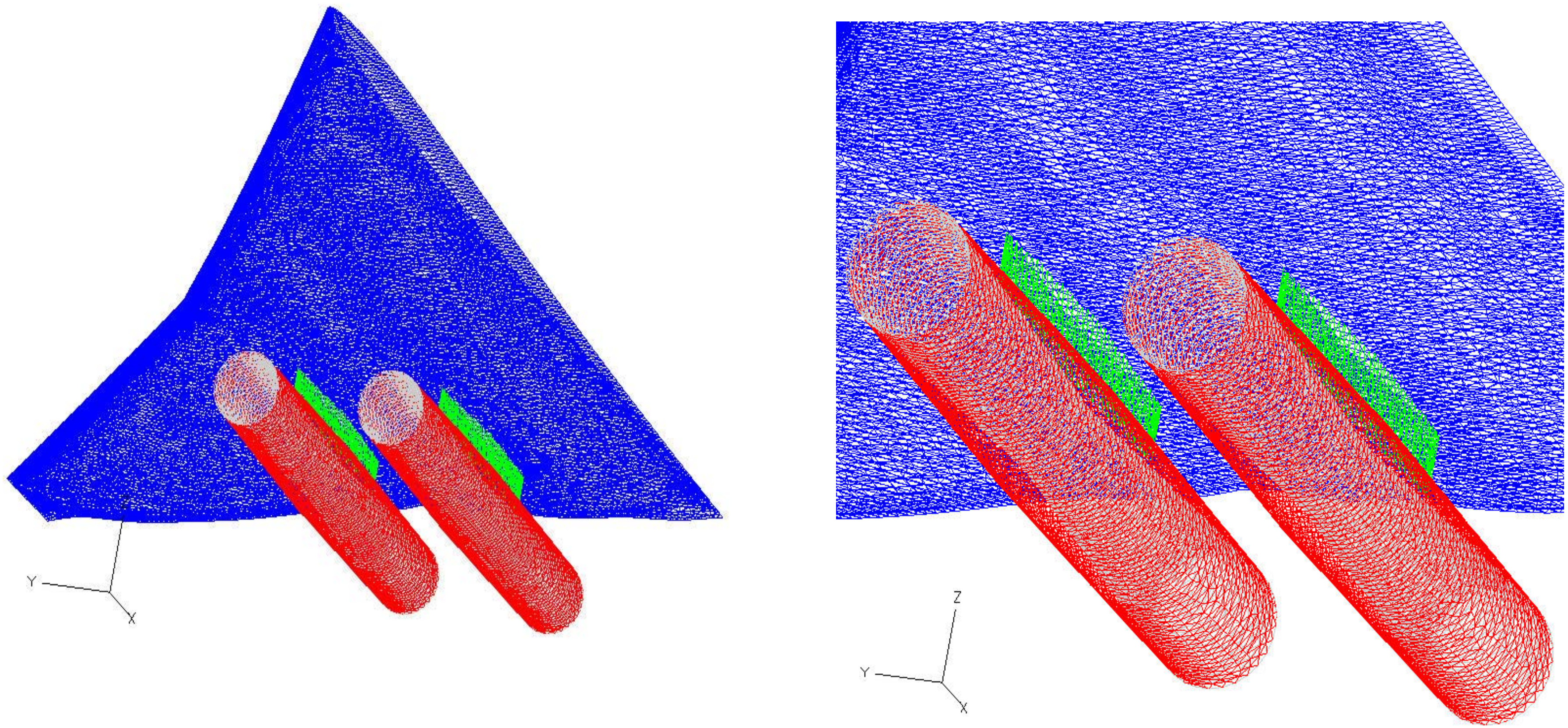

Figure 4-4. Surface Grid

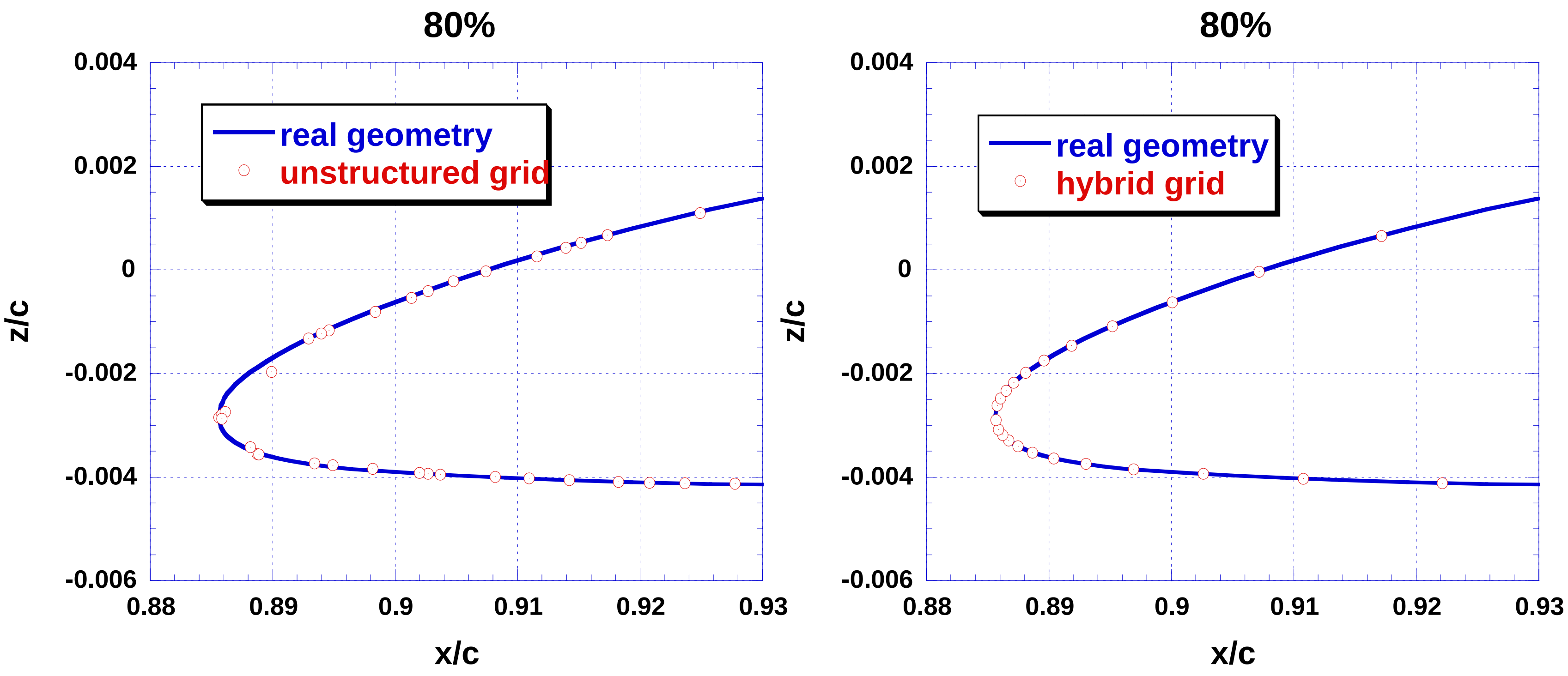

Figure 4-5. Comparison of the ability to represent the real geometry

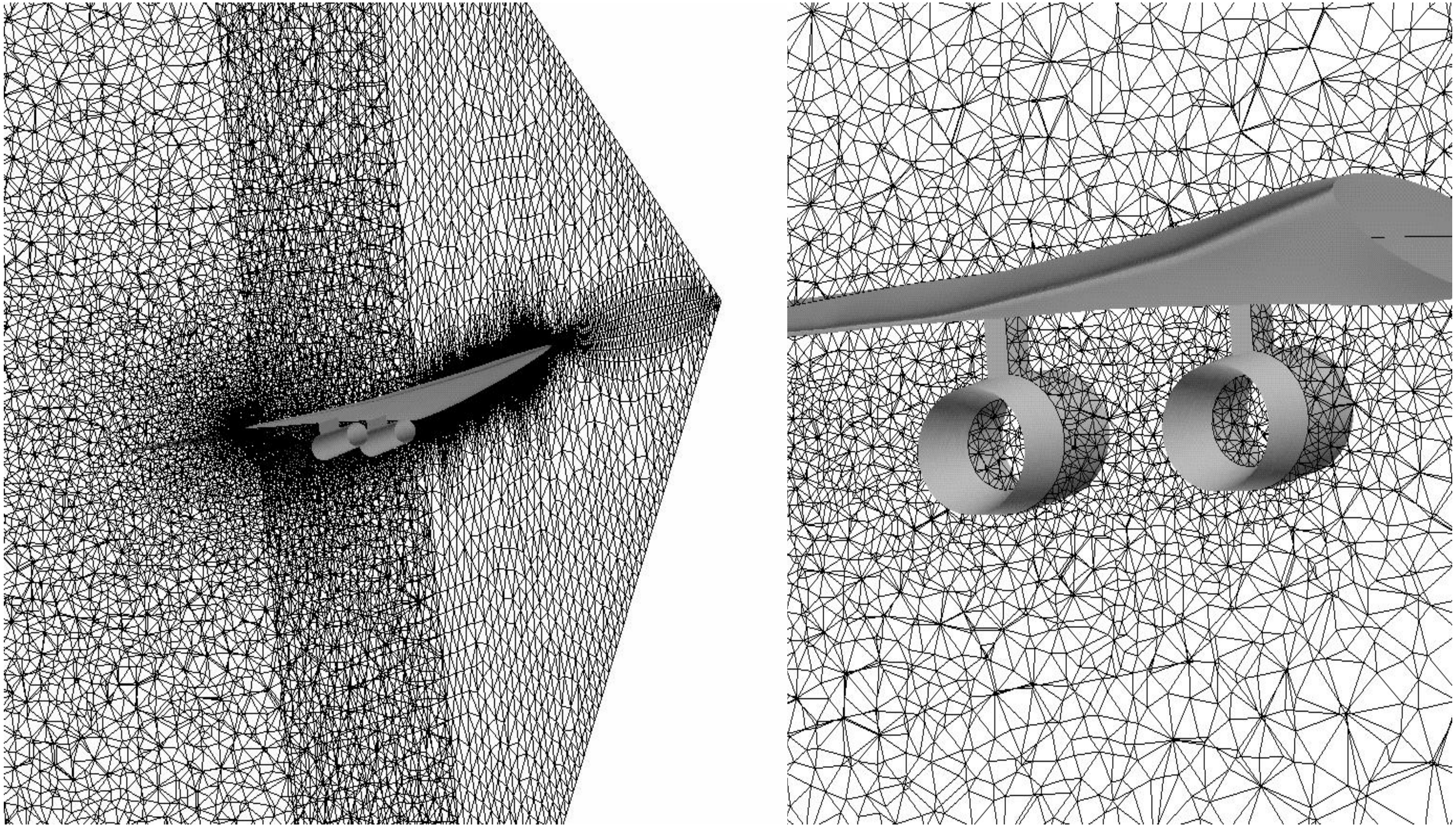

Figure 4-6. Volume grid around the wing-nacelle configuration

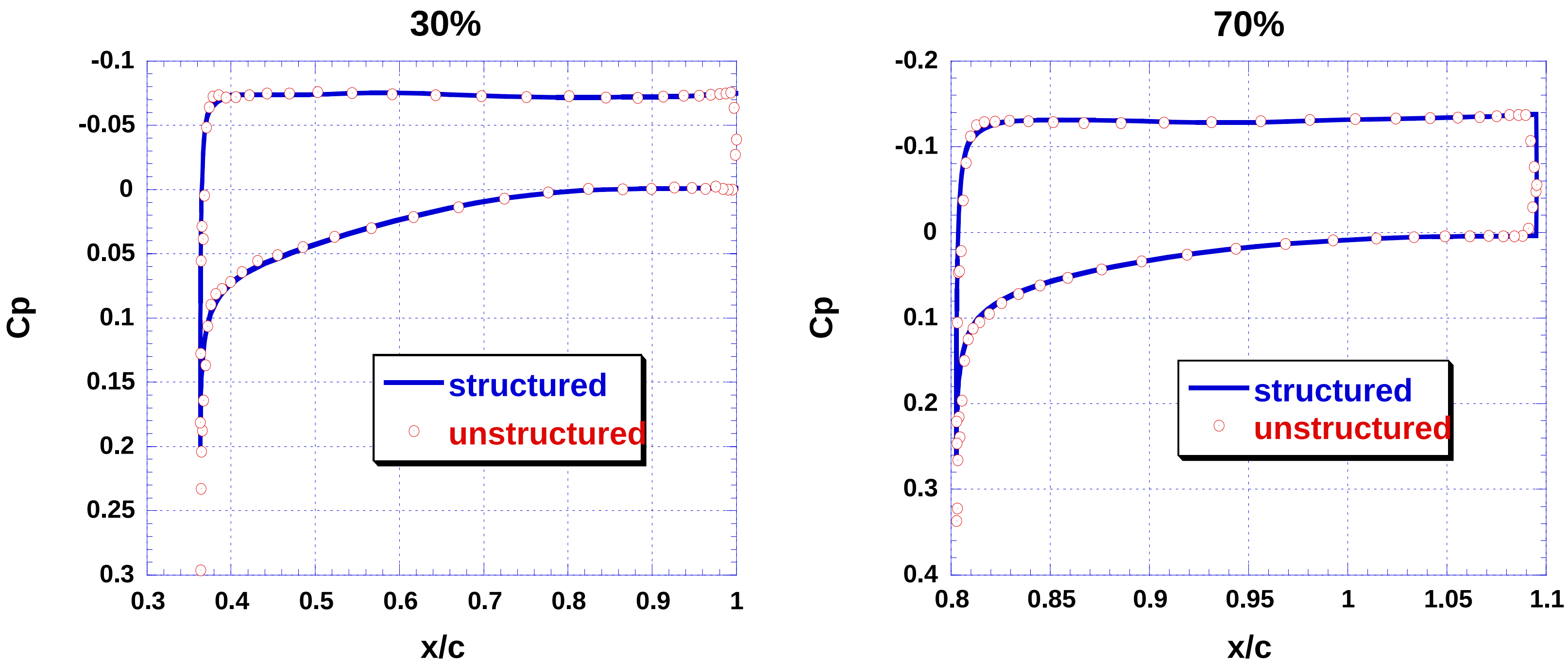

Figure 4-7. Comparison of pressure distributions between structured and unstructured grid approaches

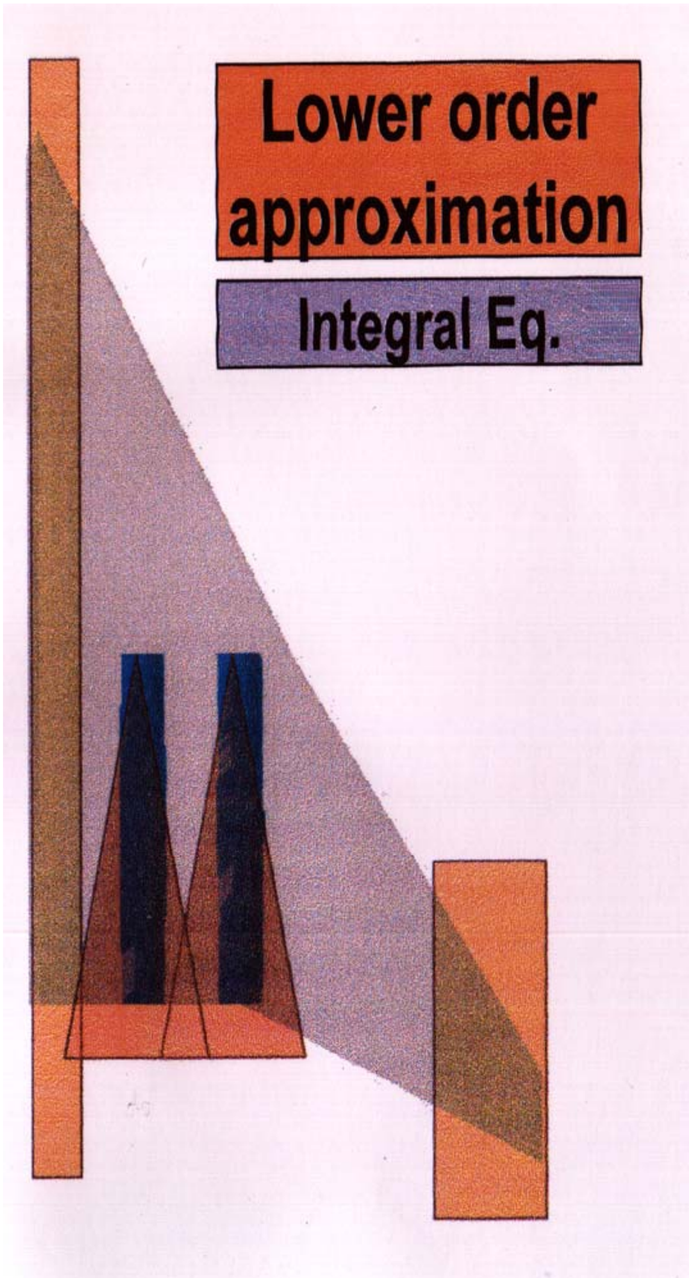

Figure 4-8. The area to be dealt with the integral equations and the lower order approximations.

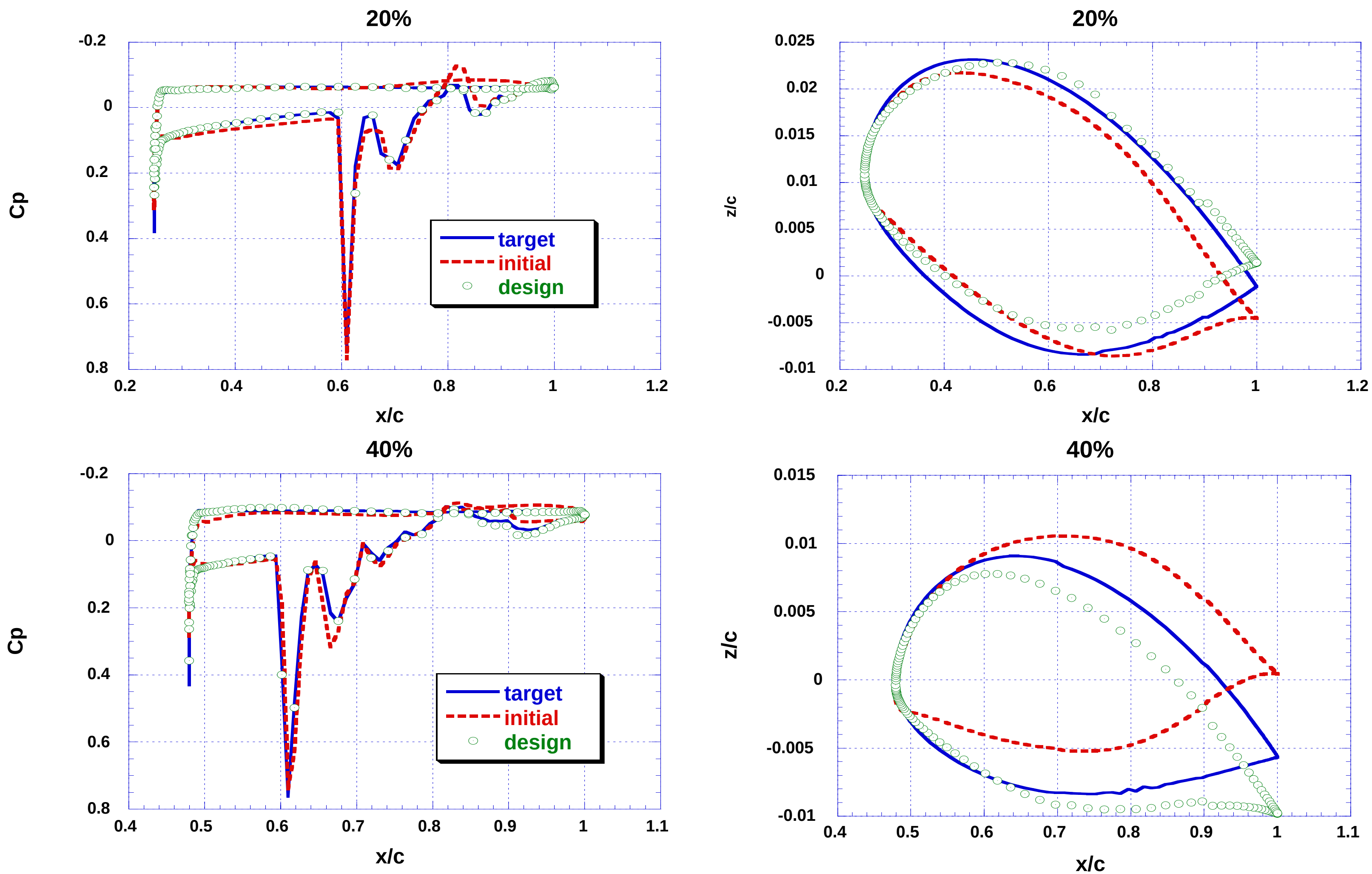

Figure 4-9. Comparison of pressure distributions and corresponding geometries among the target, initial and designed wings (1)

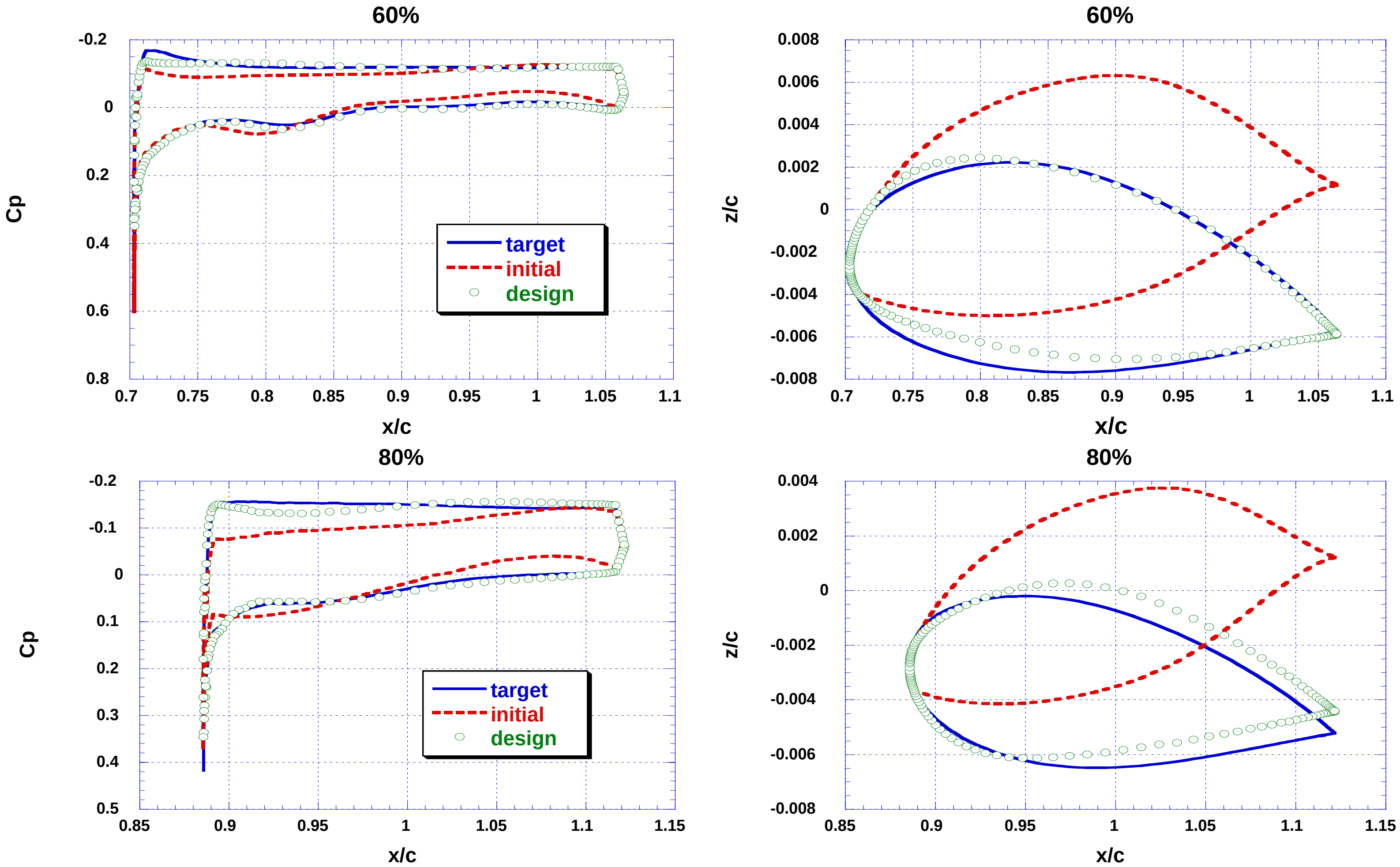

Figure 4-9. Comparison of pressure distributions and corresponding geometries among the target, initial and designed wings (2)

CHAPTER Ⅴ

CONCLUSION

For the successful design of next generation SST, an efficient and robust aerodynamic wing design method was developed in this study. The present method was extended from Takanashi's transonic inverse design method and successfully applied to the supersonic wing design problems.

In Chapter 2, the mathematical formulation for the supersonic inverse problem was constructed. The geometry correction for the inverse design can be obtained from the surface integrals on the wing. To validate the formulation, the design tests were performed. Although the midspan region was designed successfully by the integrodifferential equations derived here, near the root and tip regions had a problem of convergence to the target pressure distribution. Because the integral equations derived here are based on the linearized potential equation, they become invalid near the root and tip of the wing where the vorticity tends to be generated. In order to eliminate this convergence problem, the integral equations were revised by using the supersonic linearized pressure coefficient equations near the wing root and tip. The results of the design tests showed the improved convergence from the root to tip and confirmed the validity of the present approach.

In Chapter 3, the optimization method was investigated for target pressure distribution to be prescribed for the inverse method. Genetic Algorithms (GAs) was selected for the optimization of the target pressure distribution. The present GA adapted the Pareto-ranking approach and the fitness sharing method for the successful application to the multiobjective problems.

Based on the design policies, the optimization problem was defined as a multiobjective problem of the friction and lift-dependent drag minimization. In order to reduce the friction drag, the Natural Laminar Flow (NLF) concept was applied. For the reduction of lift-dependent drag, the elliptic spanwise loading was specified. The shape of chordwise loading pattern for the lift-dependent drag reduction was also studied here. As a result, the linear chordwise loading pattern with the elliptic spanwise load distribution found a better for drag minimization in supersonic wing design.

Twist specification was introduced to the present inverse design method by taking advantage of the non-uniqueness of three-dimensional aerodynamic inverse problems. Due to this technique, the designer is able to select a favorable geometry among the many solution geometries of the three-dimensional aerodynamic inverse problem, in particular, the wing with the specified twist.

In Chapter 4, the proposed inverse design method was extended to the design of the complicated configurations. In this study, supersonic inverse design method was applied to the wing-fuselage and the wing-nacelle configurations.

The wing-fuselage configuration design was performed in NAL's scaled supersonic experimental aircraft project. The flow analysis around the wing-fuselage was performed by using a multiblock approach. The iterative "residual-correction" concept adapted in the present inverse method allowed the wing design under the influence of the fuselage. The inverse method was found useful to design a wing utilizing the NFL concept.

In order to resolve the difficulty of the grid generation around a complicated aircraft configuration, the unstructured grid approach was considered because of its great versatility and geometry flexibility. The wing-nacelle configuration design was then performed with the unstructured grid approach. The time required for the grid generation at each inverse design cycle was reduced drastically. With a proper treatment of shock waves generated from the nacelles, the present inverse method worked also successfully in the wing-nacelle configuration design. The inverse design method coupled with the unstructured approach was confirmed practical for the complicated aircraft configuration design.

Appendix

The present inverse method has been developed under the cooperation with NAL SST Program. This Appendix explains the outline of NAL's scaled experimental aircraft design and how the present method was integrated into the NAL design system. Figures in this Appendix are presented by courtesy of NAL.

NAL’s SST design process comprised two stages. First stage was a baseline configuration design. The baseline configuration was designed as an isolated wing first and then a simple fuselage with circular cross section was attached to this. The second stage was the refinement of the baseline configuration to improve L/D. In this stage, inverse design method was introduced. The following design policy was determined by Yoshida et. al. [A1].

1. Design of a Baseline Configuration

Planform Design

In total of 99 different planforms with an identical area in a specified aspect ratio range from 1.8 to 2.2 were examined first. For every planform, a drag-due-to-lift parameter *K* defined by Eq. (A-1) was evaluated using the supersonic lifting surface theory,

$$C_D = C_{D_o} + K\left(C_L - C_{L_o}\right)^2 \qquad \text{(A-1)}$$

where C_{D_o} denotes the minimum drag coefficients, $C_{L_o} = C_L$ at C_{D_o}. Among these planforms, eight planforms with lower *K* values were selected for the next step.

<u>Warp Design</u>

For each of the eight selected planforms, a warp shape was next optimized by Carlson's method [A2]. The method sought a camber surface that yields an optimal load distribution for minimizing the lift-dependent drag. A planform of an aspect ratio of 2.2 with 66.0 and 61.2 degree sweptback angles at inner and outer leading edge lines, respectively, was finally selected as a planform for the baseline configuration. The baseline wing geometry was produced by adding a thickness distribution of NACA0003 airfoil to the optimized camber surface.

<u>Fuselage Design</u>

A simple body with circular cross sections was combined with the optimized wing. To minimize a wave drag, the supersonic area rule [A3] was applied. This wing-fuselage configuration is the baseline configuration of NAL's SST program.

2. Refinement of the Baseline Configuration

<u>Quasi-Inverse Design</u>

The first strategy of the wing refinement in the second design stage was to recover the optimized warp performance obtained by the linear theory. Figure A-1 shows a comparison of loading contours between the isolated wing and the wing-fuselage configurations. As shown in the figure, the wing-fuselage configuration lost the optimized load pattern due to the interference with the fuselage.

To recover the optimized warp effect here, a quasi-inverse design method was used.

This method calculated the new camber line for the wing-fuselage configuration using a supersonic small disturbance theory [A4].

$$\Delta P = P^{target} - P^{old} \tag{A-2}$$

$$\Delta \frac{dz_c(x)}{dx} = \varepsilon \frac{4}{\sqrt{M^2 - 1}} \Delta P \tag{A-3}$$

$$z_c^{new} = z_c^{old} + \Delta z_c \tag{A-4}$$

where P , z_c and ε denotes load, camber and relaxation constant for camber correction, respectively.

The present target load distribution for the wing-fuselage configuration was computed by Mitsubishi Heavy Industries, Ltd. (MHI) [A5]. A new wing was created by adding the original thickness distribution (NACA0003) to the new camber lines. Figure A-2 shows the wing sections of the designed wing at the 20, 40, 60 and 80% spanwise locations.

Natural Laminar Flow and Inverse Design

The second strategy of the wing refinement was reduction of friction drag through a natural laminar flow (NLF). To preserve NFL on the wing surface longer, the wing thickness distribution was changed from NACA0003 to NACA66003 airfoil thickness distribution on which the turbulent transition expected to be delayed downstream. This was named as NAL's 2nd baseline configuration. Figure A-3 plots the resulting airfoil sections at the 20, 40, 60 and 80% spanwise locations. However, it didn't delay turbulence transition as expected.

The present inverse design was thus applied to find a proper wing geometry for NLF.

The target pressure distribution for NLF on the upper surface of the wing used in this design was defined by Kawasaki Heavy Industries, Ltd. (KHI) [A6]. The target has a rapid pressure drop near the leading edge followed by a flat pressure distribution toward the trailing edge. The lower surface pressure distribution was specified by subtracting the optimal load distribution previously suggested by MHI. With this target pressure distribution, the inverse design was performed. In this case, the integral equations were applied to the entire wing surface. The modification with the lower order approximations was not used yet. The geometry obtained here became NAL's 3rd baselines configuration. Figure A-4 shows the pressure distributions and corresponding geometries at the 20, 40, 60 and 80% spanwise sections after 5 iterations in the inverse design. Although the pressure distribution of the designed wing became close to the target pressure distribution, there still existed discrepancies between them. There were several difficulties in the target pressure distribution. The specified target pressure distribution had a spike at the leading edge on the lower surface of the wing. This produces a beak-like leading edge. This kind of the leading edge is unacceptable from the structural point of view. In addition, the wing thickness near the tip became too thin. Thus, the target pressure used for 3rd baseline configuration was further modified to shape the leading edge appropriately and to meet the thickness constraint. The modifications were carefully carried out so as not to disturb NLF.

With this modified target pressure distribution, the inverse design was performed again [A7]. In this case, the lower order approximation was applied to near the wing tip. The results of inverse design with the modified target pressure were presented in Fig.

4-2 in Sec. Ⅳ-2. For NAL's final wing configuration, some geometry corrections are further performed to this geometry so as to satisfy several structural requirements.

References

[A1] Y. Shimbo, K. Yoshida, T. Iwamiya, R. Takaki and K. Matsushima, "Aerodynamic Design of Scaled Supersonic Experimental Airplane," Proceedings of 1st International CFD Workshop for SST Design, pp. 62-67, Tokyo, Japan, NAL, March 1998.

[A2] H. W. Carlson and D. S. Miller, "Numerical Method for the Design and Analysis of Wings at Supersonic Speeds," NASA TN D-7713, 1974.

[A3] H. Ashely and M. Landahl, *Aerodynamics of Wings and Bodies*, Addison-Wesley Publishing Company, Inc., Reading, 1965.

[A4] Y. Shimbo, K. Yoshida, T. Iwamiya and R. Takaki, "Linear and Non-Linear Analysis/Design of a SST Configuration," Proceedings of the 29th Fluid Dynamics Conference, pp. 369-372, September 1997 (in Japanese).

[A5] W. D. Middleton and J. L. Lundry, "A System for Aerodynamic Design and Analysis of Supersonic Aircraft," NASA CR-3551, 3552, 3553, 3554, September 1980.

[A6] H. Ogoshi, "Aerodynamic design of an Supersonic airplane wing – Application of the Natural Laminar Flow Concept to Airfoil," Proceedings of the 47th Nat. Cong. of Theoretical & Applied Mechanics, January 1998 (in Japanese)

[A7] K. Matsushima, T. Iwamiya, S. Jeong and S. Obayashi, "Aerodynamic Wing Design for NAL's SST Using Iterative Inverse Approach," Proceedings of 1st

International CFD Workshop for SST Design, pp. 73-78, Tokyo, Japan, NAL, March 1998.

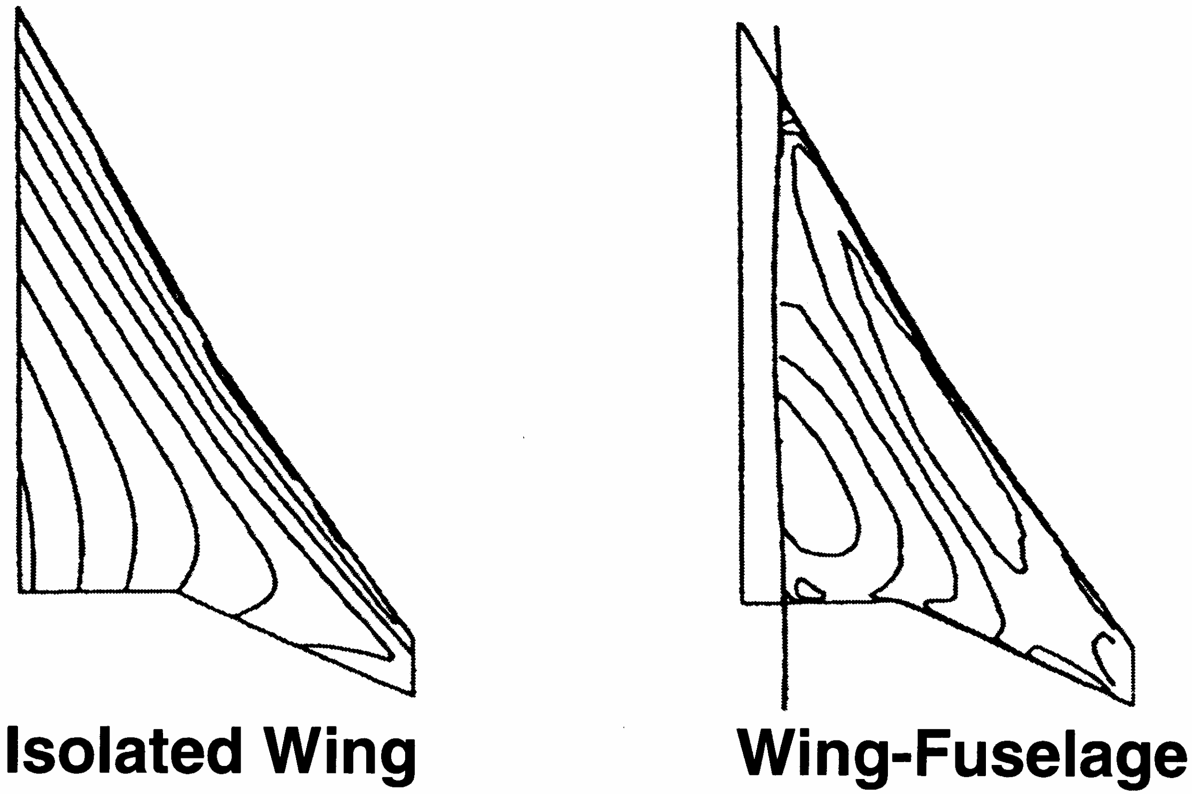

Figure A-1. Comparison of load distributions between the isolated wing and the wing-fuselage configuration

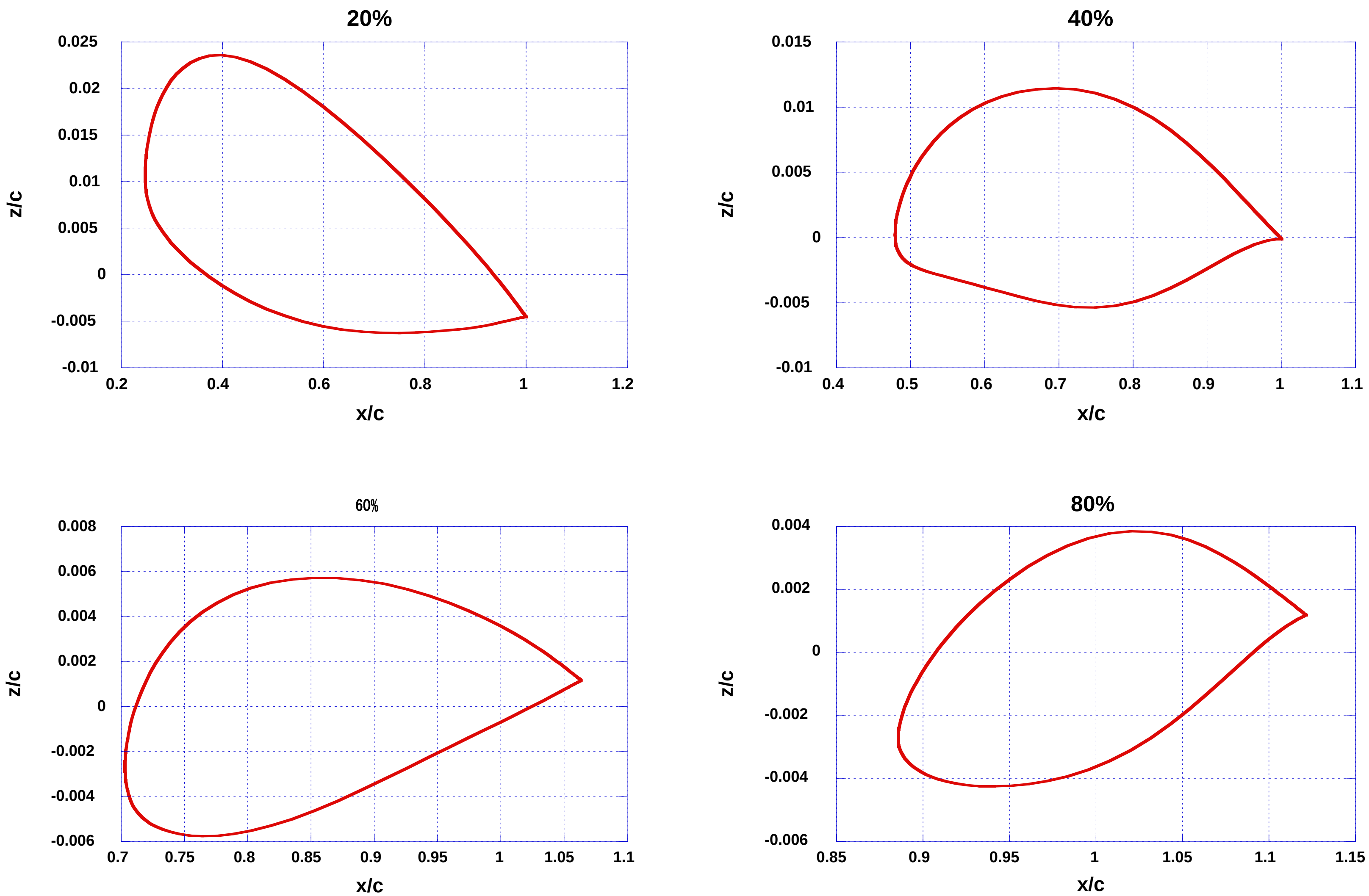

Figure A-2. Wing sections of the NAL's 1st configuration

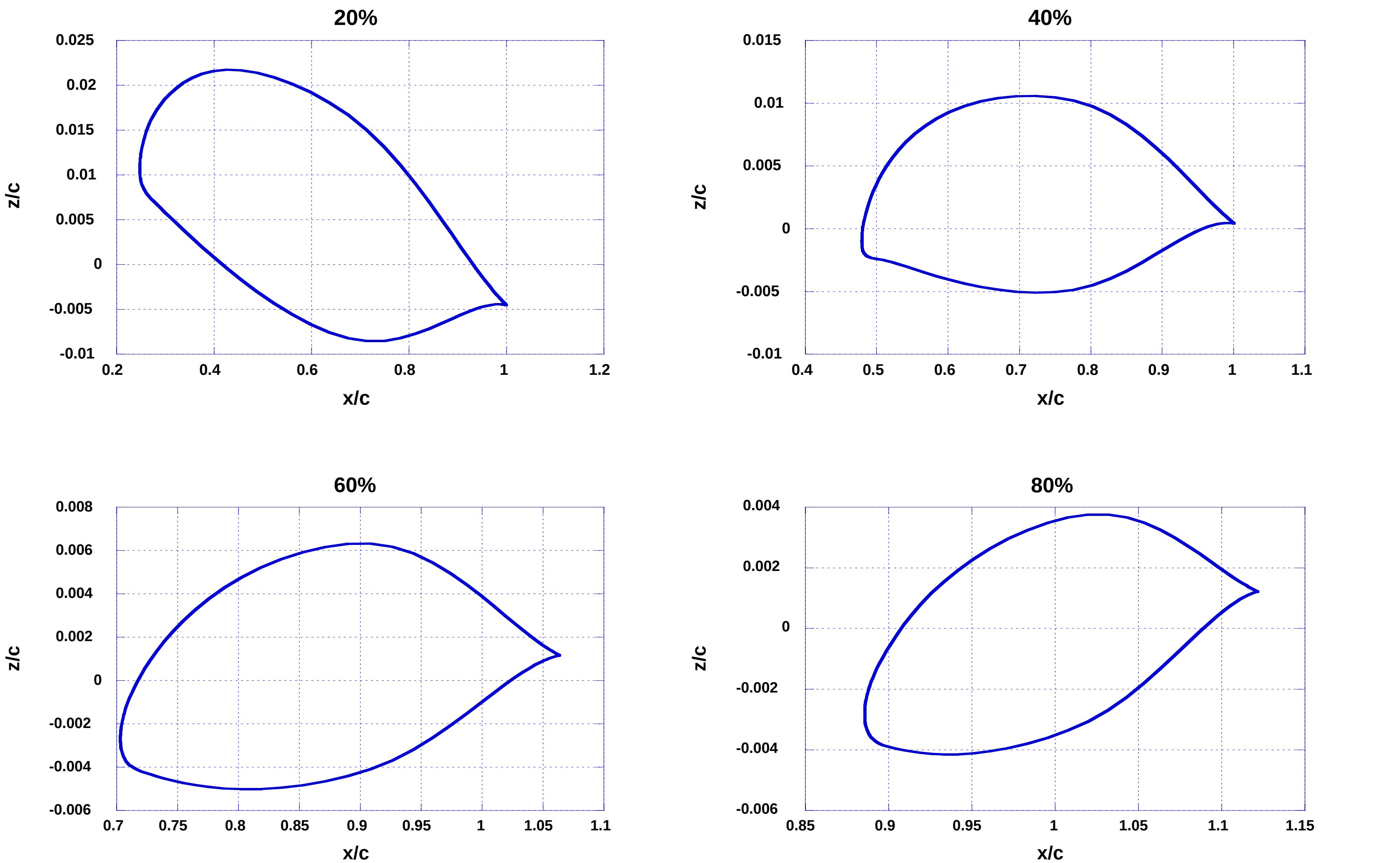

Figure A-3. Wing sections of the NAL's 2nd configuration

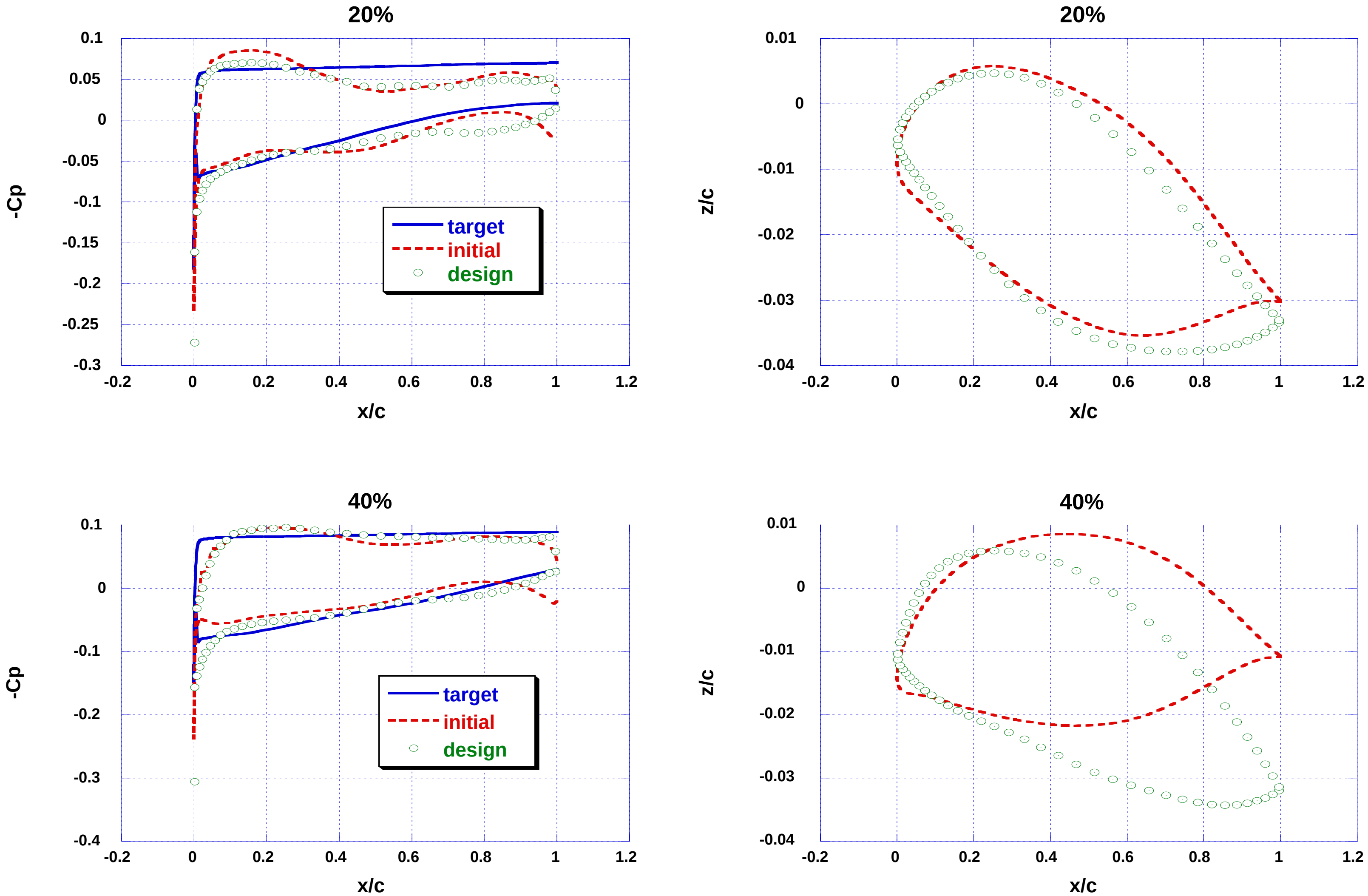

Figure A-4. Comparison of pressure distributions and corresponding geometries among the target, initial and designed wings (1)

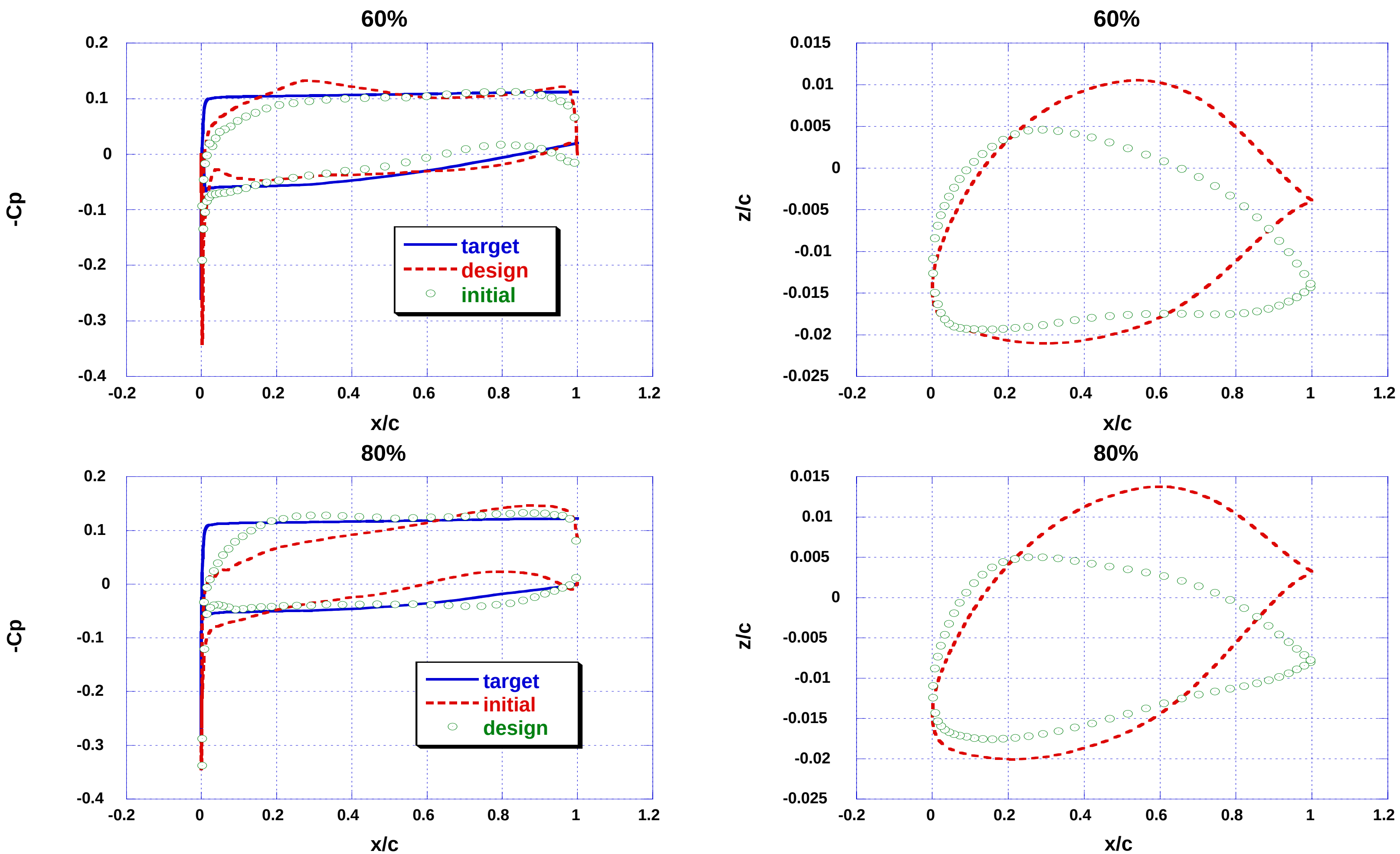

Figure A-4. Comparison of pressure distributions and corresponding geometries among the target, initial and designed wings (2)